Effect of Extracellular Stiffness on the Blood-Brain Barrier

By

Allison Bosworth

Dissertation
Submitted to the Faculty of the
Graduate School of Vanderbilt University
in partial fulfillment of the requirements
for the degree of
DOCTOR OF PHILOSOPHY
in
Biomedical Engineering
August 13, 2021
Nashville, Tennessee

Approved:
Ethan Lippmann, Ph.D.
Leon Bellan, Ph.D.
W. David Merryman, Ph.D.
Cynthia Reinhart-King, Ph.D.
Matthew Schrag, Ph.D.

For my grandfather, Edward August Bosworth, who suffered from dementia and passed away on March 18, 2018 in the second year of my PhD program. He always supported my academic pursuits and continues to motivate my research endeavors.

ACKNOWLEDGEMENTS

I have so many people to thank for their support over the last 5 years of my PhD journey. I have grown tremendously as a researcher and I have learned so much about myself. This accomplishment would not have been possible without my mentors, the resources available at Vanderbilt University, and the support of my family and friends.

First, I need to thank my advisor, Ethan, for his guidance and his patience throughout my time in his lab. There were many hurdles and failed experiments that I experienced as the first person in our lab to experiment with biomaterials and mechanobiology. Ethan was always patient throughout this process and provided ample guidance and resources for me to succeed and grow as a researcher. I have learned so much from him about how to be a compassionate mentor, how to start a research project from scratch, and how to think critically while troubleshooting experimental issues. In addition, I have had a number of talented mentors in the Lippmann lab. Emma Neal trained me on all things iPSC culture, blood-brain barrier modeling, and molecular biology techniques. I also learned a lot from her about how to be a thoughtful and efficient researcher, and I am so incredibly appreciative of the time she spent mentoring me. Our lab postdocs Dan Balikov, Brian O'Grady, and Hyosung Kim have contributed to my scientific training as well, teaching me the importance of being well-versed on literature, how to image complex samples, and how to perform image quantification, respectively. I have also learned from being a mentor myself. I had the pleasure of mentoring Jake Peters, Robbie Weinstein, Derek Lee, Izzy Richter, and a few visiting scientists. Through these experiences, I have learned so much about mentoring, training, and encouraging other scientists. My peers in the Lippmann lab, Jonah Rosch, Kylie Balotin, Ketaki Katdare, Yajuan Shi, Everett Allchin, Lexi Yates, Madison Stiefbold, Nick Marinelli, Rachel Boone, Sam Thompson, Sarah Sturgeon, Lauren Drake, and Corrinne

Warlick have been a pleasure to work with. I feel incredibly grateful to have worked alongside so many talented researchers, and I can always count on someone to help me out if I’m in a bind or just need a friend.

My family and friends from home have provided me with so much support and love, and I am immensely grateful to them. My parents, first and foremost, have sacrificed so much to allow me and my siblings to get the best education and the best opportunities to succeed in our careers, and I would definitely not be here if it were not for their sacrifices. My sister, Adrianne Bosworth, my brother, Steven Bosworth, my sister-in-law, Rachel Bosworth, my grandmother, Kathleen Bosworth, and my uncles Jeff Bosworth and Tim Bammel are an incredible emotional support system for me. Their constant love and advice have gotten me through so many difficult times during my PhD. My friends from home, Hailie Myers, Tina Azar, and Rebecca Kusch, have also been an amazing support system for me since high school. Finally, I have to thank my boyfriend Robin Rodriguez who is the most supportive, caring, and compassionate person I know. I would not have finished graduate school if it were not for his daily love and support. I am so incredibly thankful to have all of these people in my life cheering me on.

My friends in Nashville have also supported me immensely during my PhD. I moved in with my roommates, Katie Ozgun and Natalie Noll, in my first year, knowing very little about them or what graduate school would entail. They have been such considerate, caring, and fun roommates, and I am so thankful to have been on this journey alongside them. My best friends Jonah Rosch, Mohsin Rahim, Prarthana Patil, Ella Hoogenboezem, Kyle Garland, and Dickie Darcy have been such a great support system for me. In 2016, moving to Nashville for graduate school meant leaving my home and leaving everyone I knew, but these friends quickly made Nashville feel like home. We have so many fun memories of exploring Nashville together, from karaoke to trivia to escape rooms. Words cannot express how grateful I am to have them in my life. I have also become so close with Kylie Balotin because of our shared interests in tv shows and shared hobbies. She has been an incredibly supportive officemate, and I am so thankful for all of our coffee walks together. I am so lucky to call these people friends, and I look forward to calling them friends for life.

I have had an excellent group of mentors on my thesis committee at Vanderbilt as well, and I am very grateful for their feedback and guidance. Dr. Matthew Schrag has taught me so much about CAA and always goes above and beyond to provide encouraging feedback about the importance of my work. Dr. Cynthia Reinhart-King, Dr. David Merryman, and Dr. Leon Bellan have all provided critical guidance to me on my projects regarding hydrogels, mechanobiology, and AFM. My undergraduate mentors, Dr. Daniel Hayes, Dr. Jan Lammerding, and Dr. Jun Nakanishi, were such thoughtful and encouraging mentors, and I would not have been able to pursue a PhD if it were not for their supportive letters of recommendation. I am so thankful to have worked with so many talented mentors.

TABLE OF CONTENTS

Page

Abbreviations

α-SMA: Alpha-smooth muscle actin
AD: Alzheimer’s Disease
AFM: Atomic force microscopy
AOC3: Amine oxidase copper containing 3
ApoE4: Apolipoprotein E4
BBB: Blood-brain barrier
BMEC: Brain microvascular endothelial cells
CAA: Cerebral Amyloid Angiopathy
CD31: Platelet endothelial cell adhesion molecule
CNS: Central nervous system
CPM: Counts per million
CsA: Cyclosporin A
ECM: Extracellular matrix
FDR: False discovery rates
Gel-MA: Methacrylated gelatin
iPSC: Induced pluripotent stem cell
kPa: Kilopascal
LAP: Lithium phenyl-2-4-6-trimethylbenzoylphosphinate
LOX: Lysyl oxidase
MMP: Matrix metalloproteinases
MRP: Multi-drug resistance proteins
mTG: Microbial transglutaminase
PA: Polyacrylamide
PF-QNM: Peak force quantitative nanomechanical mapping
PKA: Phospho-kinase array
PGP: P-glycoprotein
R123: Rhodamine 123
ROCK: Rho-associated protein kinase
TEER: Trans-endothelial electrical resistance
tTG: Tissue transglutaminase
VCID: Vascular cognitive impairment and dementia

LIST OF MAIN TABLES

Table Page

LIST OF APPENDIX TABLES

LIST OF MAIN FIGURES

LIST OF APPENDIX FIGURES

Figure Page

Chapter 1

INTRODUCTION

1.1 Alzheimer's Disease Background

Neurodegenerative disorders involve gradual deterioration of neurons within the central nervous system, leading to impairments in cognitive function. The most common form of neurodegenerative disease, Alzheimer's Disease (AD), makes up 60 to 70% of all cases and is the 6th leading cause of death in the United States. In AD, symptoms typically present as amnesia, i.e. the inability to learn new information or recall recent information. Ultimately, patients with advanced AD experience personality and mood changes, poor judgement and decision-making, and difficulty holding a conversation. These impairments make AD patients heavily reliant upon caretakers to perform basic day-to-day functions. Moreover, this co-dependence makes AD an incredibly expensive disease. An estimated $236 billion was spent on AD during 2016 including patient care and familial caregivers' lost wages[1]. In addition, the biggest risk factor for AD is age, and approximately one-third of people over 85 are diagnosed with the disease. Looking forward, as global life expectancies continue to rise, so will the prevalence of AD. As shown in Figure 1.1, a 2015 projection stated that the number AD diagnoses in the United States will to triple from 5 million in 2010 to 15 million in 2050 if no therapeutic or preventative strategies are developed[2]. Given the heavy disease burden, discovery of underlying disease mechanisms and development of novel treatment strategies has huge societal implications.

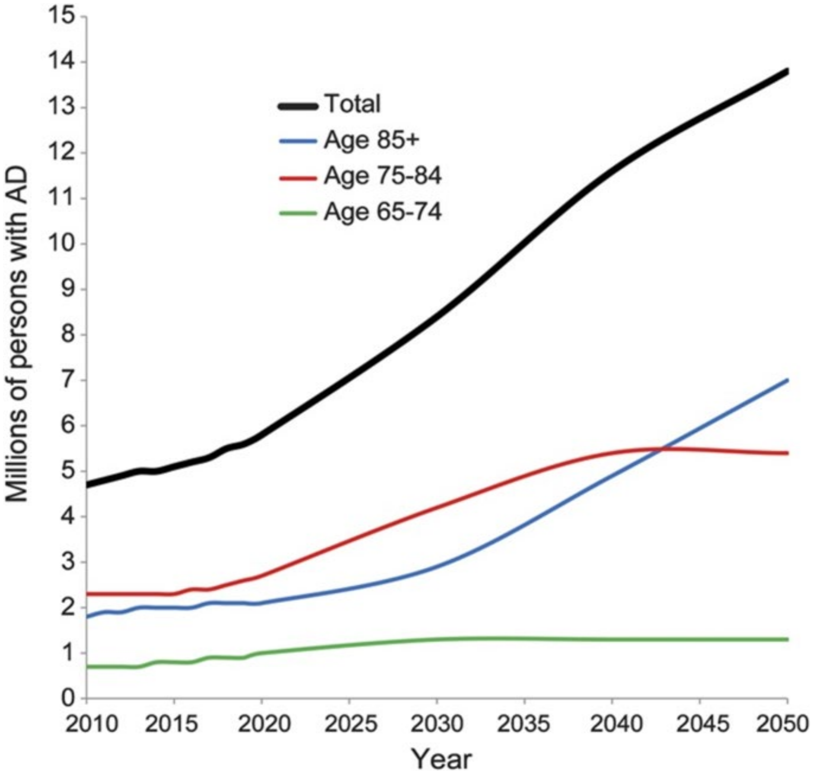

Figure 1.1 Estimate number of people in the US with AD. Projections show that the number AD cases will climb with increasing life expectancies if not therapies are developed. Figure adapted from Hebert, 2013[2].

Hallmarks of AD pathology include extracellular amyloid-β plaques and intracellular tau tangles in the brain parenchyma, both of which contribute to neuronal death. Amyloid-β plaques form when amyloid-β peptides are overproduced or when they are not properly cleared from the brain. Excess amyloid monomers aggregate to form oligomers, then fibrils, then ultimately large plaques. Familial cases of AD have an earlier disease onset, and typically involve genetic mutations on amyloid precursor protein that lead to its overexpression. Sporadic cases of AD are typically correlated with impaired amyloid-β clearance. In both familial and sporadic cases, the presence of amyloid aggregates disrupts neuronal synapses. Inhibition of long-term potentiation[6] and reduction of synaptic number and plasticity[7] have been correlated amyloid-β load in AD. In addition, amyloid-β elicits an immune response in astrocytes, a glial cell type that supports neuronal function, and microglia, the resident immune cell type in the brain. Activated astrocytes and microglia secrete cytokines that cause neuroinflammation, exacerbating AD progression[8]. The cumulative effects of amyloid-β aggregates are incredibly detrimental to neuronal function and over time can lead to broad cognitive deficits.

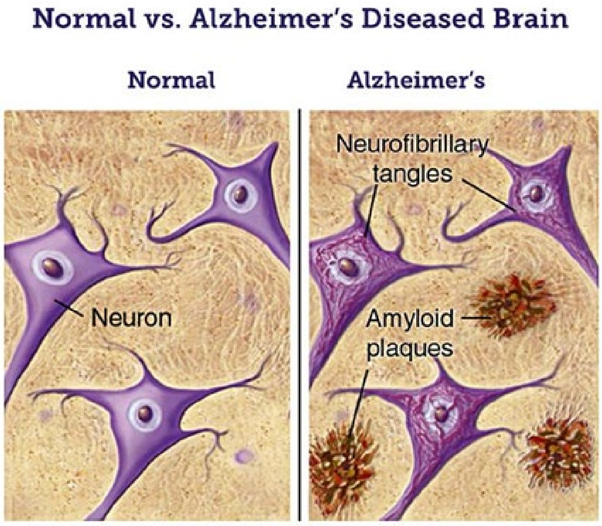

Figure 1.2 Hallmarks of AD. Extracellular amyloid plaques and neuronal tau tangles are the traditional hallmarks of AD. Figure adapted from BrightFocus, 2015[3].

The goal of AD drug development initiatives has largely been to remove extracellular amyloid-β from the brain or block further aggregation. Numerous approaches have been tested to accomplish this goal, including inhibition of secretase enzymes and binding of aggregation-blocking proteins to amyloid. β and γ–secretase enzymes cleave amyloid precursor protein to form amyloid-β monomers. Three AD drugs that made it to phase 3 clinical trials, Verubecestat, Semagacestat, and Tarenflurbil, aimed to inhibit secretase activity. Verubecestat, a β-secretase enzyme inhibitor, blocked the formation of amyloid-β in pre-clinical experiments using animal models for AD[9]. In clinical trials however, Verubecestat did not reduce cognitive decline in AD patients, and it was associated with a higher incidence of adverse events, including falls and injuries, sleep disturbance, and weight loss, in comparison to placebo groups[10,11]. Semagacestat[12] and Tarenflurbil[13], which inhibit γ-secretase with the same goal of preventing amyloid-β formation, failed in phase 3 clinical trials in similar fashions. No changes in cognitive function were observed and incidences of adverse events were higher.

Alternate AD drug strategies involve direct binding of a protein to amyloid-β peptides, physically blocking interactions with neighboring monomers and preventing further aggregation. Bapineuzumab and Solanezumab are monoclonal antibodies specific to amyloid-β that made it to phase 3 clinical trials. Bapineuzumab reduced tau levels and decreased rate of amyloid accumulation in the brain, but no difference in cognitive function was observed in comparison to a placebo group[14]. Developed to promote clearance from the brain, Solanezumab also failed to reduce amyloid load and failed to improve cognitive function[15]. With each of these failures, pharmaceutical companies lost hundreds of millions of dollars. In light of these losses, many pharmaceutical companies have reduced the number of central nervous system programs that they are funding[16]. Table 1.1 shows recent AD drugs that have failed in clinical trials, demonstrating that multiple mechanisms of action against amyloid have been ineffective. Therefore, it is up to academic researchers to fill the knowledge gap in our understanding of AD to allow for smarter drug design.

Table 1.1 Recent AD clinical trial failures. A bevy of AD drug candidates, developed to combat amyloid, have failed in clinical trials due to lack of efficacy. Further, some even worsened cognition. Table adapted from Oxford, 2020[1].

DRUG	MECHANISM	TRIAL PHASE	REASON FOR FAILURE	COMMENTS
Semagacestat	γ-secretase inhibitor	III	Toxicity, lack of efficacy	Worsens cognition
Avagacestat		II		
Bapineuzumab	Monoclonal antibodies to Aβ or its oligomers or fibrils	III	Lack of efficacy	Amyloid imaging abnormalities
Aducanumab		III	Futility analysis	Prediction that trials would not improve cognition
Solanezumab		III	Lack of efficacy	
Gantenerumab		II		
Crenezumab		II		
Verubecestat	BACE-1 inhibitor	III	Lack of efficacy	Worsens cognition
Atabecestat		III	Toxicity	
Lanabecestat		III	Lack of efficacy	

As amyloid-centric therapies fail in clinical trials, other aspects of the disease pathology, namely vascular impairments, are gaining attention as important contributors to cognitive decline. Vascular cognitive impairment and dementia (VCID) is the second most common cause of dementia behind neurodegenerative diseases. Approximately 40% of AD patients also have some form of VCID[17–20]. Known causes of VCID include stroke, hypoperfusion of the brain, and microhemorrhages, each of which disrupt blood flow to the brain. More consideration is being given to this aspect of AD, and some researchers speculate that amyloid drugs are only effective in AD mouse models that lack this vascular component. When the vascular pathologies were introduced to a mouse model for AD, treatment with an amyloid-targeting drug make the vascular pathology worse[21]. Although reductions in amyloid burden were observed, an increase in microhemorrhages negated any cognitive benefits that may have resulted from amyloid clearance. This evidence suggests that vascular contributions to AD may be crucial to understanding the underlying disease mechanisms.

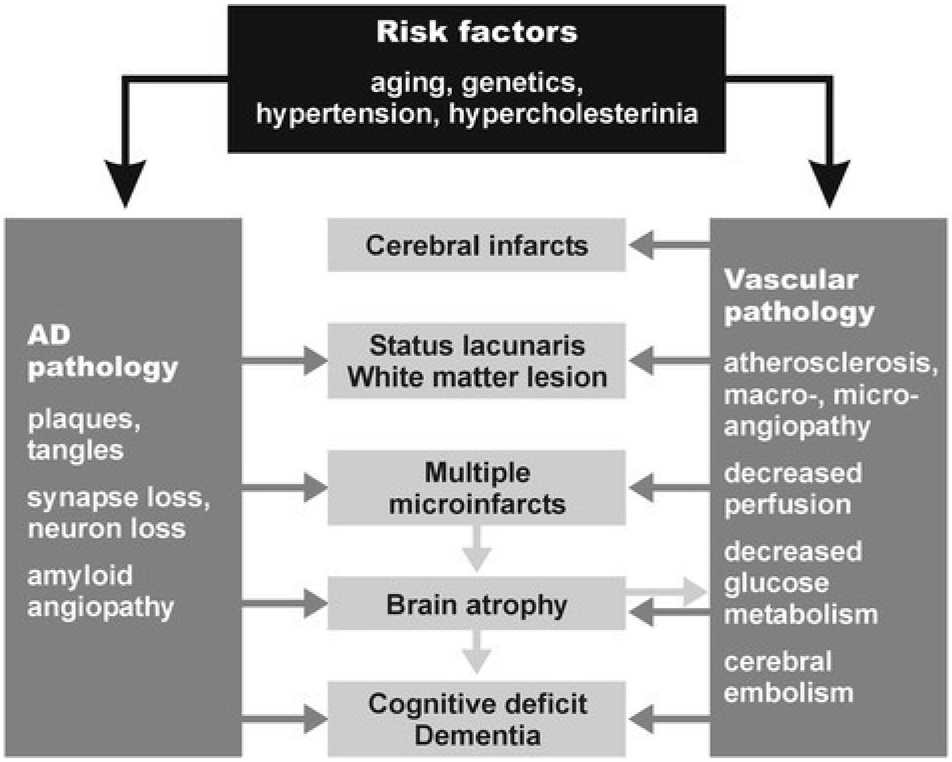

Figure 1.3 Shared risk factors between AD and vascular pathology. Similar risk factors and resulting symptoms occur between these two pathologies, highlighting the importance of vascular contribution to AD-related cognitive decline. Figure adapted from Jellinger, 2007[4].

Many risk factors for dementia overlap with the risk factors for cardiovascular disease (Figure 1.3)[22]. Age, smoking, obesity, diabetes, and midlife hypertension and high cholesterol increase likelihood of both diseases. On the other hand, physical activity and heart-healthy diets have been associated with lower risk of AD. Another overlapping risk factor between AD and cardiovascular disease is apolipoprotein E4 (ApoE4)[23], which has been shown to increase the risk of coronary artery disease[24]. An estimated 65-80% of AD patients carry the ApoE4 allele. In AD, ApoE4 correlates with increased production of amyloid-β by neurons and reduced uptake and degradation of amyloid-β by astrocytes[25]. These overlapping factors suggest that vasculature is compromised in AD patients. More holistic therapeutic strategies that address both of these components are likely to be more effective at reducing cognitive deficits than the aforementioned amyloid therapies alone.

1.2 Blood-Brain Barrier Background

Similar to peripheral vasculature, the primary role of brain vasculature is to deliver a constant supply of oxygen, glucose, and other essential nutrients to parenchymal tissue while removing carbon dioxide and metabolic waste products. However, brain vasculature differs from peripheral vasculature in that the endothelial cells form a much more restrictive barrier called the blood-brain barrier (BBB). The BBB strictly regulates transport of cells, proteins, small molecules, and even ions into the brain in order to maintain neuronal homeostasis. Passive paracellular diffusion across the BBB is restricted by intercellular tight junctions that give the BBB a high trans-endothelial electrical resistance. Transcytosis is regulated by specific transporter proteins and cell surface receptors[26]. Small lipophilic compounds that diffuse into BBB are pumped back into circulation by efflux transporters, such as P-glycoprotein (PGP) and MRP family transporters. This barrier phenotype is supported by pericytes and astrocytes, which ensheath the BBB endothelial cells. Together, they make up the neurovascular unit.

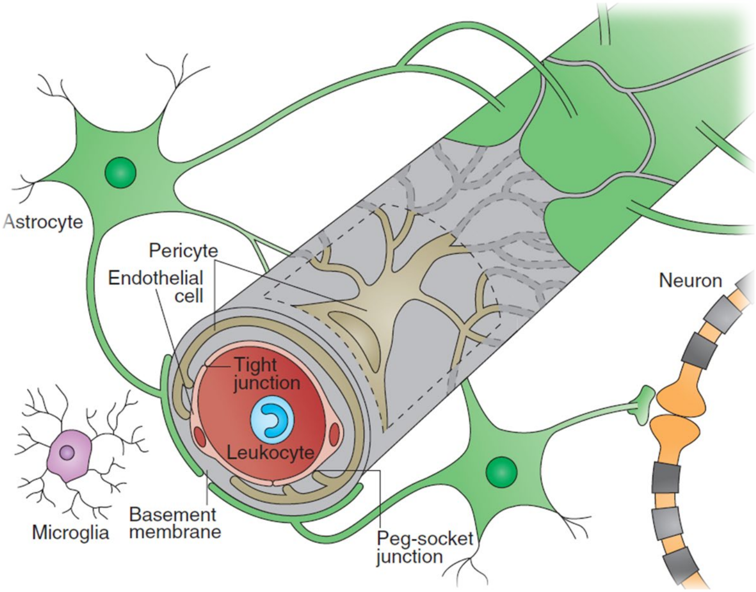

Figure 1.4 Components of the neurovascular unit. Brain microvasculature is composed of endothelial cells, pericytes, and astrocytes, which are supported by neurons and microglia. Figure adapted from Obermeier, 2013[5].

Breakdown of the BBB is associated with many disease states including stroke[27], neurodegenerative disease, traumatic brain injury, brain tumors, and natural aging[28]. This typically results in increased permeability of solutes into the brain, disrupting ionic concentrations within the neuronal microenvironment. In AD, PGP is downregulated in the presence of amyloid-β[29,30], allowing small lipophilic solutes to more readily enter the brain. Decreased PGP activity also prevents proper clearance of amyloid-β from the brain. Reductions in glucose transporters at the BBB have also been correlated with AD[31]. Since the brain contains few energy reserves, it relies heavily upon a constant supply of glucose, consuming an estimated 20% of the body's total circulating supply[32]. Consequently, the results of reduced glucose transport in AD can be detrimental. AD models show that reduced glucose states lead to hyperphosphorylation of tau and more amyloid-β generation[33]. Independent of amyloid and tau, BBB breakdown alone has been implicated as an early biomarker of cognitive decline[34]. Thus, BBB integrity may be a better biomarker for cognitive function than amyloid levels.

In addition to these functional changes in AD, structural changes to the BBB have also been reported in AD. The endothelial basement membrane, typically 50-100 nanometers wide, can thicken to four times its original size in comparison to age-matched controls for AD[35]. This thickening is associated with increased collagen content in the BM[36]. In arteries and arterioles, some amyloid-β aggregates can deposit directly onto the vessel wall in concentric rings. This occurs in 20% of AD cases and is called Cerebral Amyloid Angiopathy (CAA). In CAA vessels, vessel diameter regulation is impaired because neurovascular unit connections are broken. Endothelial cells cannot readily receive vasoconstrictive cues from astrocytes because there are large amyloid aggregates between them. CAA-affected vessels experience vascular smooth muscle cell death and dilation of perivascular spaces[37,38]. In addition, it is speculated that the rigid cast formed by amyloid aggregates also inhibits contraction. Taken together, these extracellular matrix modifications, capillary basement membrane thickening and bulk protein deposition on arteries and arterioles, may be contributing to the BBB breakdown that is observed in AD.

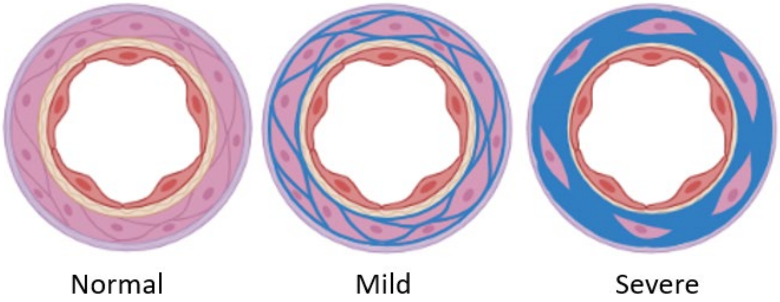

Figure 1.5 Arteriole composition during CAA progression. Arterioles, typically lined by 1-2 layers of vascular smooth muscle cells, experience accumulation of amyloid aggregates (blue) during CAA, ultimately leading to vascular smooth muscle cell death.

To characterize extracellular matrix (ECM) changes related to AD, some have reported changes in brain stiffness. Whole brain stiffness measurements using magnetic resonance elastography have shown that whole brain stiffness decreases in AD patients relative to age-matched control patients[39]. Follow-up work using similar methods showed that these stiffness changes in AD vary across different regions of the brain[40]. However, to our knowledge, no one has reported stiffness values of the blood vessels from AD brains. We suspect that deposition of amyloid aggregates increases local stiffness at the vessel wall in CAA.

1.3 Endothelial Mechanosensing Background

To gain insight into the significance of tissue stiffening, known mechanisms from peripheral tissue can be examined. ECM stiffening has been implicated in aging, cancer, fibrosis, and cardiovascular disease. In cancer and fibrosis, activated fibroblasts increase matrix protein deposition to stiffen the local environment[41]. In cardiovascular disease, arterial stiffening progresses with age and is associated with increased collagen deposition and fragmentation of elastic fibers in the intima[42]. These trends can be observed by studying mechanical and biochemical features of tissues during disease progression. Measurements of the mechanical properties of tissues can be collected using multiple techniques. Imaging modalities such as pulse wave velocity and magnetic resonance elastography can be used to measure *in vivo* vessel stiffness non-invasively. Tensile testing can be performed on excised tissue to measure stiffness of large, homogenous tissue structures such as decellularized aortas to quantify stiffness[43]. Intricate features of live tissue sections can be measured by atomic force microscopy (AFM) to determine the stiffness of the features within the tissue. For example, stiffening of lung vessels[44] and aortic valves[45] have been reported using AFM methods.

Attempts to model these ECM stiffness changes *in vitro* typically involve the use of tunable hydrogel substrates. Hydrogel materials can be animal derived, i.e. gelatin, collagen, and matrigel, or synthetically produced, i.e. polyacrylamide and polyethylene glycol. These hydrogels are incorporated into cell culture systems to provide a substrate that better mimics the *in vivo* microenvironment with respect to ECM composition, stiffness, and topography. Natural hydrogels are also amenable to three-dimensional cell culture, allowing for the development of complex tissue structures that more accurately model the native tissue architecture than two-dimensional cell culture. The recent development of dynamic hydrogel systems such as methacrylated gelatin and methacrylated hyaluronic acid can even better recapitulate *in vivo* disease conditions by stiffening in response to light.

Recent work from our lab has shown that gelatin can be biofunctionalized with a cadherin peptide to support neuronal growth and maturation[46]. This peptide is derived from N-cadherin and mimics the growth cues in the native ECM during brain development, ultimately allowing for the formation of a synaptically connected neuronal culture in 3-D. More recent, unpublished work with this model implies that this biofunctionalized gel also supports the growth of post-mortem human tissue. We can use this system to mimic microenvironmental factors including stiffness, protein density, shear flow, porosity, and presence of soluble growth factors. This system is advantageous for modeling human disease because all of these cues can be tuned more readily and more quickly than with animal models.

In vitro hydrogel models have contributed to the discovery that endothelial cells are responsive to a variety of extracellular mechanical cues, including shear stress, bifurcations, curvature, and stiffness[47]. Aortic endothelial cells respond to increased stiffness by increasing Rho-mediated contractile forces, which in turn disrupt of tight junction integrity[48]. Compromised junctional integrity leads to increased endothelial permeability to circulating solutes and immune cells. A similar trend is observed in a model of pulmonary edema, in which lung vascular permeability increases in response to matrix stiffness[49]. The conservation of this phenomenon across multiple tissue types supports our hypothesis that vessel stiffening at the BBB could cause breakdown of the barrier phenotype.

Very little work has been reported at the intersection of endothelial mechanosensing and the human BBB, but recent work from our lab shows that 3-D hydrogel systems can be used to study BBB endothelial cells are responses to shear stress[50]. Gelatin macrochannel devices were fabricated, and channels were lined with collagen type IV and fibronectin to mimic the BBB basement membrane. Human iPSC-derived brain endothelial cells were then seeded into macrochannel and exposed to varying degrees of shear flow. It was found that shear flow enhanced barrier properties, as measured by permeability to 3 kDa dextran, in comparison to static conditions. Further, optimal barrier properties occurred at 32 mPa (0.3 dyne/cm2), and increases in shear stress diminished worsened barrier properties. This work supports our hypothesis that human BBB endothelial cells are responsive to mechanical cues, and that they may also be responsive to extracellular stiffness.

1.4 Atomic Force Microscopy Background

Originally invented in the 1980s as a way to image both conducting and insulating surfaces below the optical resolution limit, the AFM allowed for high resolution imaging of flat surfaces. It has emerged as a fundamental research tool for measuring the mechanical properties of biomaterials. It uses a scanning probe to indent samples, creating a force versus displacement curve that can be analyzed to determine elastic properties of the material[51]. Many have used this tool to measure the Young's elastic modulus of hydrogels for implementation in cell culture models, and a variety of AFM models exist to accommodate different sample types. For measuring very soft biomaterials, it is advantageous to use a large, blunt probe while measuring hard biomaterials is more amenable to small, pointed tips. This allows for more accurate deflection readings because rigid, sharp probes are likely to sink into soft materials without deflecting at all. Typically, force curve measurements of soft biomaterials also exhibit larger indentation depths, which ultimately determines the type of modulus fit model used to calculate Young's modulus. When indentation depth is much smaller than the tip radius, the Hertzian model is used. When indentation depth is much larger than the tip radius, the Sneddon model is used. When indentation depth is approximately equal to the tip radius, a hybrid model called the Cone Sphere model is used. Young's modulus of soft biomaterials is typically calculated using the Sneddon model. This tunability within the AFM system allows for more accurate calculations of stiffness measurements across a wider range of biomaterials.

More recently, AFM has been applied to live tissue sections to measure stiffness of specific tissue features[44,45]. Alternative mechanical testing methods such as bulk tensile or compressive testing are not advantageous for the measurement of human brain tissue. The small vessel size, the soft nature of brain parenchyma, and the overall tissue heterogeneity make bulk mechanical testing impossible, and imaging methods cannot resolve micron-sized features. Conversely, AFM probes containing a tip radius at the nanometer scale allow for detection of very small features within the tissue with excellent spatial resolution. For interrogation of brain mechanical properties, AFM has been used to measure stiffness of live rat brain sections. Reports show that unique stiffness properties exist in white and grey matter[52] and in the hippocampus[53]. Measurements of human brain vasculature, however, have never been reported to our knowledge.

1.5 Outline of Dissertation

This dissertation consists of 4 chapters.

Chapter 2 details the characterization of post-mortem human cortical tissue affected by CAA. Mechanical characterization of CAA vessels was performed via atomic force microscopy to elucidate vessel stiffness. Additionally, IHC was performed on tissue sections to identify LOX presence and fibrosis markers, namely perivascular fibroblasts colocalizing with α-SMA, in CAA vessels.

Chapter 3 uses a human *in vitro* model of the BBB to determine effect of substrate stiffness on barrier function. Polyacrylamide hydrogel substrates were incorporated into existing BBB model, and barrier function was assayed via TEER and efflux activity. Actin organization and tight junction width and tortuosity was also quantified as a function of stiffness. Bulk RNA sequencing and phospho-kinase array datasets revealed global differences in BBB endothelial cells as a function of stiffness.

Chapter 4 demonstrates alternative approaches to studying human CAA *in vitro*. Gelatin-based dynamic stiffening hydrogels that stiffen in response to light were incorporated into the model system from Chapter 3 in order to measure TEER in real time as substrate stiffness increases. Another gelatin-based biofunctionalized hydrogel was used to embed post-mortem human tissue from Chapter 2 to support vessel survival and growth. Both of these hydrogel systems may be valuable in mimicking the extracellular microenvironment in human CAA.

Chapter 5 provides conclusions for the work discussed in this dissertation as well as future areas of focus for this research.

Chapter 2

STIFFNESS ALTERATIONS AND PERIVASCULAR FIBROSIS: NOVEL PHENOTYPES IN CEREBRAL AMYLOID ANGIOPATHY

Adopted from: Bosworth AM, Nackenoff, A, Snider, JC, Sturgeon, S, Merryman, WD, Lippmann, ES & Schrag, MS. Structural alterations and perivascular fibrosis: novel phenotypes in cerebral amyloid Angiopathy. In preparation.

2.1 Summary

Cerebral amyloid angiopathy (CAA) is a vasculopathy produced when β-amyloid forms toxic deposits on cerebral arterioles and capillaries. However, the fundamental mechanisms by which β-amyloid accumulates in and undermines structural integrity of the vasculature remain unclear. Here, we used traditional and next-generation tissue imaging techniques, as well as biophysical measurements, to characterize changes to the vasculature in CAA. Atomic Force Microscopy allowed us to quantify stiffness of blood vessels with optimal spatial resolution to directly measure amyloid aggregates on the vessel wall.

CAA vessels were found to be significantly stiffer than both healthy and diseased control vessels. CAA vessels were also LOX-positive and showed higher occurrences of myofibroblast transition in perivascular fibroblasts. These findings reveal novel phenotypes of CAA that may contribute to our understanding of disease progression and its contribution to the cognitive decline that occurs in AD. Despite its prevalence in AD cases and its standalone contribution to cognitive decline, CAA is historically understudied in comparison to the amyloid hypothesis. Our understanding of CAA's direct link to cognitive decline may be incredibly valuable in developing more effective drugs for AD.

2.2 Introduction

A vascular pathology that commonly co-occurs with AD is CAA in which amyloid peptides aggregate and deposit onto blood vessels, ultimately leading to disruption of vessel architecture and increased microhemorrhages. CAA-affected vessels experience vascular smooth muscle cell death and dilation of perivascular spaces[37,38]. The progressive accumulation of amyloid in the medial layer of small arteries and arterioles chronically limits blood supply to the brain and causes focal deprivation of oxygen[54]. This phenotype occurs in 90% of AD cases, but can also occur in the absence of AD. The isoform of amyloid that accumulates in CAA, A-$\beta_{1\text{-}40}$, makes up approximately 90% of the total amyloid secreted from neurons, while the isoform that accumulates in parenchymal plaques, A-$\beta_{1\text{-}42}$, is less than 10% of total amyloid secreted. How and why the A-$\beta_{1\text{-}40}$ isoform deposits onto vessels is still unclear, but some speculate that it localizes to vasculature as part of a clearance mechanism, either via the bloodstream of perivascular drainage.

Clinical presentation of CAA can be hemorrhage events or gradual cognitive decline. The underlying loss of vascular tone in arteries and arterioles means that 1) blood vessels are leakier, causing increased microhemorrhage events, and 2) autoregulation of blood flow is slowly lost over time, causing gradual slowing of processing speed. CAA-related hemorrhages can be detected by MRI, and CAA vessels can be detected using amyloid PET imaging. Since no treatment currently exists for CAA, a patient's diagnosis is typically followed by counseling to minimize the risk of further hemorrhages by managing blood pressure, avoiding anticoagulant medications, and minimizing risk of falls. Because there is no treatment and because disease mechanisms are still not fully understood, we sought to characterize vasculature affected by CAA by measuring stiffness and observing changes to perivascular fibroblasts.

Recent work has shown that vascular dysfunction is a consistent predictor of cognitive impairment. For example, hypertension is associated with stroke and dementia, and many studies have reported instances of cognitive impairment in patients with arterial stiffening[55,56]. Even in stroke- and dementia-free persons, increased arterial stiffness correlated with lower cognitive function[57]. Although no reports have been made regarding vessel stiffening in CAA, one paper described mouse CAA vessels as having a "rigid cast" because they exhibited little to no constriction in response to soluble vasoconstrictive cues[58]. Additionally, ECM-remodeling enzymes lysyl oxidase and tissue transglutaminase have been associated with AD pathology, and these enzymes may contribute to tissue stiffening[59,60].

Work from our collaborators in the Schrag lab at Vanderbilt University Medical Center utilized CLARITY imaging techniques to observe changes to blood vessel morphology in CAA. CLARITY imaging involves clearing of tissue constructs such that they are rendered optically transparent, allowing for large vessels to be imaged without cryosectioning. Since CAA vessels are very brittle, cryosectioning typically shatters vessels or changes their morphology. CLARITY imaging of human post-mortem tissue shows the range of vascular morphologies that can occur during CAA pathogenesis (Figure 2.1). Control vessels exhibit smooth, straight walls while CAA vessels have thicker walls with areas of stricture and dilation. Exaggerated instances of stricture and dilation occur in areas near microhemorrhages. These morphological features may lead to changes in fluid dynamics, such as turbulence, velocity, or shear stress, that contribute to vessel rupture. In addition to these mechanical properties, morphology changes may also contribute to the loss of autoregulation that occurs in CAA arterioles. We sought to characterize additional changes to CAA vessels, namely vessel wall stiffness and perivascular cell phenotypes.

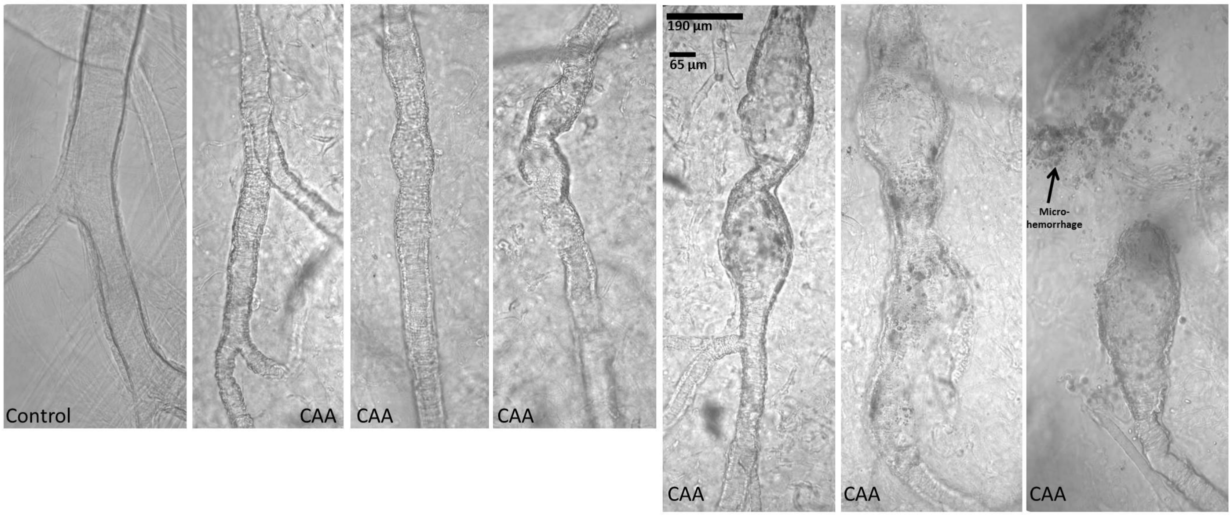

Figure 2.1 Morphologies of vascular degeneration in CAA. As CAA becomes more severe, vessel walls transition from being smooth (left) to rough with areas of dilation and stricture, which correspond to microhemorrhage events (right).

2.3 Materials and Methods

2.3.1 Inventory of Human Patient Information

Post-mortem human frontal cortex tissue was harvested and flash-frozen for long term storage in liquid nitrogen. Table 2.1 details the patient information for the data collected in the AFM experiments.

Table 2.1 Human patient information for AFM samples. A variety of pathologies were tested for control samples. Patient info column includes details about CAA and control pathologies. All AFM measurements of CAA samples were acquired on vessels containing amyloid, and all measurements of control samples were acquired on vessels with no amyloid.

	AGE	GENDER	Did measured vessels contain amyloid?	PATIENT INFO
Control #4	27	M	N	Healthy young control
UCLA A17-40	92	F	N	AD, almost no CAA
UCLA AAW16-165	65		N	Dementia with lewy bodies (vessels should be normal)
UCLA AAW16-106	78	M	N	Mild AD (Braak III-IV), mild CAA
Control #5	45	M	N	Died of basilar artery stroke
VUMC CAA5	58	M	Y	CAA, inflammatory variant
VUMC CAA6	81	M	Y	Severe CAA, hemorrhages and seizures
VUMC CAA4	71	M	Y	CAA, died of right parietal hemorrhage
VUMC CAA2	62	M	Y	CAA, without AD
UCLA AAW16-96	65	F	Y	Severe CAA (patchy) and AD

2.3.2 Preparation of Post-Mortem Human Tissue for AFM

Cryopreserved tissue chunks were sectioned by Vanderbilt University Medical Center Translational Pathology Shared Resource core at 30um/section and mounted onto the center of glass slides. Tissue was unfixed and sectioned in random orientations. Tissue sections were fixed and immunostained for CD31, VE-cadherin, and Hoechst (see section 2.3.4) to verify that each patient sample contained at least one blood vessel cross-section. Patient samples with few to no vessel cross-sections were not used for AFM measurements.

To verify that labeling tissue with Hoechst and thiazine was sufficient for identifying vessels in tissue sections, sections were fixed and stained for CD31, VE-cadherin, and Hoechst again. Sections were then imaged for all markers plus brightfield on a Leica DMi8 widefield microscope. Images of each channel, thiazine, Hoechst, and brightfield, were also acquired on the AFM before scans were performed (Figure A.2.2).

2.3.3 AFM Data Collection and Analysis

Atomic force microscopy (AFM) was performed on 30um post-mortem human tissue sections. Prior to imaging, sections were incubated with 1µg/ml Hoechst (ThermoFisher 1399) and 2µM Thiazine (Chemsavers THIR1G) for 5 minutes at room temperature to label nuceli and amyloid aggregates, respectively. Sections were subsequently mounted onto a Nikon Eclipse Ti microscope and submerged in PBS. After vessels were identified through brightfield and fluorescence channels, the Bioscope Catalyst AFM was mounted onto the microscope platform to measure vessel stiffness. AFM probes (Bruker Nano MLCT-bio-drift compensated) with a spring constant of 0.03 N/m were calibrated and then vessels were scanned at a frequency of 0.25Hz in tapping mode. 5 to 10um scan areas were captured within the vessel wall. A total of 6 vessels were measured for each condition, across ≥2 sections per condition. Each scan, consisting of 16,384 elastic modulus measurements, was averaged and resulting 6 averages were plotted as a box and whisker plot. Workflow of analysis is illustrated in Figure A.2.3.

2.3.4 Immunostaining Post-Mortem Human Tissue

10 um sections of post-mortem human tissue were fixed for 10 minutes with 4% paraformaldehyde, then photobleached for 5 hours on ice, then blocked in PBS containing 0.3% Triton-X and 5% donkey serum at room temperature for at least 1 hour. Photobleaching was crucial for removing autofluorescence in human tissue (Figure A.2.4). Sections were then incubated overnight at 4°C with primary antibodies diluted in PBS containing 5% donkey serum. Primary antibodies used were anti-TE-7 fibroblasts (Millipore CBL271, 1:100), anti-α-SMA (Millipore ABT1487, 1:1000), anti-LOX (Novus Biologicals NB100-2527, 1:50), anti-VE-cadherin (R&D Systems AF938, 1:100), anti-AOC3 (Sigma HPA000980, 1:50). On the following day, sections were washed five times with PBS at 8 minutes each. Sections were then incubated with corresponding secondary antibodies diluted in PBS containing 5% donkey serum at 1:200 for 1-2 hours at room temperature. Secondary antibodies used were donkey anti-goat Alexa Fluor 647 (Invitrogen A32849), donkey anti-mouse Alexa Fluor 555 (Thermo Fisher A31570), donkey anti-rabbit Alexa Fluor 488 (Thermo Fisher A21206). Sections were also incubated with 4 µM methoxy-X04 (Tocris 4920) for 30 minutes at room temperature following secondary antibody labeling. Four, 8 minute washes with PBS were performed, then sections were mounted using ProLong Gold antifade reagent (Invitrogen P36934).

2.3.5 Myofibroblast Quantification

10 µm tissue sections were co-stained for VE-cadherin, α-SMA, TE-7 fibroblasts, and amyloid and imaged using a Zeiss LSM 880 confocal microscope with Airy scan in the Vanderbilt Cell Imaging Shared Resource Core Facility. ImageJ was used for colocalization analysis. Regions of interest were created in the perivascular space, and pixels in the α-SMA and TE-7 fibroblast

channels were auto-thresholded. Number of colocalized pixels was quantified using the ROI tool manager. That value was then divided by the total number of TE-7 fibroblast pixels and multiplied times 100 to get percent colocalized pixels.

$$\%\ colocalized\ pixels = \frac{\#\ colocalized\ pixels}{\#\ TE-7\ fibroblast\ pixels} * 100$$

2.4 Results and Discussion

2.4.1 Vessel Stiffening in CAA

Increased deposition of ECM proteins and ECM-remodeling enzymes is associated with tissue stiffening in peripheral tissues[61]. For example, in atherosclerosis blood vessels thicken due to increased collagen deposition. To determine if increased amyloid and LOX accumulation correlates with increased tissue stiffness in CAA, we measured vessel stiffness of post-mortem human brain tissue. Hoechst and brightfield imaging of tissue sections were used to identify vessel cross-sections in the cortical tissue sections. We performed co-staining with endothelial marker CD31 to verify that these structures were blood vessels (Figure A.2.1). By atomic force microscopy, we found that CAA vessels containing amyloid were significantly stiffer than control tissue vessels, with mean stiffness values of CAA vessels ranged from 167 to 175 kPa while control vessels ranged from 36 to 68 kPa. Individual values for each condition are shown in Table A.2.1. These results show that CAA induces tissue stiffening similar to peripheral tissue stiffening[61–65].

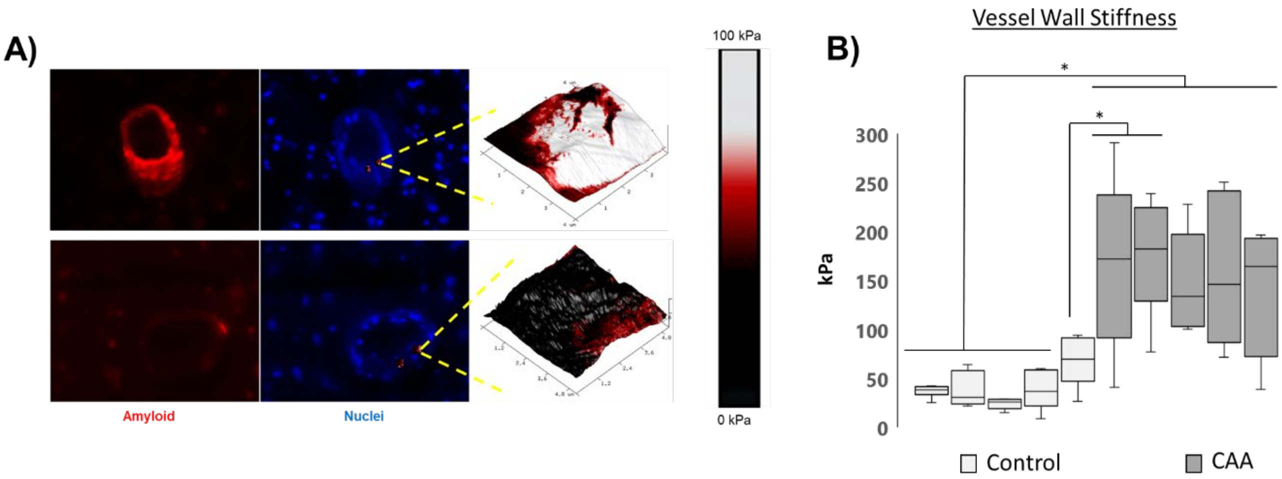

Figure 2.2 CAA vessels are stiffer than control vessels. (A) Thiazine (red) and Hoechst (blue)-labeled tissue sections were imaged then AFM probe scanned the vessel wall to measure stiffness. Heat maps indicate the stiffness values over a 5 x 5 µm scan area. (B) Vessel stiffness was measured across 10 patients (5 control and 5 CAA). 6 scans were acquired for each patient, and each scan consisted of over 16,000 stiffness measurements. Values were averaged for each scan. A one-way ANOVA with a Tukey post hoc test was used to determine statistically significant differences within each group and between control and CAA groups (*$p<0.05$).

2.4.2 LOX in CAA

Lysyl oxidase (LOX) is an enzyme that crosslinks collagen via lysine residues. It has been shown that lysine residues are essential for amyloid oligomerization and aggregation[66]. Additionally, LOX contributes to overall tissue stiffening in peripheral diseases such as fibrosis, aging and atherosclerosis[67]. LOX has been shown to colocalize to senile plaques in AD and to CAA vessels in human patient samples[68]. We aimed to confirm this finding in our tissue samples that exhibited CAA-related vascular stiffening and found that CAA vessels contained LOX signal while AD vessels with no amyloid deposition had no LOX signal (Figure 2.3). Additional confirmation of the LOX staining pattern was performed by our collaborators Dr. Matthew Schrag and Dr. Alena Shostak (Figure A.2.5). The confirmation of this marker in CAA vessels is valuable because LOX crosslinking of amyloid may contribute to stiffening.

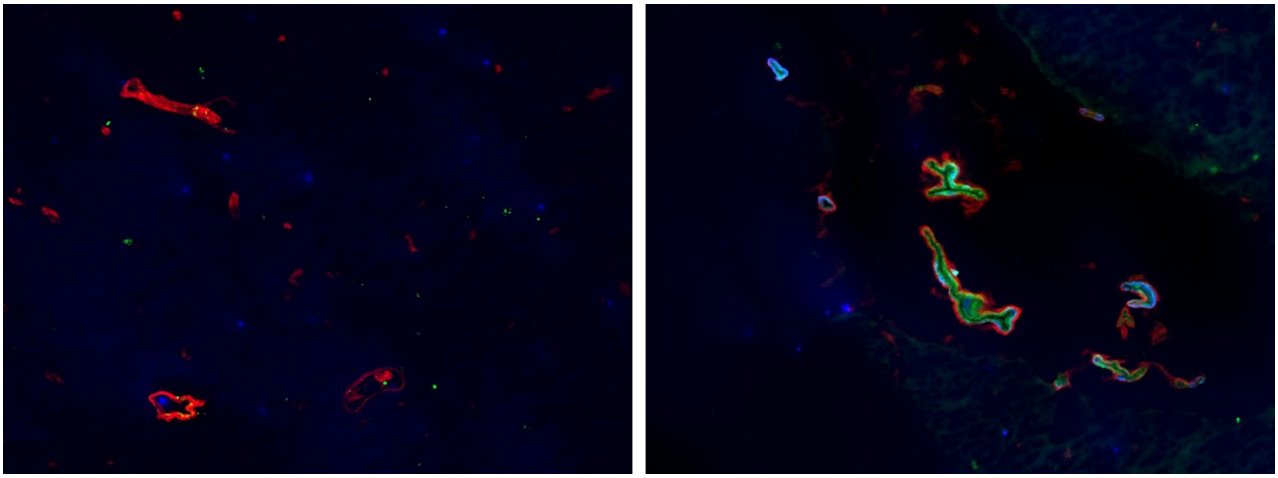

Figure 2.3 LOX in CAA vessels. CAA vessels (right image) containing amyloid (blue) are also positive for lysyl oxidase (green) whereas AD control vessels (left image) containing no amyloid are negative for lysyl oxidase. Both conditions are positive for perivascular fibroblast-like cells (red).

2.4.3 Fibrosis Markers in Perivascular Spaces of CAA Vessels

In peripheral organs, tissue stiffening and LOX accumulation are associated with fibrosis, a disease in which scar tissue accumulates and impairs organ function. For example, heightened ECM deposition in alveoli prevents proper oxygen diffusion in pulmonary fibrosis. In vascular fibrosis, thickening and stiffening of the aorta wall prevent proper distention and contraction of arteries and ultimately leads to dysregulated blood flow[69].

After we observed tissue stiffening and LOX accumulation in the CAA tissue, we chose to check for a third hallmark of fibrosis—myofibroblasts. To do this, we referred to a recent single cell RNA sequencing experiment in which a population of human brain perivascular cells were identified as fibroblast-like[70]. We first stained post-mortem human cortical tissue for the TE-7 epitope to label fibroblast-like cells and found that both control and CAA vessels contained these perivascular fibroblast-like cells. To determine if these cells were myofibroblasts, we co-stained for α-SMA, a protein that is overexpressed in myofibroblasts. We found a statistically significant increase in the number of α-SMA-positive TE-7 cells in the CAA-affected vessels versus control vessels. We verified this by staining for another marker of myofibroblasts, AOC3, and observed this marker only in CAA-affected vessels.

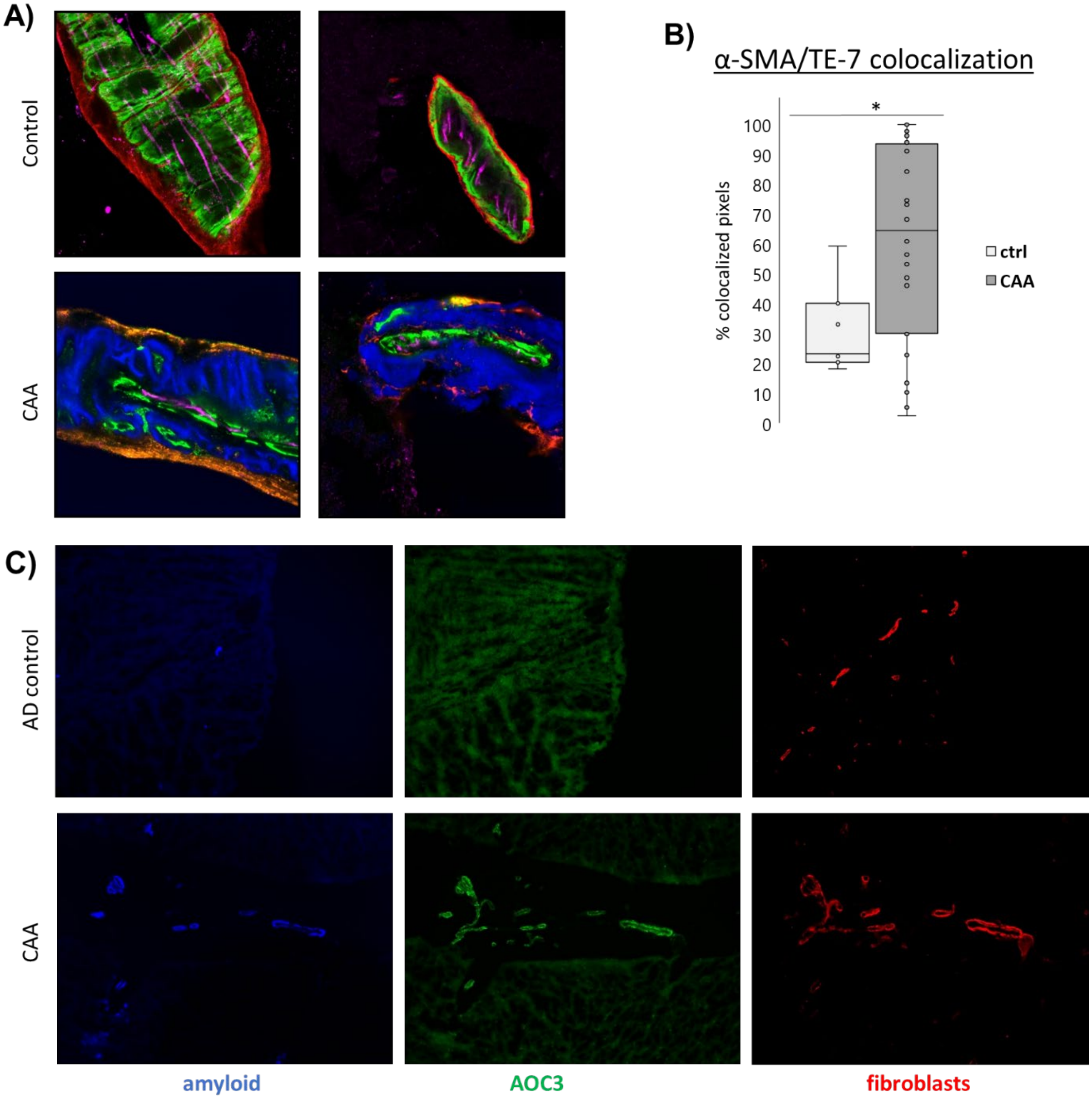

Figure 2.4 CAA vessels exhibit hallmarks of fibrosis. (A) Cortical vessels were located within 10 µm-thick tissue sections using VE-cadherin (magenta) signal. Further, CAA-affected vessels were identified by methoxy-X04 (blue). While both control and CAA vessels contained perivascular fibroblasts (red), CAA vessels exhibited colocalization of α-SMA (green) and perivascular fibroblasts, indicating the presence of myofibroblasts. (B) Colocalization of α-SMA and TE-7 fibroblasts was quantified across 3 control and 5 CAA patients. A one-way ANOVA with a Tukey post hoc test was used to evaluate the difference between control and CAA measurements (*$p<0.05$). (C) Amine oxidase enzyme (AOC3), a reported marker of myofibroblasts, is present in CAA vessels but not AD control vessels.

2.5 Conclusions

There is a growing need to better understand CAA. Our data show that CAA causes macroscale morphological changes, arteriole stiffening, and accumulation of myofibroblast markers. Stiffness was consistently increased in vessels containing amyloid deposits. Stiffness was also slightly increased in a control patient who died of basilar artery stroke, suggesting that a non-CAA vascular pathology may also contribute to stiffening. Markers of fibrosis, namely LOX and myofibroblast accumulation, are also present in CAA vessels. These parallels between CAA and fibrosis may help reveal additional CAA disease mechanisms. Additionally transgenic AD mouse models that overexpress TGF-b, another hallmark of fibrosis, have been shown to develop cognitive and vascular pathologies associated with CAA[71].

In comparison to neuronal tau tangles and parenchymal amyloid plaques, the contribution of vascular pathologies to AD has traditionally been understudied. Approximately 90% of AD patients also have CAA, and 40% have some form of vascular cognitive impairment and dementia (VCID)[17–20]. Behind AD, VCID is the second most common cause of dementia. Many mouse AD models, however, do not include vascular pathologies. When the vascular pathologies were introduced to a mouse model for AD, treatment with an amyloid-targeting drug made the vascular pathology worse[21]. Although reductions in amyloid burden were observed, an increase in microhemorrhages negated any cognitive benefits that may have resulted from amyloid clearance. Additionally, in clinical trials where amyloid plaques were cleared, CAA perisisted[72]. These findings suggest that vascular contributions to AD may be crucial to understanding and combatting cognitive decline.

2.6 Appendix

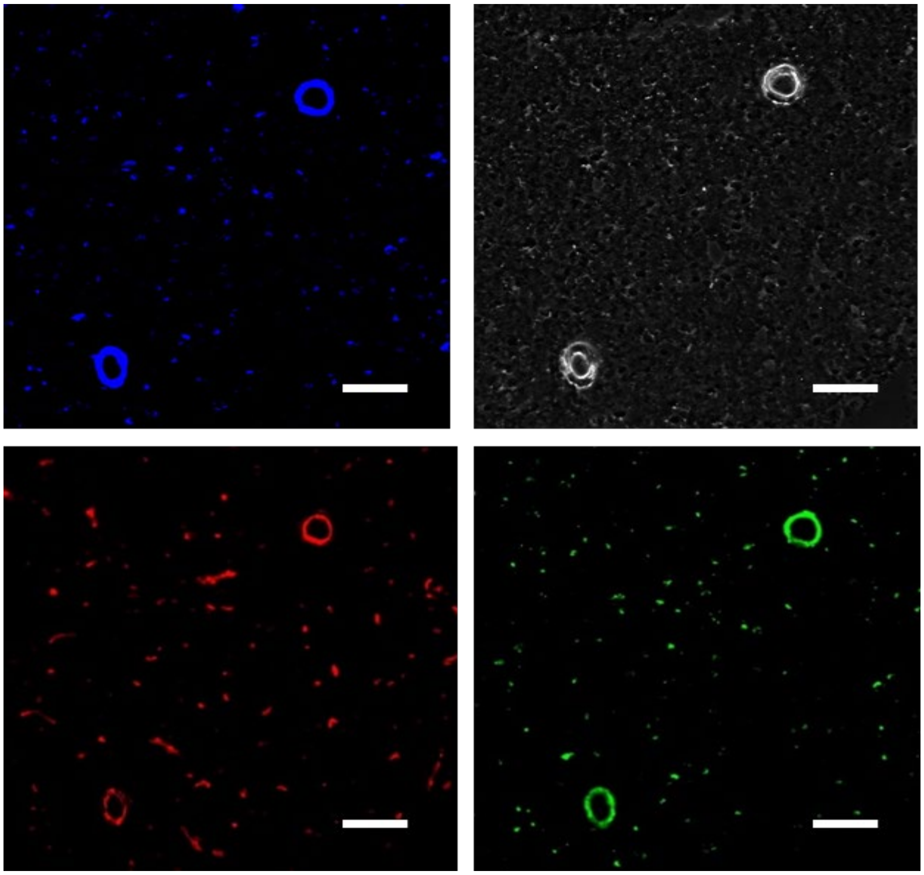

Figure A.2.1 Hoechst is sufficient for identifying arterioles in tissue sections. Human tissue sections were incubated with Hoechst (blue) and lectin (green) to label vessels. To verify that these structures were blood vessels, tissue was co-stained with an antibody for CD31 (red), a vascular endothelial cell marker. Vessels can also be visualized in the brightfield channel (grey). Scale bars represent 100 µm.

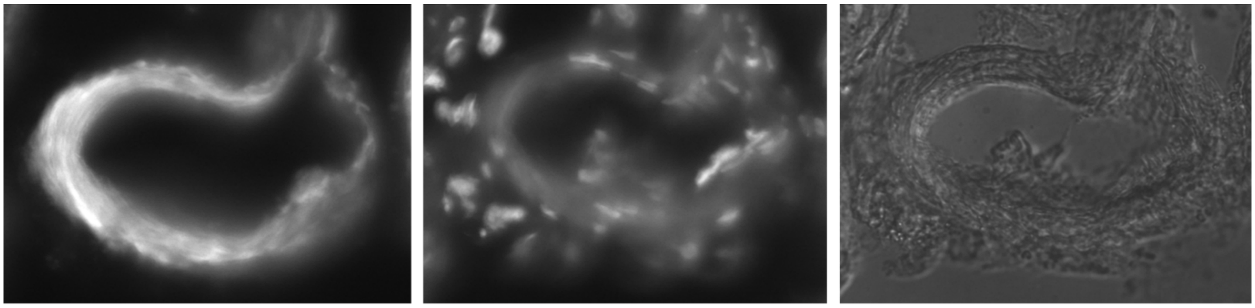

Thiazine Hoechst Brightfield

Figure A.2.2 CAA vessel markers imaged on AFM. Images acquired for each channel on AFM microscope. When scanning tissue, Hoechst channel was used to find vessels, and thiazine channel was used to determine if vessel was affected by CAA.

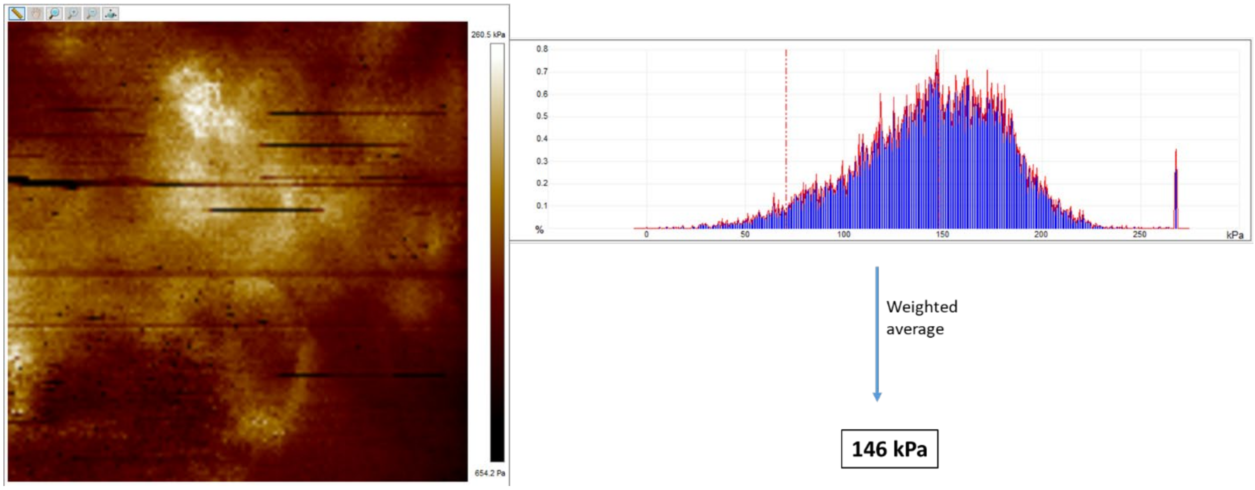

Figure A.2.3 AFM scan analysis workflow. Individual scans (left) containing ~16,000 individual modulus measurements were binned into 500 measurements. A weighted average was performed to generate one stiffness value for the scan area.

Table A.2.1 Average stiffness values for each patient sample. Six scans were performed for each patient sample. Data was analyzed according to the workflow in Figure A.2.3, and averages for each scan are reported here along with overall averages and standard deviation for each patient sample.

	Ctrl 4	**A17-40**	**16-165**	**16-106**	**Ctrl 5**	**CAA5**	**CAA6**	**CAA4**	**CAA 2**	**16-96**
scan data	40.01	21.98	24.36	43.23	71.76	219.26	186.69	142.84	189.72	238.86
	36.98	25.49	27.12	58.52	90.91	185.83	228.02	91.55	191.83	146.30
	42.53	35.47	28.45	29.69	67.98	108.44	122.00	250.73	83.57	220.09
	25.34	55.76	28.39	26.27	94.04	40.84	146.07	71.37	196.26	198.87
	41.19	63.79	20.46	60.17	54.26	157.83	104.17	238.68	139.58	77.36
	35.64	24.28	14.80	8.79	26.70	290.63	100.23	149.07	39.15	165.91
AVG	36.95	37.79	23.93	37.78	67.61	167.14	147.86	157.37	140.02	174.57
STDEV	6.25	17.82	5.41	20.00	24.94	86.95	50.56	73.94	65.85	58.51

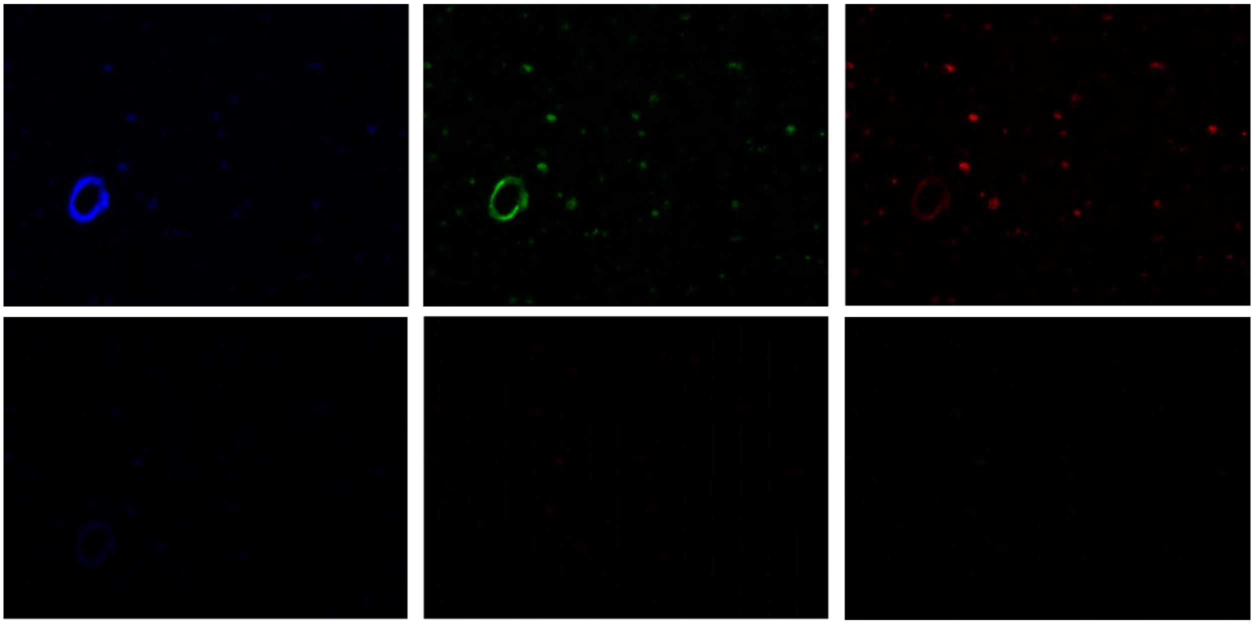

Figure A.2.4 Photobleaching conditions to minimize autofluorescent signal in human tissue. Human tissue sections were imaged before (top) and after (bottom) a 5-hour exposure to an LED array of visible light. Imaging parameters were kept consistent for both imaging experiments. Autofluorescent signal in the blue, green, and red channels is minimized after photobleaching step is performed.

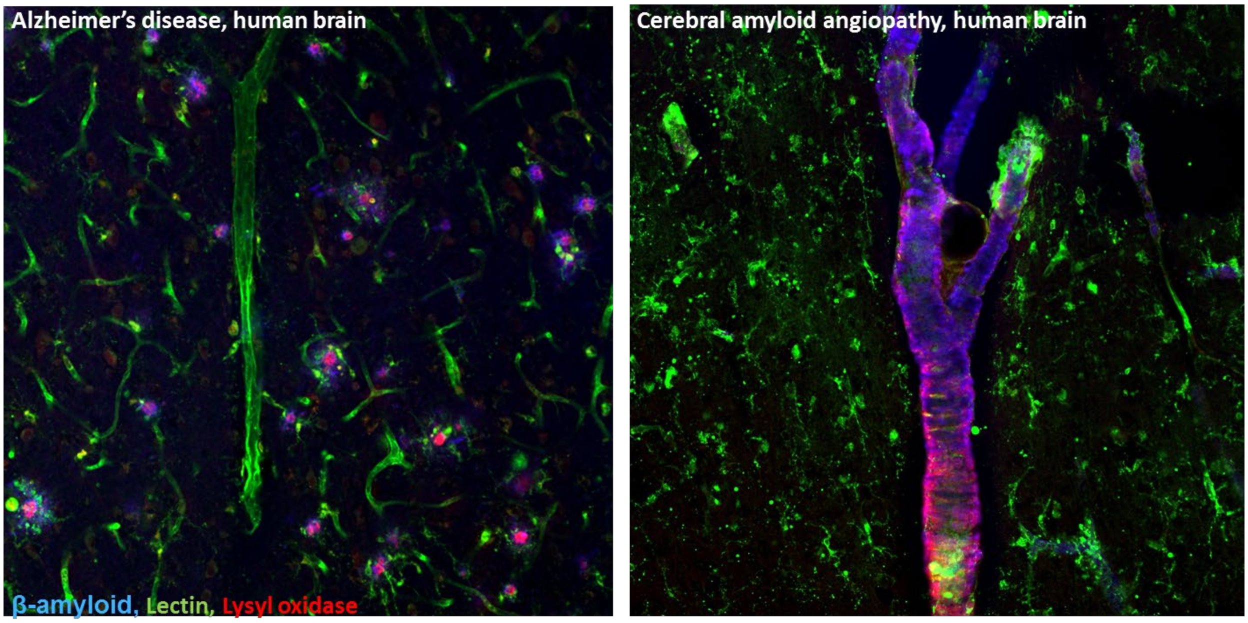

Figure A.2.5 CLARITY imaging of lysyl oxidase in human cortical tissue. In both AD plaques and CAA vascular deposits, LOX (red) colocalizes to areas of amyloid aggregation (blue). Images acquired by Schrag lab in the Vanderbilt University Medical Center.

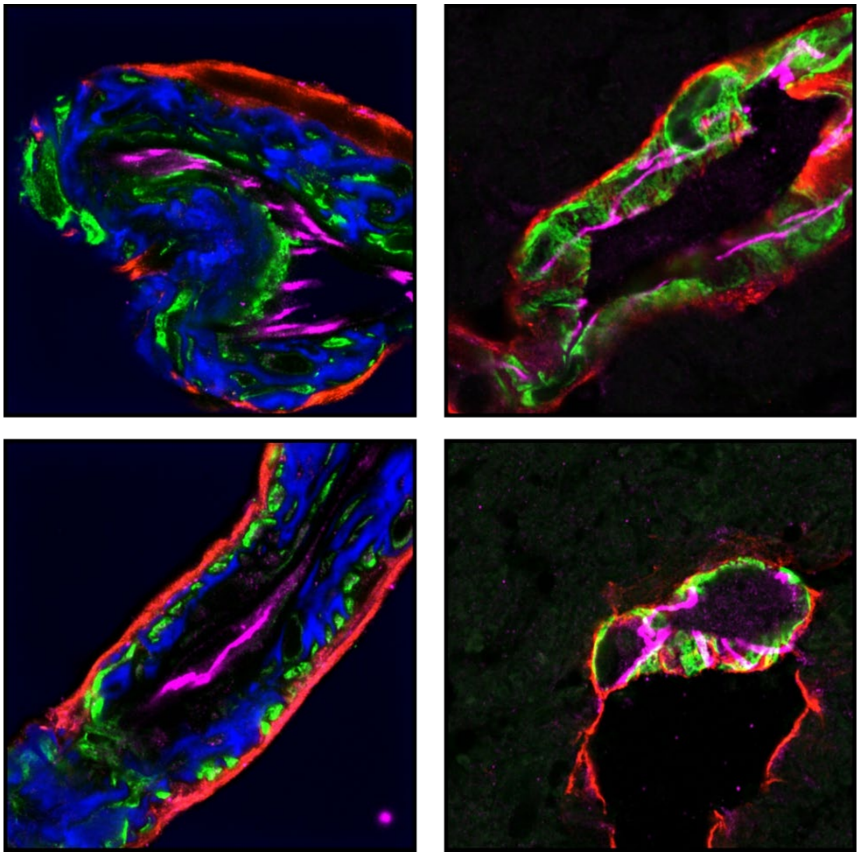

Figure A.2.6 CAA vessels without myofibroblasts. CAA tissue exhibited heterogeneity in myofibroblast presentation. Figure 2.4 illustrates the CAA vessels with positive myofibroblast markers, and vessels from CAA patients that are negative for myofibroblasts markers can be seen here. Vessels affected by CAA (left) contain amyloid aggregates (blue), however, the perivascular fibroblasts (red) did not show colocalization of α-SMA (green). Vessels lacking amyloid (right) also did not show colocalization. Vessels were identified within tissue sections by VE-cadherin signal (magenta).

Chapter 3

INFLUENCE OF SUBSTRATE STIFFNESS ON BARRIER FUNCTION IN AN IPSC-DERIVED IN VITRO BLOOD-BRAIN BARRIER MODEL

Adopted from: Bosworth AM, Kim H, O'Grady KP, Richter I, Lee L, O'Grady BJ & Lippmann ES. Influence of substrate stiffness on barrier function in an iPSC-derived in vitro blood-brain barrier model. Cellular and Molecular Bioengineering, In Review, *with permission from Springer Publishing.*

3.1 Summary

Vascular endothelial cells respond to a variety of biophysical cues such as shear stress and substrate stiffness. In peripheral vasculature, extracellular matrix (ECM) stiffening alters barrier function, leading to increased vascular permeability in atherosclerosis and pulmonary edema. The effect of ECM stiffness on blood-brain barrier (BBB) endothelial cells, however, has not been explored. To investigate this topic, we incorporated hydrogel substrates into an in vitro model of the human BBB.

Induced pluripotent stem cells were differentiated to brain microvascular endothelial-like (BMEC-like) cells and cultured on hydrogel substrates of varying stiffness. Cellular changes were measured by imaging, functional assays such as transendothelial electrical resistance (TEER) and p-glycoprotein efflux activity, and bulk transcriptome readouts.

The magnitude and longevity of TEER in iPSC-derived BMEC-like cells is enhanced on compliant substrates. Quantitative imaging shows that BMEC-like cells form fewer intracellular actin stress fibers on substrates of intermediate stiffness (20 kPa relative to 1 kPa and 150 kPa). Chemical induction of actin polymerization leads to a rapid decline in TEER, agreeing with imaging readouts. P-glycoprotein activity is unaffected by substrate stiffness. Modest differences in RNA expression corresponding to specific signaling pathways were observed as a function of substrate stiffness.

iPSC-derived BMEC-like cells exhibit differences in passive but not active barrier function in response to substrate stiffness. These findings may provide insight into BBB dysfunction during neurodegeneration, as well as aid in the optimization of more complex three-dimensional neurovascular models utilizing compliant hydrogels.

3.2 Introduction

Endothelial cells (ECs) line blood vessels and perform vital organ-specific functions. Within the blood vessel architecture, ECs sit on an intimal basement membrane which is surrounded by smooth muscle cells or pericytes depending on the location along the vascular tree. Due to their barrier properties, ECs play a key role in shuttling substances between the parenchyma and the bloodstream. ECs are known to respond to a variety of extracellular mechanical cues5, including shear flow, bifurcations, topography, curvature, matrix composition, and stiffness8,14,32. These properties can impart a positive or negative effect on EC barrier function, and the sensitivity of ECs to mechanical cues can impact a variety of disease states8.

Stiffness, in particular, has been shown to increase permeability of endothelial barriers and limit contraction of larger vessels. Across all vessel sizes, there are reports of ubiquitous changes in EC function as the underlying substrate becomes more stiff. For example, in vitro experiments have been used to demonstrate that, when placed on stiffer substrates, aortic endothelial cells exhibit increased permeability and leukocyte transmigration13, and lung microvascular endothelial cells exhibit decreased transendothelial electrical resistance (TEER) and discontinuous junctions22. Pulse wave velocity measurements of human vessels have shown that macroscale vessel stiffness increases in aging and atherosclerosis6, and these changes disrupt endothelial barriers35. Some of the mechanisms that transduce mechanical cues into barrier modifications have been illustrated as well, for example that cellular cytoskeleton and contractility are altered on stiffer matrices and negatively affect endothelial permeability1,13. However, the connections between stiffness and endothelial barrier function have thus far only been assessed for peripheral endothelial cells and not those with more stringent barrier properties, such as specialized brain microvascular endothelial cells (BMECs) that form the blood-brain barrier (BBB). BMECs are distinguished from peripheral ECs by the presence of complex tight junctions, higher mitochondrial content, lack of fenestrations, and very little pinocytosis10, which are critical features that help maintain neural function and brain homeostasis31. BMECs exhibit very high TEER, highlighting their ability to limit molecular transport along paracellular pathways. Additionally, BMECs express a variety of membrane transporters to actively shuttle molecules into and out of the brain along transcellular pathways. Altogether, these properties allow the BBB to strictly regulate the transport of compounds between the bloodstream and the brain. At present, it has not been assessed whether BMECs and their specialized BBB properties are influenced by underlying substrate stiffness.

BMECs have historically been difficult to study in vitro because they lose BBB characteristics after removal from the in vivo microenvironment29. This challenge has been partially circumvented in recent years by the advent of human pluripotent stem cell technology, which has permitted the generation of endothelial-like cells with robust BBB properties20,21. Previous work from our group demonstrated that these human induced pluripotent stem cell (iPSC)-derived BMEC-like cells respond to shear stress when cultured as a perfusable macrovessel structure. When cultured under constant shear, iPSC-derived BMEC-like cells were 10-100 times less permeable to 3 kDa dextran relative to those cultured under static conditions.7 Different perfusion rates also yielded changes to dextran permeability and induced angiogenic-like sprouting into the surrounding hydrogel, which indicated that iPSC-derived BMEC-like cells are sensitive to mechanical cues. However, the response of iPSC-derived BMECs to the stiffness of the underlying substrate was not explicitly tested. Here, we sought to further characterize how iPSC-derived BMEC-like cells respond to stiffness cues using hydrogels, functional assays, and molecular biology tools. We determined that, in agreement with general mechanobiology trends, iPSC-derived BMEC-like cells develop tighter barriers on hydrogels with intermediate stiffness that match healthy vessel intima. These cells reorganize actin into intracellular stress fibers when substrate conditions are too soft or too stiff, and small molecule-mediated induction of actin polymerization yielded a rapid reduction in TEER, suggesting links between actin structure and passive BBB function. Finally, RNA sequencing was used to provide further insight into how iPSC-derived BMEC-like cells respond to culture on substrates of varying stiffness. We suggest that our findings will be useful towards fabricating more complex 3D BBB models that involve hydrogels and may be interesting for studies of vascular dysfunction in neurodegeneration.

3.3 Materials and Methods

3.3.1 Polyacrylamide Hydrogel Preparation

For coverslip-bound hydrogels, activated coverslips and polyacrylamide (PA) hydrogels were prepared as previously reported4. 15 mm circular glass coverslips (Carolina 633011) were exposed to oxygen plasma for 6 minutes, incubated with a 0.1% polyethyleneimine (Sigma P3143) solution for 10 minutes, washed three times in deionized water for 5 minutes each, and incubated with 0.5% glutaraldehyde (Sigma G7776) for 30 minutes. Three additional 5 minute washes were performed, and activated coverslips were dried overnight in fume hood.

Stock 40% acrylamide (BioRad 1610140) and 2% bis-acrylamide (BioRad 1610143) solutions were diluted in ultrapure water at varying concentrations to yield hydrogels of varying stiffness. Final concentrations of 3% A and 0.1% B, 15% A and 0.1% B, 15% A and 1.2% B were used to fabricate hydrogels at 1 kPa, 20 kPa, and 150 kPa, respectively. To fabricate the gels, these PA solutions were degassed for 1 hour, then TEMED (BioRad 1610801) and ammonium persulfate (APS) (BioRad 1610700) were added to initiate polymerization. For each milliliter of PA solution, 1 µl of TEMED and 5 µl of a freshly reconstituted 10% APS solution were added. 35 µl of this solution was immediately sandwiched between a Rain-X-coated microscope slide and the activated coverslip. Polymerization occurred for 2030 minutes before gels were unmolded to reveal a coverslip-bound gel of 0.2 mm thickness.

Hydrogels were incubated in a 50 mM HEPES (Sigma 391340) buffer of pH 8 for at least 30 minutes on a rocking plate at room temperature before being coated with a sulfo-SANPAH (SS) (CovaChem 13414-5x5) linker. SS was reconstituted in aforementioned HEPES buffer at 0.5 mg/ml and immediately pipetted onto the gel surface. PA gels were exposed to 110 mJ/cm2 of UV light (UVP CL-1000 UV Crosslinker) for 10 minutes. Once this exposure was completed, fresh

SS was added to the gels, and a second UV exposure was performed. Then, PA gels were washed twice in HEPES buffer for 15 minutes on a rocking platform to remove excess, unbound SS. Following the washes, the PA gels were incubated with extracellular matrix protein (ECM) solutions overnight at 4°C. To prepare the protein solution, collagen type IV (Sigma C5533) and fibronectin (Sigma 1141) were diluted in sterile HEPES buffer to final concentrations of 0.4 and 0.1 mg/ml, respectively.

For TEER measurements, PA hydrogels were polymerized in Transwell filter inserts (Fisher Scientific 07-200-161). These PA gels used an N-6-((acryloyl)amino)hexanoic acid, succinimidyl ester linker as opposed to the sulfo-SANPAH linker because we were unable to polymerize sulfo-SANPAH-linked gels in a Transwell filter with a smooth surface (data not shown). The N-6 linker was synthesized through the Vanderbilt Chemical Synthesis Core according to established methods13. N-6 PA gels were prepared as described previously[48,73]. 3, 15, 55 kPa hydrogel precursor solutions contained 5.4%:0.01%, 8%:0.02%, 13%:1.1% acrylamide: bisacrylamide, respectively. After samples degassed for 1 hour, 5.6 mg of N-6 was reconstituted in 70 µl of ethanol and added to 845 µl of PA solution along with TEMED and APS to initiate polymerization. 350 µl of this solution was added to each transwell insert. Well plate containing transwell inserts was placed into an environmental chamber without the plate lid, and chamber was flushed with nitrogen gas for 2 minutes. Polymerization occurred for 20 minutes, then the well plate was removed from the chamber and protein solution was added to gel surface. The same ECM protein solution was used for N-6 and sulfo-SANPAH gels. 250 µl of ECM protein solution was added to each gel and incubated for 2 hours at 4°C. Gels were then incubated with ethanolamine at room temperature for 30 minutes, with 1.5 ml in the basolateral chamber of the and 0.5 ml in the apical chamber of the Transwell filter.

After overnight incubation, hydrogels were submerged in 5% PenStrep for 4 hours at room temperature in preparation for cell seeding. After 4 hours, gels were rinsed 3 times with sterile, ultrapure water, then incubated with DMEM/F12 for 30-60 minutes at 37°C prior to cell seeding.

3.3.2 Gelatin Hydrogel Fabrication

Gelatin from porcine skin (Sigma G1890) was reconstituted in water at 10% (w/v), then further diluted to produce 7.5%, 5%, and 2.5% gelatin solutions. 10 mL of each solution was mixed with 1 mL of a 10% (w/v) solution of microbial transglutaminase (Modernist Pantry 1203-50) in water. This precursor solution was thoroughly mixed by pipetting. To polymerize hydrogels in Transwell filters, 350 uL of precursor solution was pipetted onto the top of the filter. To produce hydrogels bound to coverslips, 130 uL of precursor solution was sandwiched between Rain-X-coated microscope slides and glutaraldehyde-activated coverslips. For both Transwell and coverslip formats, precursor solutions were incubated overnight for 1 hour at 37°C to crosslink. Hydrogels on Transwells were incubated with ECM solution overnight for adsorption in preparation for cell seeding. ECM solution was prepared at same concentrations as mentioned above, but proteins were diluted in sterile water instead of HEPES buffer. Coverslip hydrogels were not coated with ECM.

3.3.3 Quantifying Stiffness of Gels by Atomic Force Microscopy

Stiffness of hydrogels was quantified using a Bruker Dimension Icon Atomic Force Microscope in the Vanderbilt Institute for Nanoscale Science and Engineering. Both sulfo-SANPAH PA hydrogels and gelatin hydrogels were prepared as coverslip-bound gels for atomic force microscopy (AFM) measurements. Coverslips were glued to microscope slides and measurements were performed in fluid. PA hydrogels were measured using Bruker pre-calibrated PFQNM-LC-A probes with a nominal spring constant of 0.1 N/m and a tip radius of 70 nm, and gelatin hydrogels were measured using Novascan pre-calibrated PT.PS.SN.4.5.CAL probes with a nominal spring constant of 0.01 N/m and a tip radius of 2.25 µm. were used to measure tThree distinct 5x5 micron areas were measured across three hydrogels for each condition, totaling 9 captures per condition. The resulting force curves for each condition were baseline corrected, and Young's Modulus was calculated according the Hertzian model. Values for each condition were averaged to produce the reported stiffness values found in Figures 1 and 2.

3.3.4 Differentiation of iPSCs to BMEC-like Cells

iPSCs were maintained and differentiated as previously described[74,75]. For all experiments, to initiate differentiation, CC3 iPSCs were seeded in E8 medium containing 10 µM Y27632 (Fisher Scientific 12-541-0) at 12,500 cells/cm^2. Then, 24 hours after seeding, cells were switched to E6 medium and daily media changes were performed for four days.

From this point, different routes were taken depending on the experiment and hydrogel substrate. For experiments on gelatin hydrogels, we started with an older differentiation procedure that utilized serum-containing medium[74]. Briefly, on day 4 of differentiation, media was changed to the following formulation of EC medium: human endothelial serum-free medium (hESFM, Thermo Fisher 1111044) supplemented with 1% platelet-poor plasma-derived serum (PDS, Fisher AAJ64483AE), 10 µM retinoic acid (RA, Sigma R2625), and 20 ng/mL basic fibroblast growth factor (bFGF, Peprotech 100-18B). No media change was performed on day 5. On day 6, cells were dissociated in Accutase for 15-20 minutes (or until approximately 70% of cells had visibly dissociated), centrifuged, and replated in the same EC medium onto gelatin hydrogels cast in Transwell filters, as described above. Cells from 3 wells of a 6-well plate were split across 9

Transwell filters. 24 hours later, media was aspirated and changed to fresh EC medium containing PDS but without RA or bFGF. No further media changes were performed.

For experiments on PA hydrogels and standard Transwell filters, we utilized newer variations of our protocol that remove serum from the differentiation procedure[75,76]. Here, on day 4 of differentiation, media was switched to updated EC medium: Neurobasal (Thermo Fisher 21103049) with 0.25% GlutaMAX (Thermo Fisher 35050061), 0.5% B27 supplement (Thermo Fisher 17504044), 10 µM RA, and 20 ng/mL bFGF. No media change was performed on day 5. On day 6, cells were dissociated in Accutase for 15-20 minutes (or until approximately 70% of cells had visibly dissociated), centrifuged, and replated onto polyacrylamide hydrogels or standard Transwell filters. If seeding onto hydrogels, cells were plated in the aforementioned EC medium containing 0.1% PDS and 1 µM Y27632 (Tocris 1254) to facilitate adhesion. If seeding onto Transwell filters coated with 0.4 mg/ml collagen IV and 0.1 mg/ml fibronectin, cells were plated in the same EC medium utilized at day 4. Cells from 2 wells of a 6-well plate were split across 3 hydrogels or 6 Transwell filters. 24 hours later, media was aspirated and changed to fresh EC medium containing B27 but without RA, bFGF, PDS, and Y27632. No further media changes were performed.

3.3.5 TEER Measurements

For experiments on hydrogel substrates, TEER was measured using an EVOM2 voltohmeter with EndOhm cup chamber (World Precision Instruments ENDOHM-12g) filled with pre-warmed hESFM medium. Each day, height of the upper electrode was set according to an empty gel Transwell containing no cells. Resistance values were recorded for the empty gel Transwells and for the sample conditions. For experiments on cells cultured directly on Transwell filters, TEER was measured using an EVOM2 voltohmeter with STX3 chopstick electrodes (World Precision Instruments). 0.13 µM jasplakinolide (jasplak; Thermo Fisher J7473) was added directly to the cell culture medium, and equivalent volumes of DMSO were added as the vehicle control. Resistance values were recorded from an empty Transwell containing no cells and for the samples conditions. For all experiments, empty measurements were subtracted from sample measurements, and the resulting values were multiplied by 1.1 cm^2 surface area of the filter.

3.3.6 P-glycoprotein Efflux Assay

Efflux assays were performed on BMEC-like cells 8 days after seeding onto hydrogels. 10 µM Cyclosporin A (Fisher Scientific 11-011-00) was added to the cell culture media and incubated for 1 hour at 37°C. Cells were then incubated with 10 µM Rhodamine 123 (Thermo Fisher R302) and 10 µM Cyclosporin A in fresh EC medium for 1 hour at 37°C. Cells were then rinsed with PBS, scraped off the gel surface and transferred to a microfuge tube containing TryplE (Thermo Fisher 12604013). Triplicate gels of each condition were pooled, and triturations were performed until no visible cell clumps remained. Cells were re-centrifuged and resuspended in flow buffer (PBS containing 5% donkey serum). Flow cytometry was performed using a Guava easy-Cyte benchtop flow cytometer. Events were plotted as forward scatter versus green fluorescence, and rhodamine-positive cells were identified against BMEC-like cells that received no rhodamine or cyclosporin.

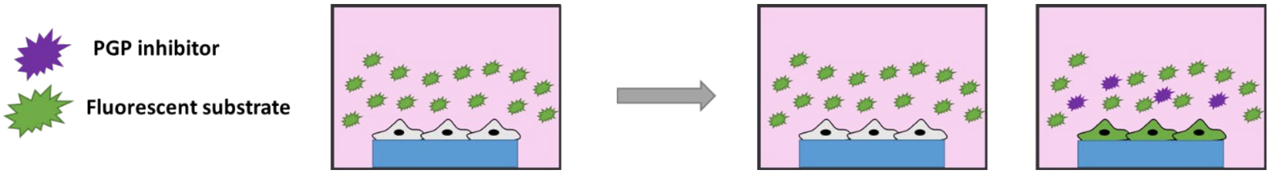

Figure 3.1 Workflow of P-glycoprotein efflux assay. BMECs adhered to PA gels are incubated with a fluorescent substrate of PGP. Increased accumulation of the fluorescent substrate corresponds to less efflux activity. Pre-incubation with a PGP inhibitor serves as a control in which little to no fluorescence is effluxed and accumulation is high.

3.3.7 Immunostaining BMECs on Polyacrylamide Substrates

Cells were rinsed twice with PBS and fixed for 10 minutes in 4% paraformaldehyde. Then, cells were washed three times in PBS containing 0.3% Triton-X, referred to as PBS-T, for 5 minutes each. After washes, cells were blocked in PBS-T containing 5% donkey serum at room temperature for at least 1 hour. Cells were then incubated overnight at 4°C with an occludin primary antibody (Thermo Fisher 33-1500) at 1:200 in PBS containing 5% donkey serum. On the following day, cells were washed five times in PBS-T at 8 minutes each. A donkey anti-mouse Alexa Fluor 647 secondary antibody (Thermo Fisher A31571) was diluted at 1:200 in PBS containing 5% donkey serum and applied to cells for a 1-2 hour incubation at room temperature. Cells were then incubated with Phalloidin-488 (Thermo Fisher A12379) at 1:1000 for 30 minutes and Hoechst (Thermo Fisher H1399) at 1 µg/mL for 10 minutes. Four more washes in PBS-T were performed at 8 minutes each, and cells were mounted onto microscope slides for imaging.

3.3.8 Image Analysis and Quantification

For qualitative assessment of cell confluence, brightfield images were acquired using an EVOS XL Core Imaging System. For quantification of actin stress fibers and tight junction integrity, phalloidin and occludin were imaged using a Zeiss LSM 880 confocal microscope in the Vanderbilt Cell Imaging Shared Resource Core Facility. Actin stress fibers were manually counted by a blinded observer. Occludin labeling was overlaid during counting to ensure that only intracellular fibers were counted.

For quantification of tight junction width and tortuosity, image processing was performed in Matlab (MathWorks, Inc.). First, fluorescence images of occludin were filtered with a two-dimensional Hessian filtering algorithm to enhance contrast using a modification of methods described previously[77,78]. In the filtering step, junctions oriented in any direction were detected using the eigenvalues of the image, and detection was performed over multiple scales. The raw image was then scaled using the maximum filter response for each pixel, and the resulting image was thresholded to produce a binary mask of the tight junctions. The binary mask was skeletonized to find the centerline pixels of all junctions, and the junction width at each centerline pixel was computed. To estimate tortuosity of the junctions, the straight-line distance was computed between branch points in the skeletonized image, and the actual total length of the junctions was divided by the total straight-line distance (ratios closer to 1 indicate junctions are less tortuous).

3.3.9 Bulk RNA Sequencing

On day 8 after purification, BMEC-like cells were detached from PA hydrogel surfaces with a 10 minute Accutase incubation at 37°C. Cells from 3 gels of each stiffness condition were pooled to create one biological replicate. Cells were then rinsed with PBS and incubated in Trizol (Thermo

Fisher 15596026) for 10 minutes at room temperature. RNA was extracted using a Direct-zol RNA miniprep kit (Zymo R2050) according to the manufacturer's instruction. This process was repeated two additional times from independent iPSC differentiations (biological n=3).

RNA samples were submitted to the Vanderbilt Technologies for Advanced Genomics (VANTAGE) facility for sequencing using an Illumina NovaSeq6000. Raw sequencing reads were obtained for the 9 paired-end samples. FASTQ reads were mapped to human genome (hg19) by HISAT2 (version 2.1.0). Gene expression levels were estimated through String Tie. EdgeR (version 3.30.3) was used to measure differential gene expression, and genes with $p<0.05$ were utilized for Gene ontology (GO) enrichment analysis with the WEB-based GEne SeT AnaLysis (WebGestalt) Toolkit[79]. Results were annotated with functional database IDs and false-discovery rates for each signaling pathway.

3.3.10 Phospho-kinase Array

Baseline levels of phosphorylation of 43 common phosphorylation sites were measured using an array kit (R&D Systems ARY003B). On day 7 after purification, iPSC-derived BMEC-like cells were manually scraped off of hydrogels. Protein isolation and incubation with array membranes was performed according to manufacturer's protocol. Membranes were imaged via chemiluminescence on a LiCor Odyssey Fc imager. Spot intensities on the membrane were quantified using Image Studio Lite software.

3.4 Results and Discussion

3.4.1 iPSC-derived BMEC-like cells exhibit improved passive barrier function on compliant gelatin hydrogels

To initially examine the influence of stiffness on passive barrier function, we crosslinked gelatin hydrogels in Transwell filters and measured TEER in iPSC-derived BMEC-like cells. We utilized an older variant of our differentiation protocols that contained serum throughout the differentiation process and after purification of the iPSC-derived BMEC-like cells[74] (Figure __). We manipulated the gelatin concentration (2.5, 5, and 7.5 weight percent), which resulted in hydrogel stiffnesses of 0.3, 2.5, and 5 kPa respectively (Figure __). Intriguingly, while cells on 2.5% gelatin hydrogels exhibited either similar or lower TEER maxima than cells on control Transwell filters, cells cultured on 5% and 7.5% gelatin exhibited significantly higher TEER maxima, as well as enhanced barrier longevity (Figure 3.2). In particular, iPSC-derived BMEC-like cells cultured on 7.5% gelatin hydrogels reach a significantly higher TEER maximum with respect to the softer substrates and the no hydrogel control. These results suggest that passive barrier function of iPSC-derived BMEC-like cells is sensitive to the stiffness of the underlying substrates.

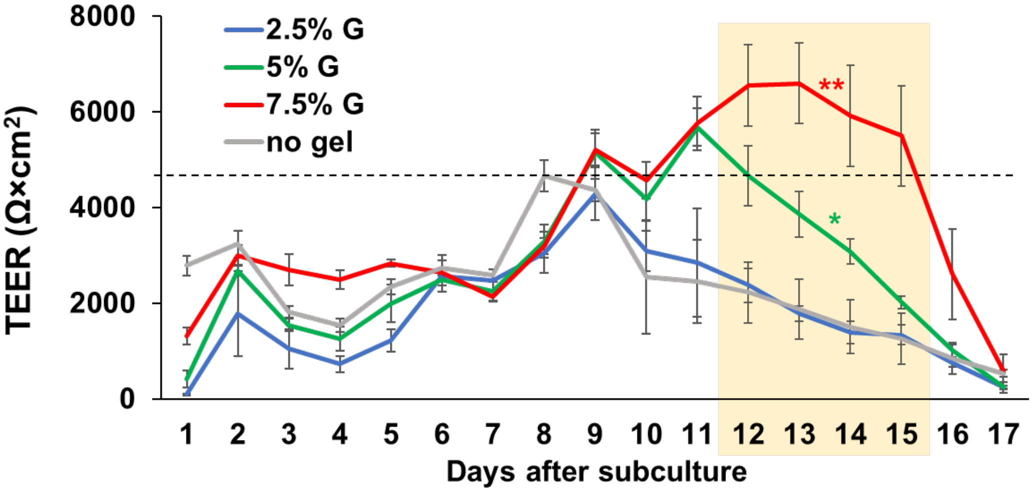

Figure 3.2 Representative TEER plot for iPSC-derived BMEC-like cells cultured on gelatin hydrogels. 3 filters were prepared for each condition, and each filter was measured in triplicate. Values for each day represent mean ± standard deviation from these 9 measurements. The dotted line indicates maximum average TEER achieved by the no hydrogel control. A one-way ANOVA with a Tukey post hoc test was performed for days 12-15 (yellow box), which showed that the 7.5% and 5% gelatin hydrogels had significantly elevated TEER relative to the 2.5% gelatin hydrogel and no hydrogel control on each day (*$*p<0.05$, $**p<0.01$*). These trends were confirmed across an additional biological replicate.

3.4.2 Optimized seeding of iPSC-derived BMEC-like cells on polyacrylamide hydrogel substrates

The stiffness of ECM-based hydrogels can be tuned by modifying protein concentration, but this can also result in differences in porosity and altered cell-ECM interactions (for example, differential presentation of RGD ligands as a function of increased ECM content). To enable more controlled studies and to test a wider range of stiffness conditions, we transitioned to the use of polyacrylamide (PA) hydrogels. Here, we synthesized PA hydrogels by varying acrylamide and bis-acrylamide concentrations, which tuned the stiffness of the hydrogels as expected (Figure __). Since PA is biologically inert, we covalently tethered collagen IV and fibronectin, which are crucial for adhesion of iPSC-derived BMEC-like cells[75]. We chose to synthesize PA hydrogels with stiffness conditions that represent: 1) bulk brain stiffness (0.2-2 kPa), 2) healthy peripheral vessel intimal stiffness (20-30 kPa), and 3) diseased peripheral vessel intimal stiffness (>50 kPa)[80,81].

Here, we utilized newer variants of our iPSC differentiation protocols that replace the serum component in the culture medium with more defined B27 supplement[75]. However, we subsequently determined that iPSC-derived BMEC-like cells did not adhere to PA hydrogel surfaces as confluent monolayers unless serum (PDS) and ROCK inhibitor (Y27632) were included in the medium (Figure 3.3A). Serum and Y27632 have been shown to promote cell survival during passaging[82] and were clearly necessary for attachment to the synthetic hydrogels, and supplementation of these factors did not hinder barrier function (Figure 3.3B). We thus moved forward with this system for downstream analyses of cell phenotype and function. To avoid confounding effects of serum, we decreased its concentration to 0.1% and only included it for one day to assist with adherence to the PA hydrogels. Likewise, because ROCK inhibitors influence mechanosensing, Y27632 was only included for one day. All subsequent analyses were conducted 8 or 15 days after placing the BMEC-like cells onto hydrogels.

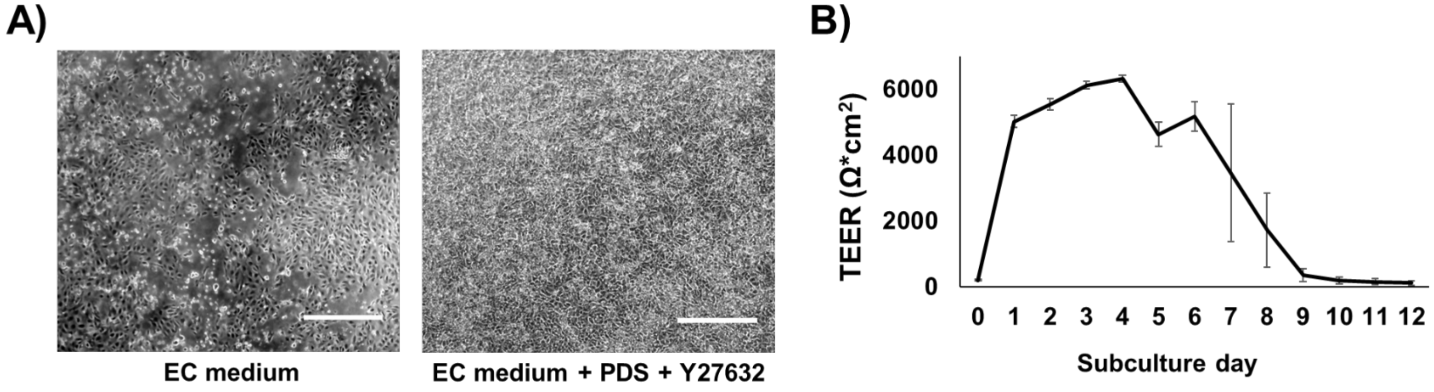

Figure 3.3 Optimization of subculture protocol for polyacrylamide stubstrates. (A) Brightfield images showing that iPSC-derived BMEC-like cells sporadically adhere to PA hydrogel surfaces in base EC medium but form confluent monolayers when base EC medium is supplemented with PDS and Y27632 for 24 hours. Scale bars are 250 µm. (B) With inclusion of PDS and Y27632, BMEC-like cells still achieve physiological TEER values.

3.4.3 Stiffness of polyacrylamide hydrogel substrates modestly affects TEER

An important hallmark of BBB function is high TEER, which prohibits paracellular transport. We measured TEER of BMECs cultured on PA gels cast in Transwell filters. Based on titration experiments, we determined that the maximum stiffness we could achieve in PA gels crosslinked with N-6 linker was 55 kPa, so this value was chosen as the upper limit (Figure ___). We also prepared PA gels at 3 kPa and 20 kPa stiffness to mimic the elastic modulus of bulk brain tissue and peripheral vessel intimal stiffness. We found that BMECs cultured on 3 kPa gels could not form a passive barrier, as determined by negligible TEER. In contrast, BMECs cultured on either 20 kPa or 55 kPa gels exhibited similar maximum TEER, but the cells on 20 kPa gels maintained maximum TEER values longer, indicating that 20 kPa may be optimal for passive barrier formation (Figure 3.4). Based on these results, we directed our more in-depth investigations towards passive barrier function.

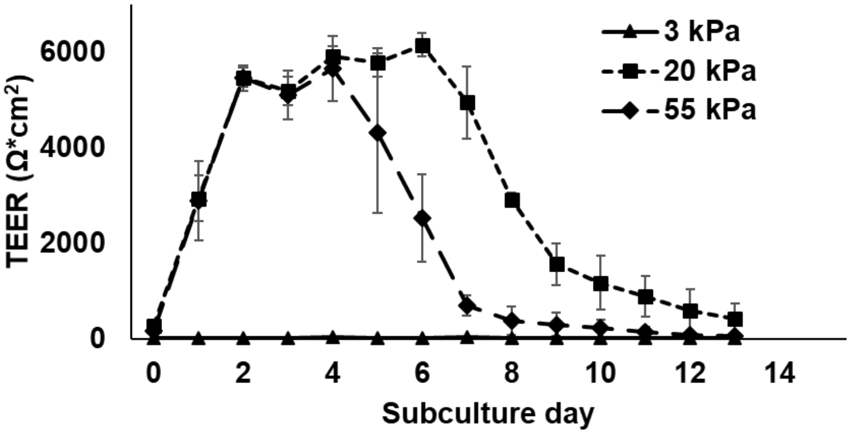

Figure 3.4 TEER of BMEC-like cells as a function of substrate stiffness. TEER was performed on PA gel substrates. 3 filters were prepared for each condition, and each filter was measured in triplicate. Values for each day represent mean ± standard deviation from these 9 measurements.

3.4.4 Phenotypic and functional assessments of iPSC-derived BMEC-like cells cultured on PA hydrogels

Peripheral endothelial cell mechanobiology studies have shown that actin reorganizes in response to substrate stiffness and that this reorganization can disrupt endothelial barriers[83]. Quiescent endothelium is characterized by a cortical actin ring to reinforce cell-cell junctions, while intracellular actin stress fibers are associated with barrier dysfunction and increased permeability[84]. With this in mind, we assessed if actin organization in BMEC-like cells was affected by substrate stiffnesses of 1, 20, and 150 kPa, mimicking the conditions mentioned in the previous paragraph. After 8 and 15 days of culture on hydrogels, phalloidin staining revealed that BMEC-like cells cultured on 1 and 150 kPa substrates developed significantly higher numbers of intracellular actin stress fibers relative to cells cultured on 20 kPa substrates (Figure 3A-C). When comparing BMEC-like cells on 1 and 150 kPa substrates, the number of total stress fibers is not statistically different, but actin filaments on the stiffer matrix appear thicker and more pronounced than the diffuse filaments on the soft matrix (Figure 3A-B). Since complex tight junction structure is an important hallmark of the BBB, and loss of tight junction integrity and passive barrier function are typically associated with increased tight junction width and tortuosity in peripheral endothelium[48,85,86], we quantified width and tortuosity of occludin, a major constituent of BBB tight junctions. At 3, 8, and 15 days of culture on PA hydrogel substrates, no statistical differences were observed in occludin width or tortuosity (Figure 3D-E). Next, since molecular transporters are another key aspect of BBB function, we quantified p-glycoprotein activity using fluorescent rhodamine 123 (substrate) and cyclosporin A (inhibitor) after 8 days of culture on PA hydrogel substrates, where the inhibitor yields an increase in substrate accumulation if the transporter is active. Here, we did not observe any significant difference in p-glycoprotein activity across the different substrate stiffnesses as measured by rhodamine 123 signal (Figure 3F). These results suggest passive barrier function may be compromised on softer and stiffer substrates, as judged by the formation of actin stress fibers, without overt changes to tight junction organization. In contrast, p-glycoprotein activity is unaffected by substrate stiffness.

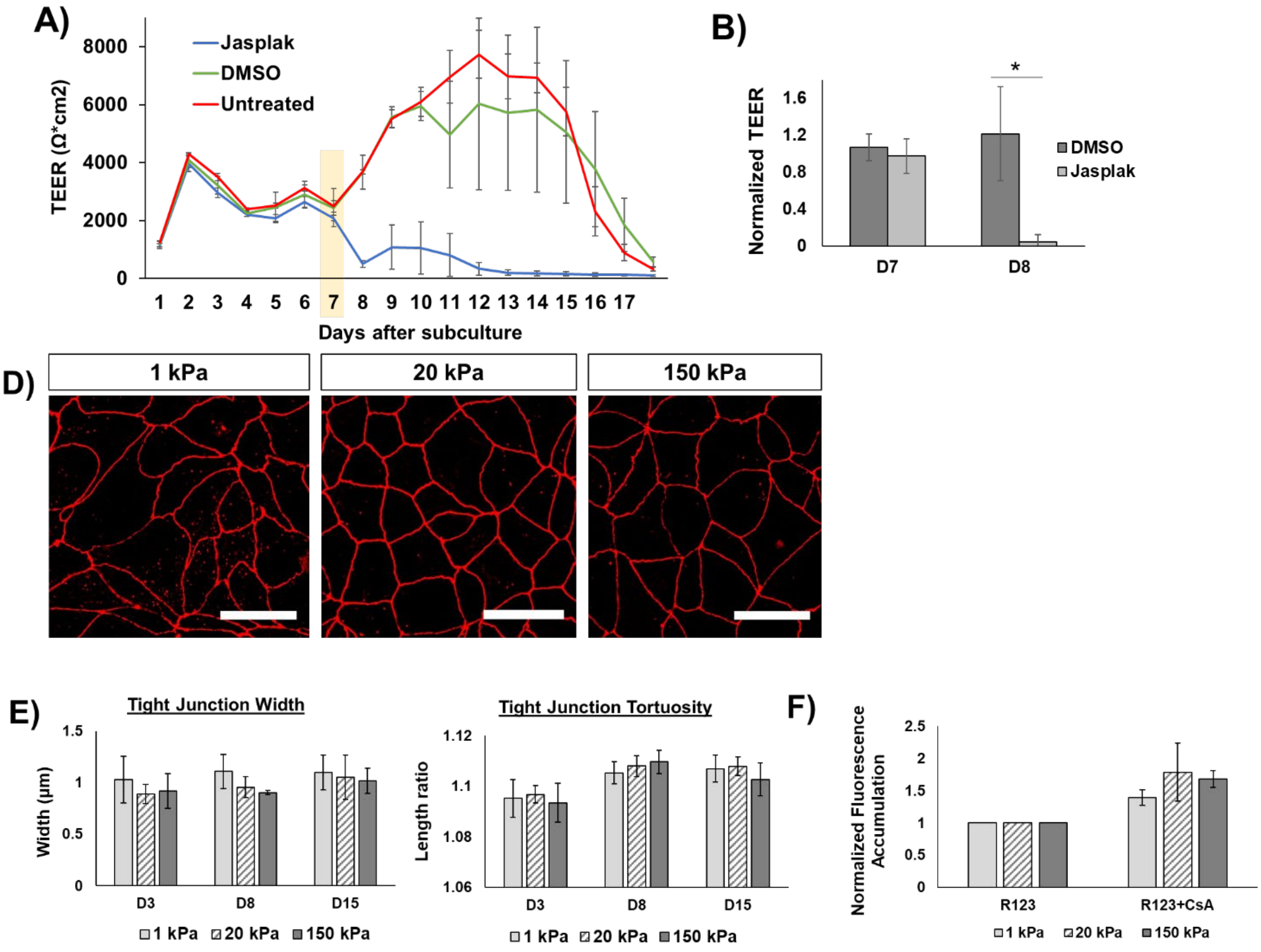

Figure 3.5 Phenotypic and functional characteristics of iPSC-derived BMEC-like cells on PA hydrogels. (A, B) Representative images of phalloidin-stained BMEC-like cells after 8 days (panel A) and 15 days (panel B) on hydrogels. Scale bars represent 30 µm. (C) Quantification of actin stress fibers on each substrate. Three distinct images were collected for each hydrogel and the total number of actin stress fibers were counted manually for each image. This process was repeated for triplicate hydrogels across 3 different iPSC differentiations (biological N=9). Data are reported as number of fibers per field of view averaged across all biological replicates. A one-way ANOVA with a Tukey post hoc test was used to evaluate the difference in actin fibers per field of view between stiffness conditions (*$*p<0.05$, $**p<0.01$*). (D) Representative images of occludin-stained BMEC-like cells after 8 days on hydrogels. Scale bars are 30100 µm. (E) Quantification of tight junction width and tortuosity on each hydrogel substrate at varying time points. Three distinct images were collected for each hydrogel and tight junction width and tortuosity were analyzed using a MATLAB script. This process was repeated for triplicate hydrogels across 3 different iPSC differentiations (biological N=9). No significant differences were observed across stiffness conditions. (F) Flow cytometry quantification of rhodamine 123 (R123) uptake in BMEC-like cells after 8 days on hydrogels. Fluorescence was averaged across biological triplicates and normalized to R123 alone for each condition. Data are presented as mean ± standard deviation. No significant differences were observed in fluorescence increase upon inhibitor treatment across stiffness conditions.

3.4.5 Actin disruption explicitly compromises passive barrier integrity in iPSC-derived BMEC-like cells

After observing stiffness-induced actin disruption, we assessed passive barrier function in iPSC-derived BMEC-like cells in response to a chemical modulator of actin, jasplakinolide (jasplak). Jasplak is a peptide that binds directly to actin and induces polymerization[87] and has been shown to disrupt actin organization in endothelial monolayers[88]. Treatment of multiple endothelial cell subtypes with jasplak has been shown to diminish cortical actin signal and induce the formation of abnormal actin bundles[89]. In iPSC-derived BMEC-like cells cultured on Transwell filters without hydrogel substrates, treatment with jasplak induced a statistically significant decline in TEER in comparison to DMSO-treated and untreated controls (Figure 4A). This effect was consistent across multiple biological replicates (Figure 4B) and suggests that actin disruption can rapidly diminish passive barrier function in iPSC-derived BMEC-like cells, aligning with the actin imaging data.

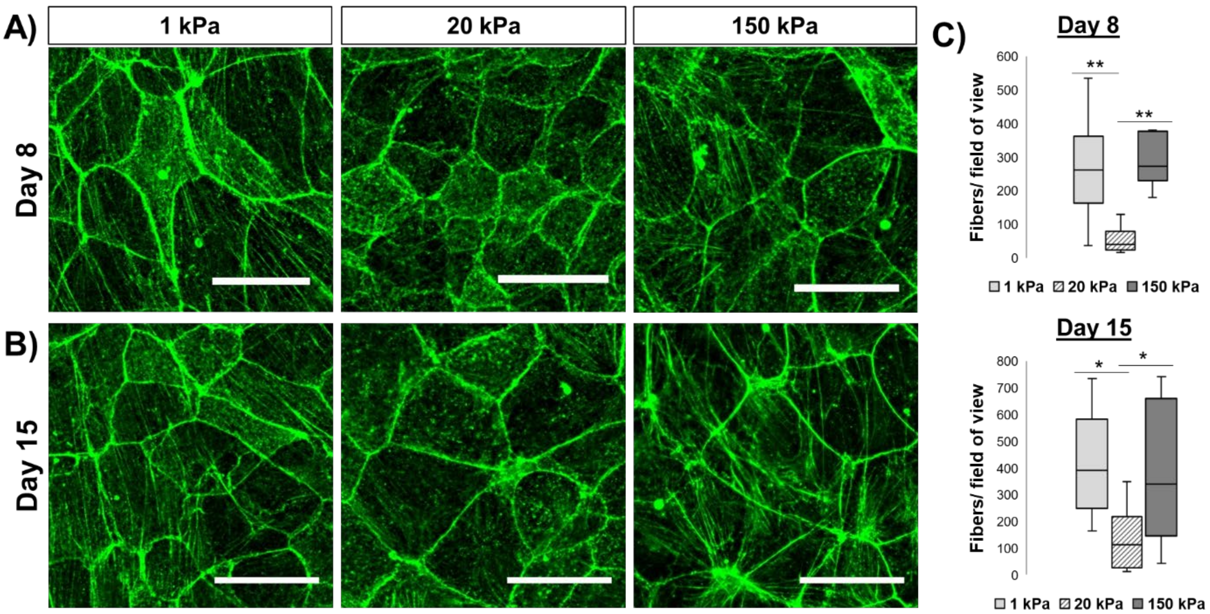

Figure 3.6 Actin disruption compromises passive barrier function in iPSC-derived BMEC-like cells independent of hydrogel substrates. (A) Representative TEER profiles in untreated cells and cells treated with jasplakinolide (jasplak) or DMSO. 3 filters were prepared for each condition, and each filter was measured in triplicate. Values for each day represent mean ± standard deviation from these 9 measurements. The yellow highlight indicates the day of treatment. (B) Average TEER before and 24 hours after jasplak or DMSO treatment. TEER values were normalized to untreated controls from the same day and averaged across 3 biological replicates. Data are presented as mean ± standard deviation. A student's unpaired t-test was used to assess statistical significance (*$*p<0.05$*).

3.4.6 Substrate stiffness modestly influences transcriptome and phosphorylation of common kinases

To examine global responses to substrate stiffness, we first collected RNA from iPSC-derived BMEC-like cells cultured on 1, 20, and 150 kPa substrates for 8 days. Bulk RNA-sequencing revealed a cohort of differentially expressed genes, and we used gene ontology analyses to infer differences in signaling pathway activation (Figure 5). When comparing 1 kPa to 20 kPa, 627 genes were significantly downregulated and 685 genes were significantly upregulated on the softer substrate. When comparing 20 kPa and 150 kPa, 207 genes were significantly downregulated and 218 genes were significantly upregulated on the softer substrate. When comparing 1 kPa and 150 kPa, 448 genes were significantly downregulated and 578 genes were significantly upregulated on the softer substrate. Several interesting differences were noted. In particular, cell cycle pathways are downregulated in iPSC-derived BMEC-like cells cultured on 20 kPa substrates versus 1 and 150 kPa substrates, which could reflect a more quiescent state within cells lacking actin stress fibers on a substrate stiffness mimicking healthy vessel intima. As another example, Rho GTPase signaling was upregulated on the 1 kPa substrates, and this pathway is associated with mechanotransduction and putative stress fiber formation[90]. The full list of differentially expressed genes can be found in Table SI 1.

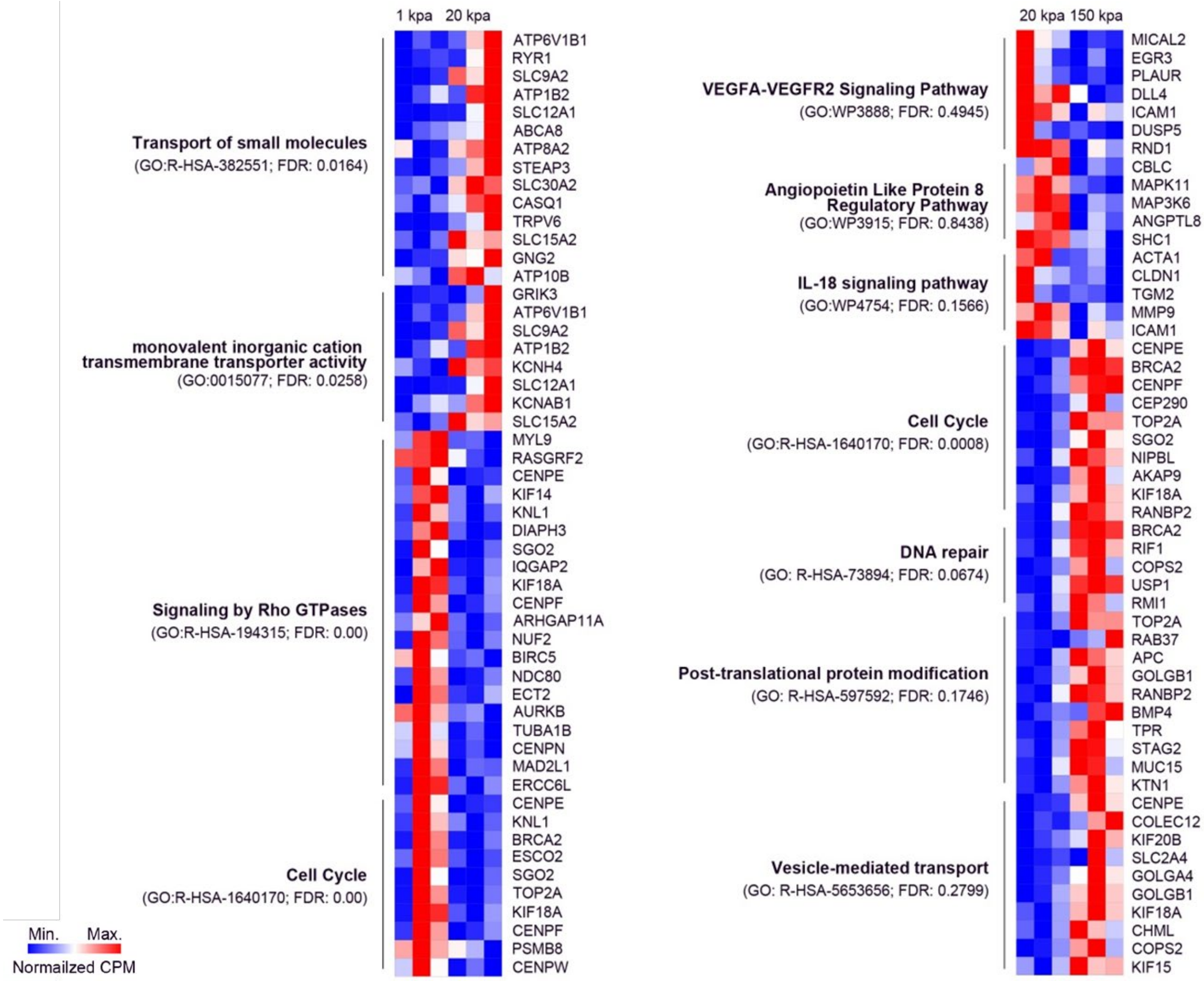

Figure 3.7 Characterization of iPSC-derived BMEC-like cell transcriptome in response to substrate stiffness. RNA was isolated and sequenced from BMEC-like cells cultured on 1, 20, and 150 kPa substrates for 87 days. Pathway enrichment analysis was performed on significantly altered genes ($p<0.05$). Comparisons of 1 versus 20 kPa (left) and 20 versus 150 kPa (right) are displayed with false-discovery rates.

Since increased substrate stiffness is generally associated with endothelial dysfunction, we examined differences in global protein phosphorylation between iPSC-derived BMEC-like cells cultured on 20 versus 150 kPa substrates. Protein was isolated from cells cultured on each substrate for 7 days and measured for relative phosphorylation levels of 43 targets using an array kit. Although differences were modest, several proteins that have putative roles in cytoskeletal regulation, such as ERK1/2 and WNK1, had altered phosphorylation status as a function of substrate stiffness. Mechanical stress has been shown to induce ERK phosphorylation, which was higher on the 150 kPa substrates, thus generally agreeing with this trend. WNK1 plays known roles in morphogenesis, proliferation, and migration of endothelial cells[91], and WNK1 phosphorylation is important for its activation status[92]; as such, decreased WNK1 phosphorylation on 150 kPa substrates could be reflective of loss of key endothelial functions. Overall, these datasets provide a rich foundation for assessing how increased substrate stiffness may influence BBB dysfunction in BMECs.

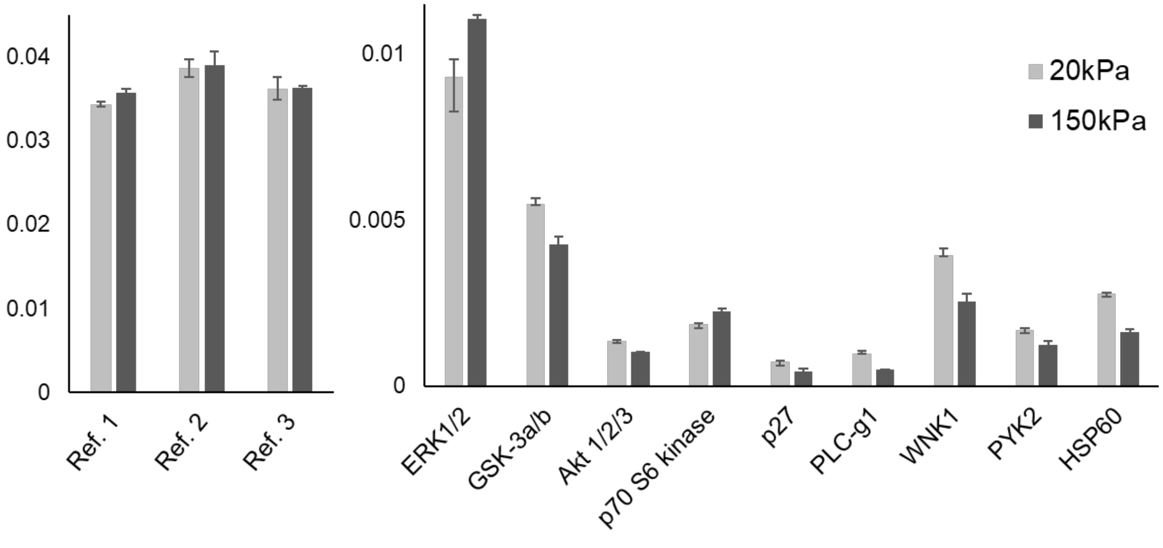

Figure 3.8 Phospho-kinase array shows differences between 20 and 150 kPa conditions. Significant differences in baseline phosphorylation between subculture day 7 BMECs on 20 versus 150kPa substrates were quantified using a phospho-kinase array kit. While reference spots show no statistical difference, nine common phosphorylation sites show different phosphorylation levels.

3.5 Conclusions

We determined that iPSC-derived BMEC-like cells can be seeded on hydrogels for interrogation of biophysical responses to substrate stiffness. Our results demonstrate that, in agreement with general mechanobiology trends, iPSC-derived BMEC-like cells exhibit optimum passive barrier function on intermediate substrate stiffness and develop intracellular actin stress fibers on relatively soft and stiff matrices. We further demonstrate that passive barrier function is rapidly disrupted by small molecule-induced actin polymerization. Thus, similar to studies on peripheral endothelial cells[49], endothelial cells with a highly impermeable barrier exhibit optimum function on an intermediate substrate stiffness that supports cytoskeletal health. These findings may be relevant for designing improved *in vitro* neurovascular models where BBB function must be properly represented.

Curiously, we did not observe any significant differences in tight junction morphology as a function of substrate stiffness. We have previously shown that TEER levels in iPSC-derived BMEC-like cells do not correlate with tight junction expression levels[93], which suggests that the formation of actin stress fibers could be negatively influencing barrier function without impacting overt tight junction structures. More sensitive imaging techniques such as electron microscopy might be necessary to resolve ultrastructural differences that cannot be seen by fluorescence. We also did not observe any differences in p-glycoprotein efflux activity as a function of substrate stiffness. These results would suggest that active barrier functions are not significantly influenced by stiffness-induced cytoskeleton remodeling, but more work would be needed to probe this possibility across a more diverse array of transporters and substrates.

Overall, our results support prior investigations showing that iPSC-derived BMEC-like cells respond to mechanical cues in a manner similar to cultured endothelial cells. Our results also provide evidence that increased substrate stiffness, a ubiquitous feature of aging and disease in the periphery, may mediate negative changes in the BBB. BBB dysfunction has been linked to many disease states including stroke, neurodegenerative disease, traumatic brain injury, brain tumors, and natural aging[27,28]. In Alzheimer's Disease (AD), BBB dysfunction is accompanied by thickening of the vascular basement membrane up to four times its original size,[35] with increased collagen content that may alter vessel stiffness[36]. Additionally, ~90% of AD cases co-occur with cerebral amyloid angiopathy, where amyloid-β aggregates can deposit directly onto the medial layer of arteries and arterioles, disrupting vessel architecture and forming a 'rigid cast' around the vessel that potentially alter the mechanical properties of the vessel[94]. Hence, future work may focus on assessing whether our observations in the *in vitro* system map to human tissue samples from these patient populations.

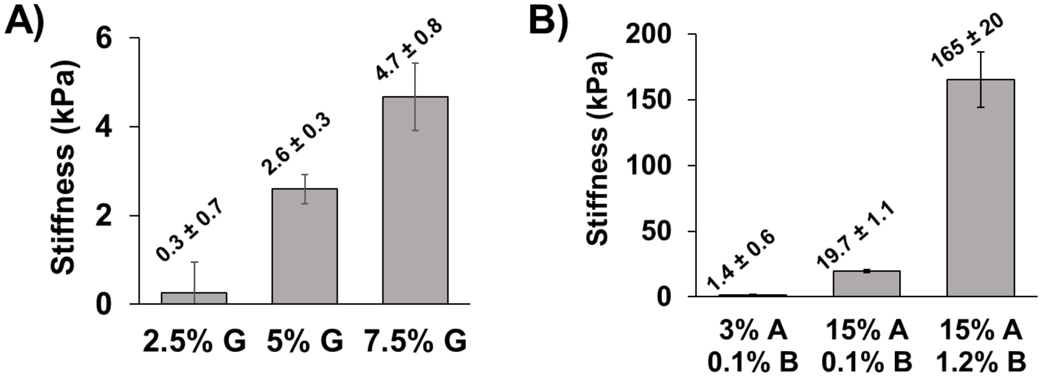

Figure A.3.1 Characterization of hydrogel stiffness. Young's Modulus of gelatin (A) and polyacrylamide (B) hydrogels quantified using atomic force microscopy. Values represent mean ± standard deviation across technical triplicates.

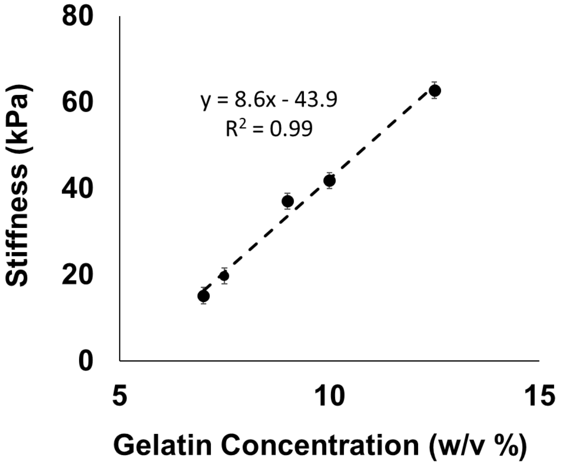

Figure A.3.2 Bulk characterization of hydrogel stiffness. Young's Modulus of gelatin was quantified by measuring bulk gel constructs on and Instron. In comparison to AFM data from Figure A.3.1, these data indicate that method of stiffness quantification can yield different values.

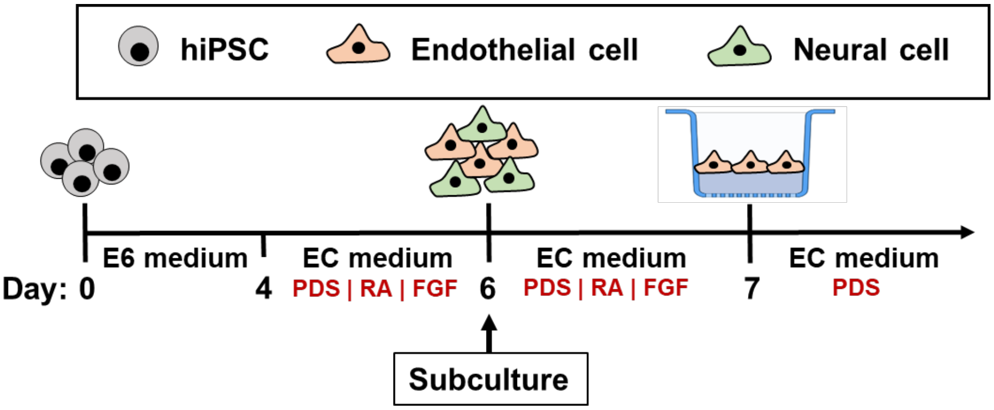

Figure A.3.3 Differentiation strategy for measuring TEER of BMEC-like cells on gelatin substrates. A previous iteration of the differentiation protocol was used for these experiments. From day 4 to day 7, PDS was used in endothelial cell media.

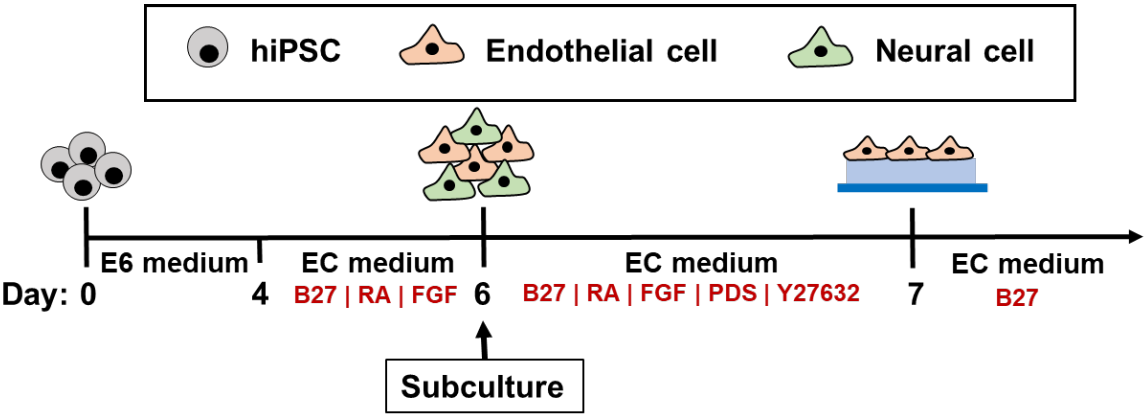

Figure A.3.4 Optimized differentiation strategy for generating BMEC-like cell monolayer on PA substrates. An updated version of the differentiation protocol was used for these experiments. From day 4 to day 7, B27 supplement was used in endothelial cell media. On the day of subculture, media was supplemented with PDS and Y27632 to promote cell attachment.

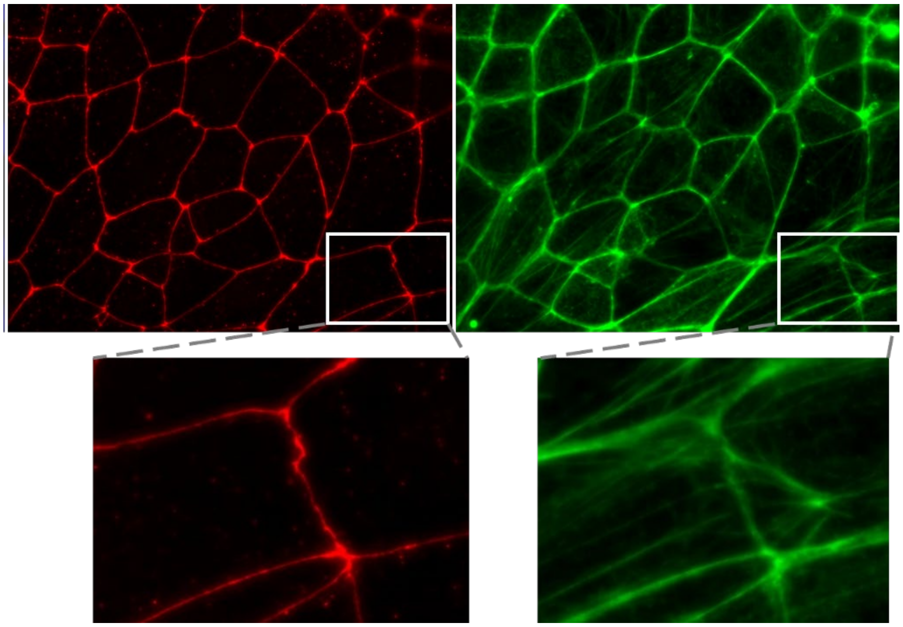

Figure A.3.5 Site of tight junction tortuosity corresponds to intracellular actin stress fiber formation. Occludin (red) in BMEC-like cells adhered to PA hydrogel substrates presents as a discontinuous junction at the site of intracellular actin (green) stress fibers.

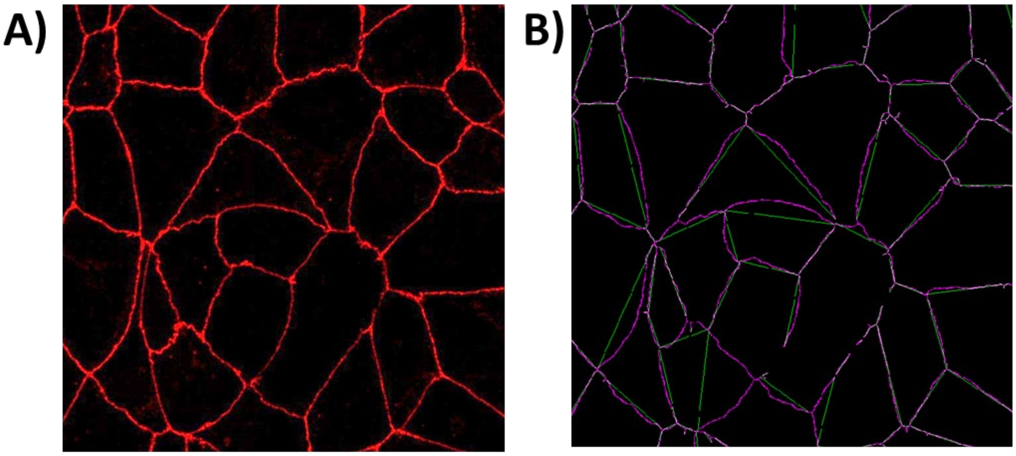

$$\boldsymbol{Tortuosity = \frac{actual\ path}{direct\ path}}$$

Figure A.3.6 Quantification of tight junction tortuosity in MATLAB. (A) BMEC-like cells were stained for occluding (red) and imaged on a confocal microscope. (B) Skeletonized image generated in MATLAB depicts the most direct path (green) between junction foci and the actual path (purple). Tortuosity was calculated by dividing the actual path by direct path.

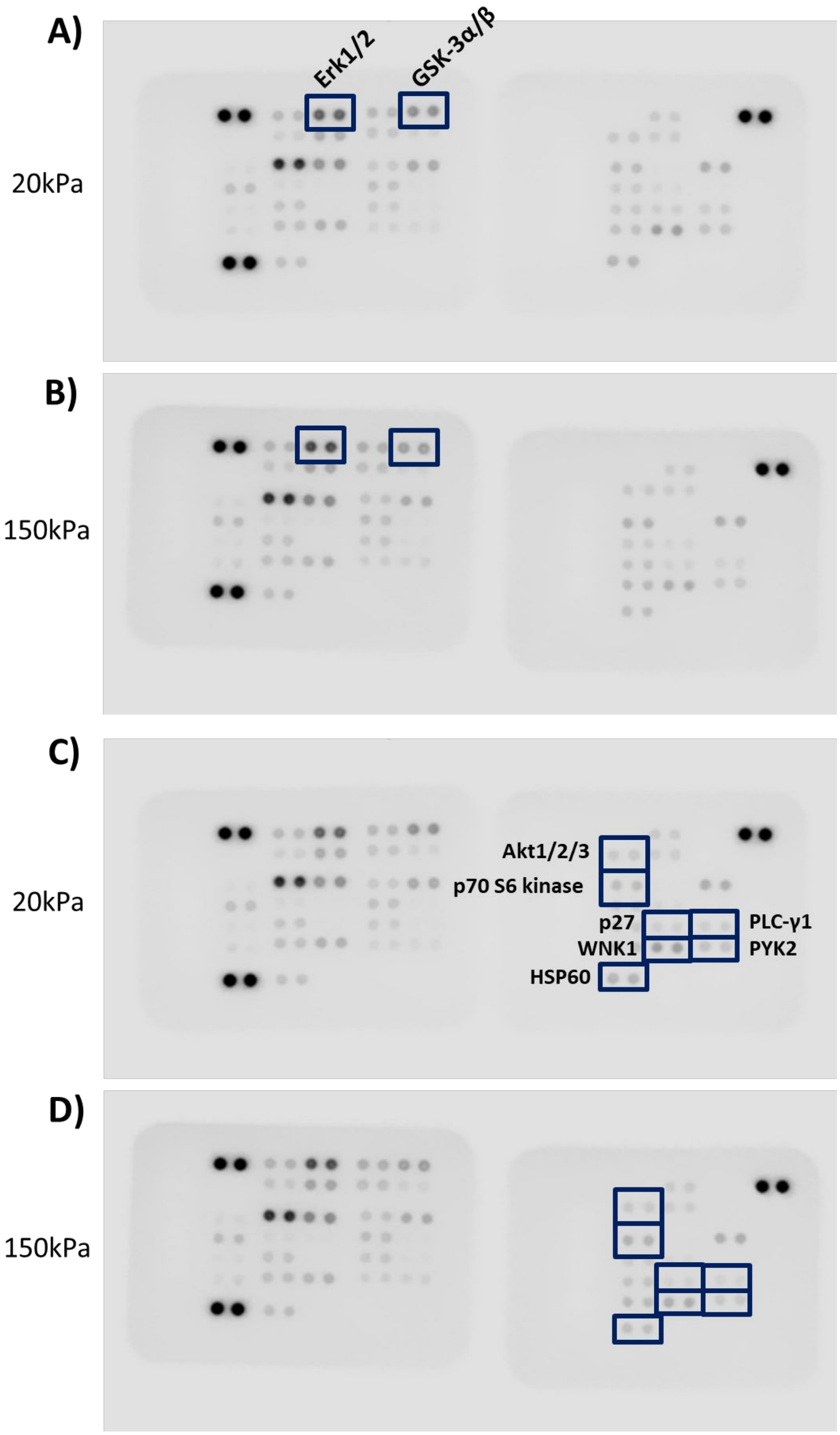
A)
Erk1/2
GSK-3α/β
20kPa
B)
150kPa
C)
20kPa
Akt1/2/3
p70 S6 kinase
p27
WNK1
HSP60
PLC-γ1
PYK2
D)
150kPa

Figure A.3.7 Characterization of hydrogel stiffness. Array was performed to determine the activation level of common phosphorylation sites. Briefy, membranes dotted with capture antibodies were incubated with protein isolated from BMEC-like cells on 20 kPa (A, C) and 150 kPa (B, D) substrates. Chemiluminecence was captured and pixel intensity of each spot was quantified. Panels A and B represent membrane A, and panelss C and D represent membrane B in the R&D systems kit. Duplicate dots that are boxed represent signals that exhibited significant differences between the 20 kPa and 150 kPa conditions.

Table A.3.1 Activation of all phosphorylation sites tested in phospho-kinase array kit. Chemiluminescence was captured from membrane dots depicted in Figure A.3.7, then duplicate dot signals were averaged. Average and stadard deviation are showen here for each kinase and phosphorylation site. (Some kinases may be listed multiple times if multiple phosphorylation sites exist.) A t-test was performed to determine statistically significant differences between the 20 and 150 kPa values. Highlighted rows represent signals that exhibited significant differences of $p \leq 0.05$. Separate tables represent membrane A and membrane B.

			Phosphorylation Site	Averages			Standard Deviation	
				20kPa	150kPa		20kPa	150kPa
Ref. 1				0.034335	0.03564		2.83E-04	5.66E-04
Ref. 2				0.038585	0.03904		1.06E-03	1.56E-03
Ref. 3				0.036185	0.03634		1.34E-03	1.41E-04
A	**A3, A4**	**p38a**	T180/Y182	0.002085	0.00238		5.66E-05	1.41E-04
	A5,A6	**ERK1/2**	T202/Y204, T185/ Y187	0.009315	0.01104		5.23E-04	1.41E-04
	A7,A8	**JNK1/2/3**	T183/Y185, T221/ Y223	0.002085	0.00277		2.12E-04	1.27E-04
	A9,A10	**GSK-3a/b**	S21/S9	0.00549	0.00426		1.77E-04	2.26E-04
	B3,B4	**EGFR**	Y1086	0.000538	0.000887		6.29E-05	4.14E-04
	B5,B6	**MSK1/2**	S376/S360	0.003	0.003445		2.19E-04	2.76E-04
	B7,B8	**AMPKa1**	T183	0.00119	0.00159		1.48E-04	1.98E-04
	B9,B10	**Akt1/2/3**	S473	0.000599	0.00053		2.71E-04	2.30E-04
	C1,C2	**TOR**	S2448	0.000308	0.000307		9.48E-05	2.49E-04
	C3,C4	**CREB**	S133	0.013635	0.01384		2.83E-04	4.24E-04
	C5,C6	**HSP27**	S78/S82	0.005705	0.00628		1.13E-04	4.10E-04
	C7,C8	**AMPKa2**	T172	0.001001	0.001245		6.36E-06	1.34E-04
	C9,C10	**b-catenin**	----	0.003365	0.002785		1.41E-04	1.63E-04
	D1,D2	**Src**	Y419	0.001725	0.00163		0.00E+00	7.07E-05
	D3,D4	**Lyn**	Y397	0.00028	0.000241		2.55E-05	2.01E-04
	D5,D6	**Lck**	Y394	0.00015	0.000118		1.10E-04	1.94E-04
	D7,D8	**STAT2**	Y689	0.001415	0.00151		0.00E+00	9.90E-05
	D9,D10	**STAT5a**	Y694	8.07E-05	8.41E-05		9.60E-05	7.43E-05
	E1,E2	**Fyn**	Y420	0.000268	0.000172		2.90E-05	7.54E-05
	E3,E4	**Yes**	Y426	0.001215	0.00121		4.24E-05	2.83E-05
	E5,E6	**Fgr**	Y412	-2.5E-05	-5.8E-05		5.07E-05	5.05E-05
	E7,E8	**STAT6**	Y641	0.000924	0.001041		1.15E-04	1.54E-04
	E9,E10	**STAT5b**	Y699	0.000106	8.83E-05		2.01E-05	9.90E-06
	F1,F2	**Hck**	Y411	0.000403	0.000427		2.00E-04	1.98E-04
	F3,F4	**Chk-2**	T68	0.00171	0.00158		3.04E-04	2.83E-05
	F5,F6	**FAK**	Y397	0.00278	0.00236		7.07E-06	3.39E-04
	F7,F8	**PDGFRb**	Y751	0.000521	0.000628		7.42E-05	1.12E-04
	F9,F10	**STAT5a/b**	Y694/Y699	0.00048	0.000605		1.04E-04	1.45E-04
	G3,G4	**PRAS40**	T246	0.00172	0.001725		4.95E-05	2.12E-05

			Phosphorylation Site	Averages			Standard Deviation	
				20kPa	150kPa		20kPa	150kPa
Ref. 1				0.034335	0.03564		2.83E-04	5.66E-04
Ref. 2				0.038585	0.03904		1.06E-03	1.56E-03
Ref. 3				0.036185	0.03634		1.34E-03	1.41E-04
B	**A13,A14**	**p53**	S392	0.00116	0.000848		9.19E-05	1.52E-04
	B11,B12	**Akt 1/2/3**	T308	0.00135	0.001042		3.54E-05	0.00E+00
	B13,B14	**p53**	S46	0.00097	0.00081		2.06E-04	1.12E-04
	C11,C12	**p70 S6 kinase**	T389	0.001845	0.002257		4.24E-05	6.36E-05
	C13,C14	**p53**	S15	8.93E-05	7.57E-05		1.57E-05	2.80E-05
	C15,C16	**c-Jun**	S63	0.00297	0.002667		4.95E-05	1.63E-04
	D11,D12	**p70 S6 kinase**	T421/S424	0.000898	0.00077		5.30E-05	1.42E-04
	D13,D14	**RSK 1/2/3**	S380/S386/S377	0.000333	0.000369		1.13E-04	7.50E-05
	D15,D16	**eNOS**	S1177	6.45E-05	4.23E-05		8.84E-06	3.71E-05
	E11,E12	**STAT3**	Y705	0.001008	0.001112		9.19E-06	9.90E-05
	E13,E14	**p27**	T198	0.000737	0.000428		2.19E-05	9.55E-05
	E15,E16	**PLC-g1**	Y783	0.000982	0.000486		6.43E-05	9.90E-06
	F11,F12	**STAT3**	S727	0.00154	0.001662		1.06E-04	9.90E-05
	F13,F14	**WNK1**	T60	0.00394	0.002537		1.91E-04	2.33E-04
	F15,F16	**PYK2**	Y402	0.00167	0.001227		6.36E-05	1.20E-04
	G11,G12	**HSP60**	----	0.00279	0.001617		2.12E-05	9.19E-05

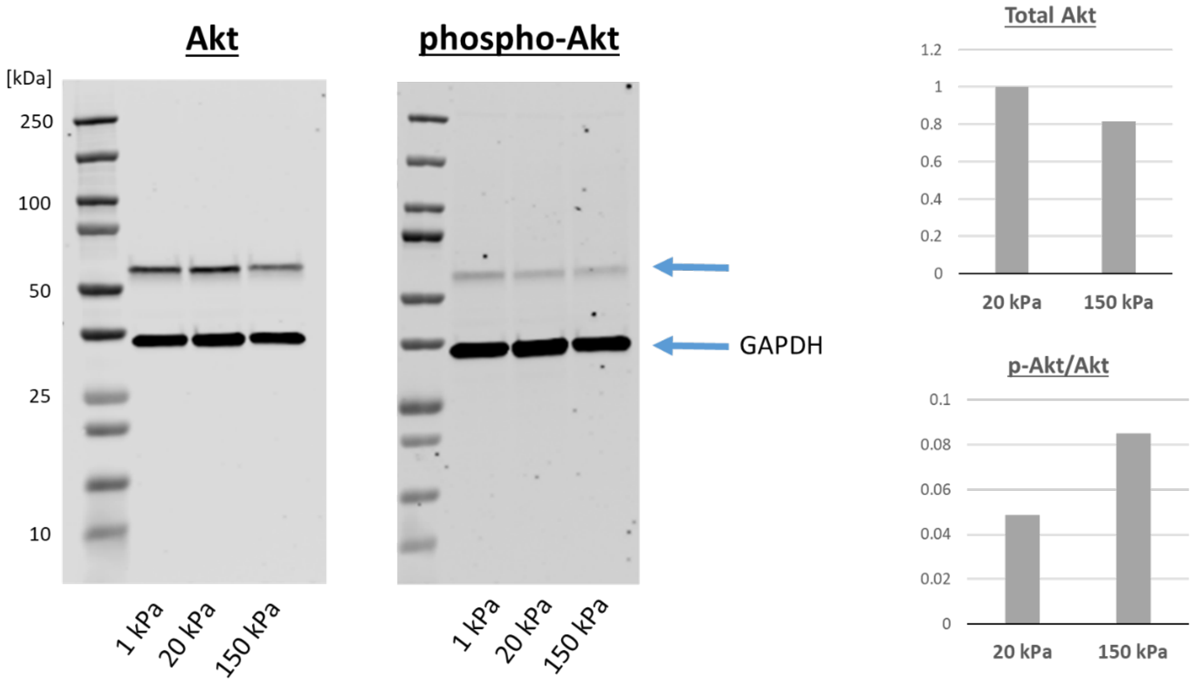

Figure A.3.8 Follow up on target from phospho-kinase array. Akt showed statistically significant differences in levels of phosphorylation between 20 and 150 kPa conditions, so western blots were performed using protein isolated from BMEC-like cells on PA gel substrates 8 days after subculture. Total Akt (top right) was quantified my measuring pixel intensity of the Akt bands and normalizing to the corresponding GAPDH band. p-Akt was quantified in the same way, and p-Akt/Akt (bottom right) represents the fraction of activated Akt in each stiffness condition, indicating that the stiffer substrate enhances Akt activation.

Chapter 4

ALTERNATIVE APPROACHES TO STUDYING CAA IN VITRO

4.1 Summary

Cerebral Amyloid Angiopathy (CAA) has a very high co-occurrence with AD and contributes to cognitive decline. Existing models of CAA are animal models, mainly rodents, but the development of an *in vitro* model that uses human cells may be advantageous to analyzing different factors of disease progression and for better mimicking the human vasculature. We sought to design two *in vitro* systems for studying human CAA using 3-D dynamic hydrogel platforms.

Gelatin was modified to create a light-responsive dynamic stiffening hydrogel called gel-MA and biofuntionalized with a cadherin peptide to support vascular growth. Gel-MA substrates were incorporated into human iPSC-derived BBB models to observe real-time TEER responses to a stiffening substrate. The cadherin gel was used for embedding post-mortem human tissue to recapitulate a 3-D CAA microenvironment.

iPSC-derived BBB endothelial cells formed physiologically relevant TEER values on gel-MA substrates, and exposure to stiffening conditions temporarily caused a decline in TEER but the cells ultimately returned to maximum TEER values. Additionally, human tissue that was embedded in cadherin gels retained intact vasculature and showed some signs of new vessel growth. Tissue treated with amyloid-β was positive for vascular amyloid and myofibroblast markers. These platforms may be valuable in uncovering CAA disease mechanisms, namely barrier modifications in response to a stiffening substrate, and the impact of ECM and soluble cues on CAA progression in human vessels.

4.2 Introduction

Dynamic hydrogel systems have been used to model tissue fibrosis[95] and stem cell differentiation[96]. Typically consisting of methacrylate groups conjugated to hyaluronic acid[95] or gelatin[97], these hydrogels undergo a two-step polymerization reaction in which primary cross-linking is catalyzed by an enzyme, while secondary cross-linking occurs in response to light exposure. This two-step polymerization allows for analysis of cellular responses to a stiffening matrix in real time. As opposed to cells being transferred from a plastic dish to a static hydrogel, cells adhered to these dynamic hydrogels sense the transition from a soft to a stiff matrix while being maintained on the same substrate. This more closely mimics physiological disease conditions. Dynamic gelatin and hyaluronic acid platforms are also amenable to three-dimensional cell culture, which cannot be achieved using synthetic, static hydrogels such as polyacrylamide. In the context of the BBB, three-dimensional co-culture is advantageous for studying the contribution of supporting glial cell types, such as astrocytes and pericytes, on barrier function. A wide variety of stiffness values can be achieved using a methacrylated gelatin (gel-MA) platform[98,99]. Wu, et al. showed that gel-MA stiffness can range from 3kPa to 180kPa be altering gel-MA concentration. Degree of methacrylation can also be tuned within this system to modify stiffness. Thus, the versatility of this system allows us to tailor our experiments to the stiffness transitions that occur in AD.

To our knowledge, no one has applied these dynamic hydrogel systems to study endothelial barrier function on a stiffening substrate, especially at the BBB. Utilization of this widely tunable platform would allow us to study real time changes in barrier function in response to a stiffening substrate. This dynamic hydrogel platform can reveal changes in BBB passive barrier as a function of stiffness.

Another application of hydrogels for in vitro modeling is three-dimensional embedding. Since two-dimensional culture dishes do not fully recapitulate the tissue microenvironment, hydrogels have been engineered to contain proteins that mimic native ECM to support cell or tissue growth. This can be achieved by decellularizing existing tissue or my functionalizing natural hydrogel polymers. Previous work from our lab, for example, has shown that functionalization of gelatin with N-cadherin peptide, a cell adhesion molecule that plays an important role in neurite growth during neurogenesis, enhances neuronal maturity and synaptogenesis in vitro[46]. Scrambled peptide control hydrogels caused neurons to die within 4 days while neurons in N-cadherin-conjugated gels exhibited 97% cell viability after 10 days of embedding. Not only does this system highlight the importance of biochemical signaling, but it also better recapitulates the three-dimensional environment of the brain.

Three-dimensional in vitro models have also been used to study vasculature. These models can either be derived from isolated cells or whole tissue structures. One such ex vivo tissue model has been used to study metastasis, for example. Mouse cancer cells were isolated, dissociated into single cells, grown into spheroids, then embedded into hydrogels to assay ex vivo growth and therapeutic response[100]. Others have excised entire vessel structures and placed them into bioreactors to examine device degradation. Porcine aortas were isolated and placed into bioreactors to examine magnesium stent degradation under laminar flow[101]. Another study placed human umbilical cord arteries into bioreactors to examine the effect of shear stress on vascular smooth muscle cell growth[102]. These bioreactor systems are valuable in bridging the gap between device design and implantation into an in vivo system, and they help with predicting in vivo outcomes. While these models were valuable in their respective studies, neither allowed for examination of intact arterioles, or small vessels. To our knowledge, no in vitro model systems exist to study human CAA using intact tissue.

Recent work from our group involved the development of a model system in which post-mortem human tissue can be embedded into a biofunctionalized hydrogel that maintains structural integrity of small vessels. Arterioles within the system exhibit in vivo-like organization with endothelial cells surrounded by α-SMA-positive vascular smooth muscle cells and TE-7-positive fibroblasts in the perivascular space. This system is advantageous for studying CAA because arterioles are typically the site of microhemorrhages that lead to gradual cognitive decline. We aimed to use this model system to induce a CAA phenotype and allow for mechanistic studies that are typically not possible with post-mortem tissue.

4.3 Materials and Methods

4.3.1 Gel-MA Synthesis and Characterization

To synthesize gel-MA, a 10% (w/v) gelatin solution was prepared by mixing on a hot plate at 60°C for at least 2 hours. Then 6mL of methacrylic anhydride (Sigma 276685) was added to 100mL of 10% gelatin solution while stirring and left to react for up to 3 hours (50°C, 270 rpm). After 3 hours, solution was centrifuged at 3500xg for 3 min to remove excess methacrylic anhydride. The gel-MA supernatant was decanted from the methacrylic anhydride pellet and transferred to a beaker containing 200 mL pre-warmed ultrapure water (Fisher 10977023) and stirred at 40°C until well mixed.

Dialysis was performed to further remove unbound methacrylic anhydride. 12 kDa dialysis tubing (Fisher 21-152-14) was soaked in diH2O and clipped shut on one end with a weighted clip (Fisher 08-750-24P). Diluted gel-MA solution was then pipetted into dialysis tubing and clipped tightly on the opposite end. Sealed dialysis bags were submerged in diH2O, covered with foil to prevent light degradation, and left to mix at 40°C for 10 days. Fresh water was added 2-3 times each day.

After ten days, dialyzed gel-MA was pH adjusted to 7.4 using 1M sodium bicarbonate. Gel-MA was then frozen and lyophilized for 5 days, still covered in foil to protect from light degradation. Gel-MA powder was placed in -80°C freezer for long-term storage.

To characterize gel-MA and quantify the degree of methacrylation, ^{1}H-NMR was performed using a Bruker 500 Hz NMR spectrometer set to 37 °C. Lyophilized gel-MA and gelatin were reconstituted in deuterated water at 10 mg/mL. Resulting spectra was analyzed to determine degree of methacrylation by measuring the area under peaks. Peak at 7.1-7.4 ppm is from phenylalanine on gelatin backbone, and this peak should be consistent across all samples. Peaks at 5.3 and 5.5 ppm refer to the acrylic protons of methacrylated grafts, and peak intensity increases with degree of methacrylation. Peak at 2.8-3.0 ppm corresponds to lysine methylene proton on gelatin that is removed during methacrylation, so this peak intensity should decrease with methacrylation. Finally, the peak at 1.8 ppm is the methyl group of metharylated grafts, and peak intensity is increased with methacrylation. In TopSpin software, baseline correction was performed then the area under the phenylalanine peak was set to 1.0. Peaks at 3.0 ppm were then integrated on gelatin and gel-MA spectra. The following equation was used to calculate the degree of methacrylation:

$$DM = \left(1 - \frac{A(lysine\ peak\ on\ gel - MA)}{A(lysine\ peak\ on\ gelatin)}\right)$$

4.3.2 Dynamic Stiffening Gel-MA

Primary cross-linking step was performed to polymerize gel-MA gels in transwell inserts via enzymatic cross-linking. To do this, lyophilized gel-MA was reconstituted in sterile water at 10% (w/v) and sterile-filtered. 1 g of microbial transglutaminase (mTG) (Modernist Pantry 1203-50) was reconstituted in 5 mL of sterile water, then sterile filtered. 4.5 mL of gel-MA solution was then combined with 500 mL of mTG solution then thoroughly mixed by pipetting. 350 uL of the resulting mixture was pipetting into 12-well transwell inserts and left overnight at 37°C in cell culture incubator to polymerize. Gelatin control gels were prepared similarly except a 10% gelatin solution was prepared instead of 10% gel-MA.

On the following day, hydrogels on transwells were incubated with ECM solution in preparation for cell seeding. To prepare the ECM solution, collagen type IV (Sigma C5533) and fibronectin (Sigma 1141) were diluted in sterile water to final concentrations of 0.4 and 0.1 mg/ml, respectively. Hydrogels were incubated with ECM solutions overnight at 37°C in cell culture incubator.

BMEC-like cells were differentiated from iPSCs similar to section 3.3.5. On day 4 of differentiation, updated EC medium was used: Neurobasal (Thermo Fisher 21103049) with 0.25% GlutaMAX (Thermo Fisher 35050061), 0.5% B27 supplement (Thermo Fisher 17504044), 10 µM RA, and 20 ng/mL bFGF. On day 6, cells were plated in the aforementioned EC medium containing 0.1% PDS and 1 µM Y27632 (Tocris 1254) to facilitate adhesion. Cells from 1 well of a 6-well plate were split across 3 transwell inserts. TEER measurements were performed daily according to methods in section 3.3.6 using EndOhm cup chamber (World Precision Instruments ENDOHM-12g) filled with pre-warmed Neurobasal medium.

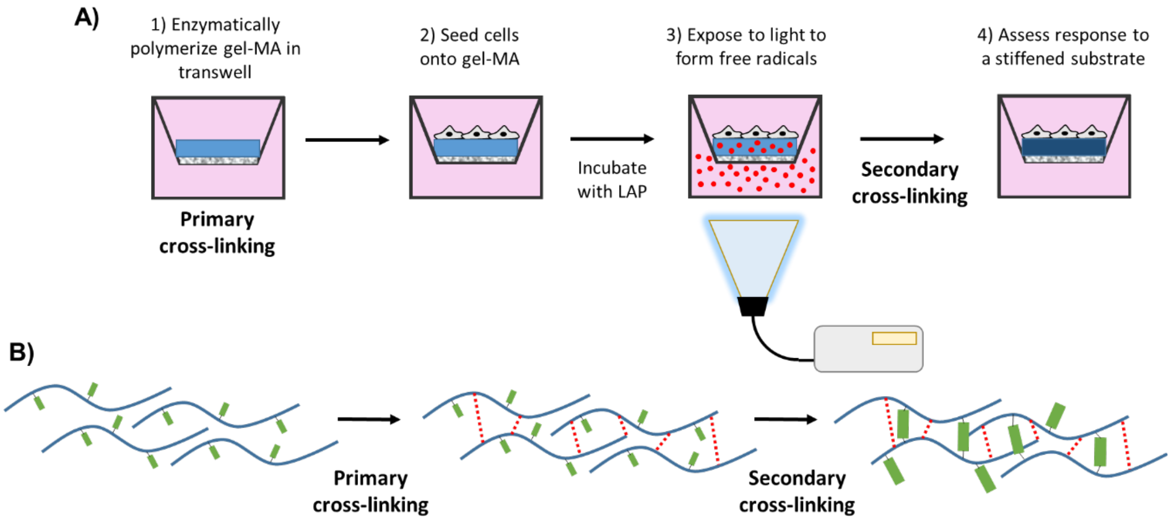

Figure 4.1 Workflow of dynamic stiffening gel-MA hydrogel system. During primary cross-linking step, gel-MA is enzymatically crosslinked via mTG in transwell inserts. (Red dotted lines in panel B represent crosslinks formed by mTG.) Cells are then seeded onto gel-MA substrates, incubated for 1 week, then secondary cross-linking step is performed by incubation with light-responsive free radical initiator, LAP. This process forms crosslinks using grafted methacrylation sites. (In panel B, methacrylation sites are represented by green bars.)

On subculture day 7, secondary cross-linking step was performed. 100 mg of Lithium phenyl-2-4-6-trimethylbenzoylphosphinate (LAP) (Sigma 900889) was reconstituted in 10 mL DMEM, and 1.5 mL was added to the basolateral chamber of each transwell gel. Plate was left to incubate for 2 hours to allow for LAP to diffuse into the gels. Then, each well was exposed to 45 mW of ultraviolet light (UV) (ThorLabs CS2010) for 10 seconds from the bottom of the plate. The plate was left for an additional hour to allow for secondary cross-linking to occur, then TEER was measured and fresh EC medium (Neurobasal with GlutaMax and B27) was added to the basolateral chambers. LAP-initiated cross-linking chemistry is similar to previous methods[95].

4.3.3 Embedding Post-Mortem Human Tissue

Post-mortem human cortical tissue was acquired and cryopreserved for long-term storage prior to embedding in hydrogels. Unfixed tissue was cut into roughly 1 cm cubes and transferred to cryovials containing Hibernate media (Brain Bits HA500) with 10% DMSO. Cryovials were then transferred to a Mr Frosty (Thermo Fisher 15-350-50) and placed in a -80°C freezer for 1 week to fully freeze. Cryovials were then transferred to a liquid nitrogen tank for long-term storage.

Prior to embedding, redox-cad hydrogel materials were prepared. Redox-cad hydrogels are also gelatin-based and can be crosslinked by mTG. Therefore, similar preparation was performed. Lyophilized redox-cad was reconstituted at 10% (w/v) in sterile human endothelial serum-free media (hESFM) (Thermo Fisher 11111044) and sterile filtered. mTG was reconstituted at 1 g/mL water, then sterile filtered. Materials were kept at 37°C during tissue preparation.

Tissue chunks were thawed, broken into smaller pieces, and washed in preparation for embedding. hESFM was added dropwise to the cryovial to prevent osmotic shock-induced cell death. Tissue chunks were transferred to a sterile, dry petri dish using tweezers, then tweezers and a razor blade were used to cut tissue into smaller pieces. Tissue was then transferred to a microfuge tube containing hESFM and triturated 8 times with a P1000. Tubes were centrifuged at 3.5xg for 7 min, then pellets were resuspended in fresh hESFM, and centrifugation was repeated. 300 μL of tissue pellet was then resuspended in 1mL hydrogel solution plus 15 mL mTG solution plus 5 μL PenStrep (Thermo Fisher 15140122). Mixture was mixed by pipetting and 100 μL droplets were added to a glass-bottom 24-well plate (Fisher Scientific NC0397150), and plate was left in 37°C incubator overnight to crosslink. On the following day, 2 mL hESFM was added to each well.

Media was supplemented with PenStrep at 5 µL/mL. Tissue was left to incubate for up to 2 days to promote vessel sprouting.

Immunostaining of embedded tissue was performed to observe CAA phenotype. Fixing and blocking procedures from Methods section 2.3.4 were used, except tissue was blocked overnight at 4°C. Tissue was then incubated overnight with a primary conjugated collagen type I antibody (Novus Biologicals NBP1-77458AF594) diluted in PBSD. Five 10-minute washes were performed on the following day, and tissue was imaged on a Zeiss LSM 710 confocal microscope. Brightfield images were acquired with a Leica DMi8 widefield microscope. For CAA images, embedded tissue was stained with primary antibodies for anti-TE-7 fibroblasts (Millipore CBL271, 1:100) and anti-α-SMA (Millipore ABT1487, 1:1000) overnight at 4°C. Five 10-minute washes were performed on the following day, then tissue was incubated with secondary antibodies donkey anti-mouse Alexa Fluor 555 (Thermo Fisher A31570), donkey anti-rabbit Alexa Fluor 488 (Thermo Fisher A21206), and 2µM Thiazine (Chemsavers THIR1G) for 4 hours at room temperature. Another five 10-minute washes were performed, then tissue was imaged on the Zeis LSM 710 confocal microscope.

4.3.4 Inducing CAA Phenotype with Soluble β-Amyloid

To induce a CAA phenotype, embedded tissue was treated with soluble amyloid-β during 2-day incubation period. Synthetic human amyloid-β (1-40) (AnaSpec AS-24236) was reconstituted in ice-cold Hexafluoroisopropanol (Sigma 105228) at 4 mg/mL and left to dissolve for 1 hour at room temperature. Monomeric amyloid-β solution was then aliquotted into microfuge tubes, and solutions were left in a fume hood overnight to allow for solvent evaporation. On the following day, tubes were sealed with parafilm and transferred to a -80°C freezer for long-term storage. To treat embedded tissue, amyloid-β aliquots were reconstituted in hESFM plus PenStrep mixture at 10 ug/mL and added to well plate on the day after tissue embedding.

4.4 Results and Discussion

4.4.1 Gel-MA Characterization

To validate that methacrylate groups were added to the gelatin backbone, NMR spectra were analyzed. Two gel-MA conditions were tested and compared to an unmodified gelatin control (Figure 4.2). For the two gel-MA conditions, gelatin was left to react with the methacrylic anhydride for 1 hour or 3 hours. Phenylalanine protons are unaffected by methacrylation, so intensity of peaks at 7.4 ppm are identical for all conditions. Peaks at 5.5 ppm are present in only the gel-MA samples because they correspond to acrylic protons on the methacrylated grafts. Since the lysine methylene proton is lost during methacrylation, the peak at 3.0 ppm is highest in gelatin control and decreases with degree of methacrylation. Integration of this peak in gelatin, 1-hour gel-MA, and 3-hour gel-MA are 0.744, 0.3393, and 0.1382, and correspond to degrees of methacrylation of 0%, 54.4%, and 81.4%, respectively. This dataset shows that degree of methacrylation of gelatin can be tuned by modifying the reaction time of gelatin and methacrylic anhydride. Degree of methacrylation will ultimately allow for finer tuning of the secondary cross-linking step, for instance, a higher degree of methacrylation will correspond to a larger increase in stiffness of gel-MA substrates during TEER experiments.

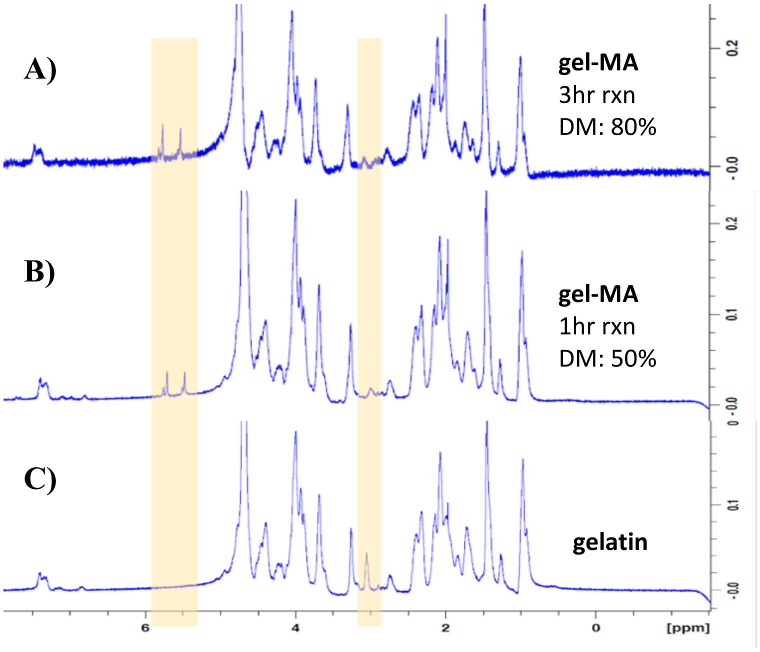

Figure 4.2 NMR analysis of gelatin methacrylation. Samples reconstituted in D2O at 10 mg/mL were measured at 37°C using a 500 Hz NMR spectrometer. Highlighted peaks can be integrated in TopSpin to determine the degree of methacrylation. Left highlighted peaks correspond to methacrylic protons grafted onto gelatin backbone during the reaction while right highlighted peak corresponds to a lysine proton that is lost during the reaction. A 1-hour reaction time yielded a degree of methacrylation of 50% while a 3-hour reaction time yielded a degree of methacrylation of 80%.

4.4.2 TEER on Dynamic Stiffening Gel-MA

To measure barrier properties of iPSC-derived BMEC-like cells on a stiffening substrate, TEER was measured. Prior to secondary cross-linking, TEER gradually increased over 6 days, and cells achieved maximum TEER at 706 and 1086 Ω*cm^2. Secondary crosslinking was then induced on day 7. Both conditions experienced a substantial decline in TEER, dropping to 293 and 212 Ω*cm^2, and ultimately recovered back to their maximum TEER values after a few days. No significant differences were observed between the stiffening gel and the static gel.

To assess BMEC-like cells' response to UV light and free radical generation, a control experiment was performed with unmodified gelatin control gels. Cells on these substrates were exposed to identical conditions, namely exposure to UV light and UV light plus free radicals. Cells on these substrates exhibited TEER maxima at 3845 and 2838 Ω*cm^2. After exposure to secondary cross-linking conditions on day 7, TEER rapidly declined to 392 and 430 Ω*cm^2, a more substantial decline than the cells on gel-MA. Additionally, the UV-treated condition only recovered up to 1064 Ω*cm^2, a fraction of its maximum TEER value, and the UV plus free radical-treated condition dropped to negligible values and never recovered.

Since the decline in TEER occurred in both conditions, with and without LAP, it is likely that the exposure to UV light temporarily diminished barrier integrity. To minimize UV-induced loss of barrier properties in future experiments, blue light can be used instead because LAP also responds to blue light. Free radical generation did also contribute to loss of barrier properties because cells on unmodified gelatin never recovered. This lack of recovery validates that the gel-MA system is consuming the free radicals generated appropriately because cells on gel-MA that were treated with LAP did recover to their maximum TEER.

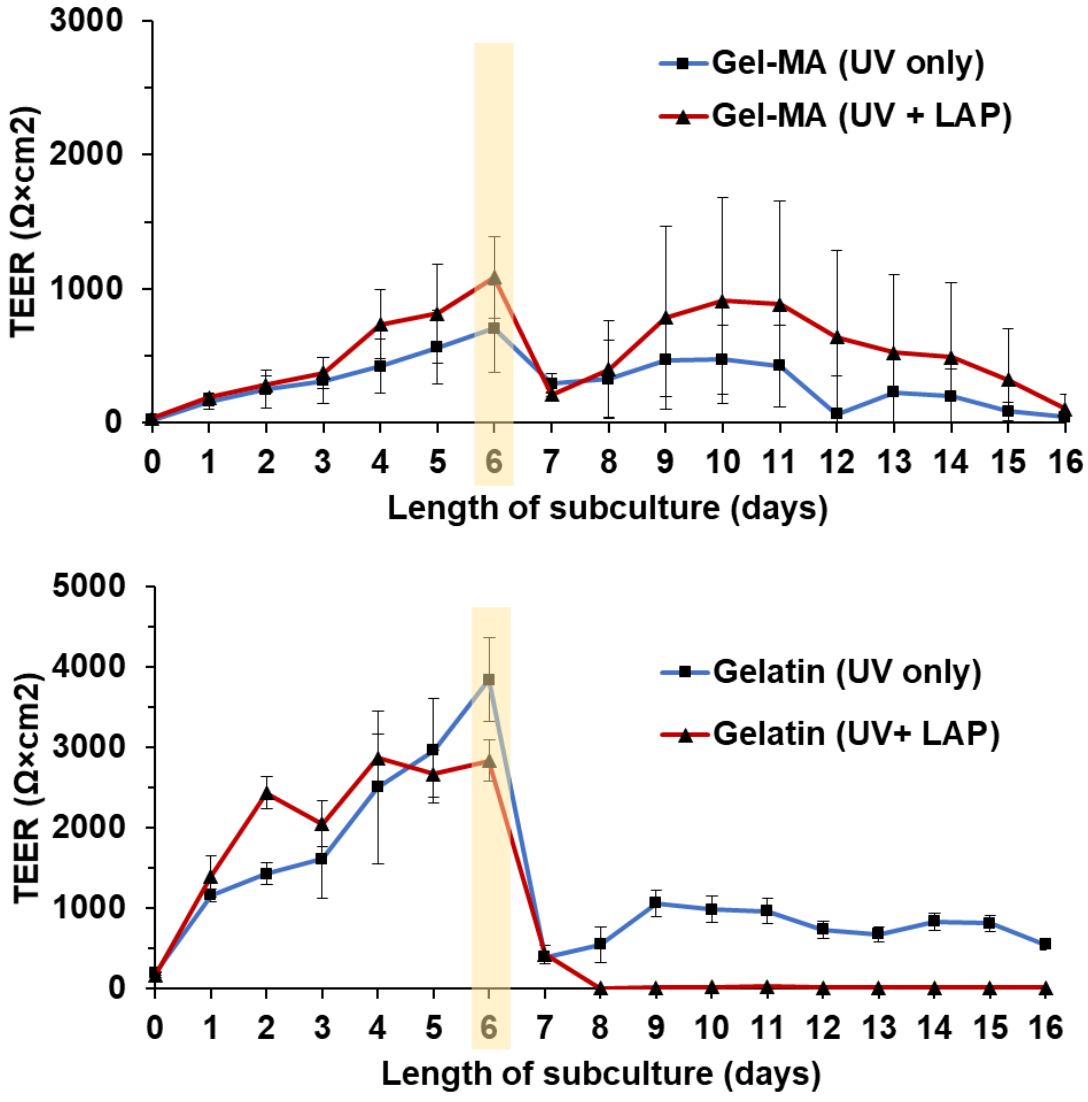

Figure 4.3 TEER responses of BMEC-like cells to a stiffening gel-MA substrate. BMEC-like cells were seeded onto gel-MA gels and gels were stiffened according to the workflow in Figure 4.1. 3 filters were prepared for each condition, and each filter was measured in triplicate. Values for each day represent mean ± standard deviation from these 9 measurements. The yellow highlight indicates the day of treatment. Cells either received UV exposure only (blue line) or UV exposure plus free radicals (red line) to determine if free radical generation was detrimental to barrier integrity. Cells on gel-MA substrates (top) experienced a decline in TEER but ultimately recovered back to the prior maxima. Cells on unmodified gelatin (bottom) were exposed to higher concentrations of free radicals because the gelatin could not consume them for cross-linking. Therefore, cells on gelatin experienced significant decline in TEER and never fully recovered.

4.4.3 *Fibrosis Phenotype in Embedded Tissue Model*

After 2 days of embedding in redox-cad hydrogel, a variety of vessel sizes were observed. Figure 4.4 illustrates a very large vessel with a diameter of approximately 30 µm and much smaller vessels that appear to be capillaries. These vessels likely already existed in the tissue chunks prior to embedded and remained intact during the thawing and embedding procedure. Tissue was stained for vascular marker collagen I, and Figure A.4.3 verifies that these structures are blood vessels.

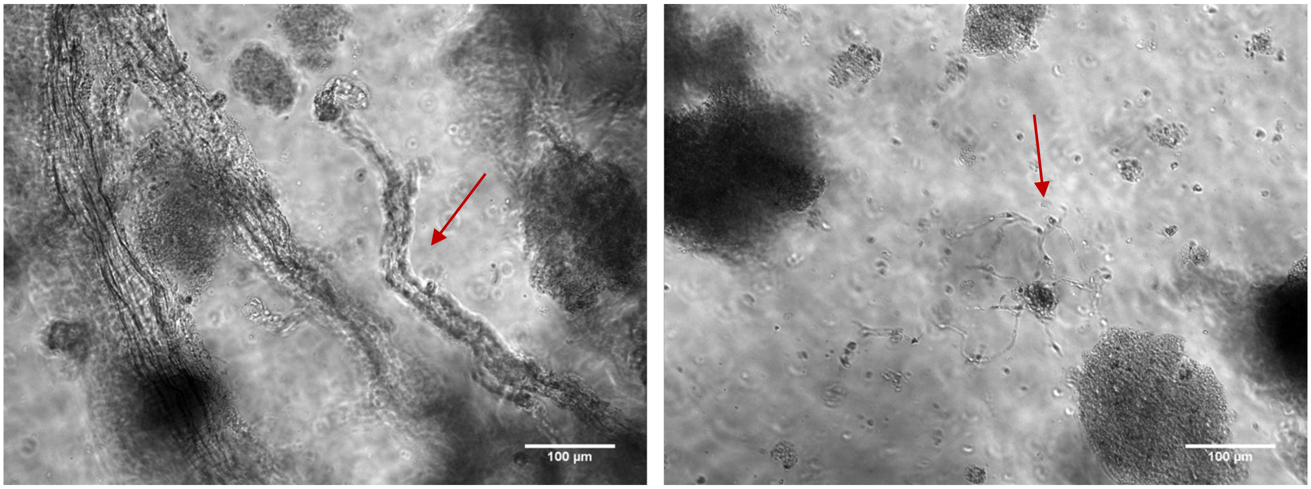

Figure 4.4 Diversity of vessel structures observed in embedded tissue. Post-mortem human tissue embedded in cad-functionalized hydrogels displayed both large and small vascular structures. Left panel shows an arteriole with a diameter of approximately 30 µm, and right panel shows a capillary structure that appears to have the diameter of a single cell. Scale bars represent 100 µm.

Treatment of embedded tissue with soluble amyloid-β induced a slight CAA effect. Upon treatment with monomeric amyloid-β (1-40), tissue was incubated for 2 days then fixed and stained for an amyloid marker, thiazine, and markers of perivascular fibrosis, TE-7 fibroblasts and α-SMA. CAA tissue displayed a strong vascular amyloid signal while control vessels displayed little to no vascular amyloid (Figure 4.5). In both conditions, vessels with amyloid signal also showed colocalization of TE-7 fibroblasts with α-SMA, indicating the potential presence of myofibroblasts in those vessels. To confirm this, further staining will need to be performed with additional myofibroblast markers. Ultimately, treatment with varying concentrations of amyloid-β may be used to model the different stages of CAA progression. Additionally, this hydrogel platform allows for secondary redox-induced cross-linking to further mimic CAA with ECM stiffening.

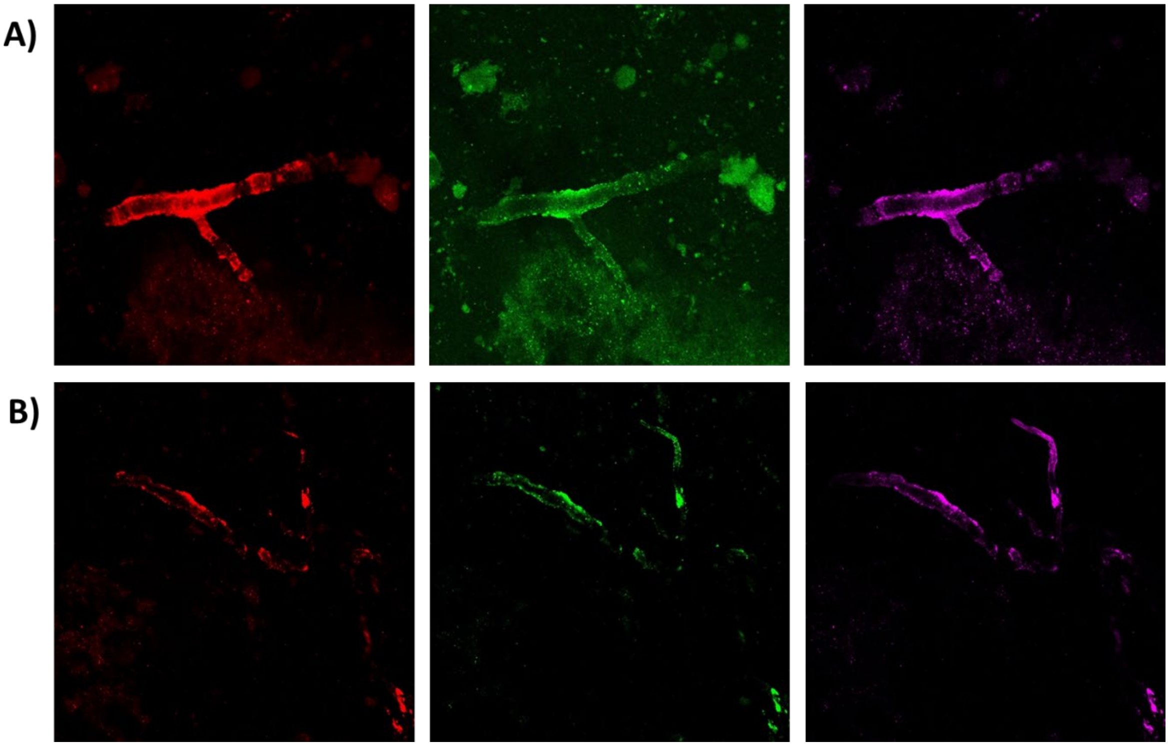

Figure 4.5 Markers of perivascular fibrosis in amyloid-treated embedded tissue structures. Post-mortem human tissue was embedded in cad-functionalized hydrogels and incubated with soluble amyloid-β at 10ug/mL for 2 days. Amyloid (red), α-SMA (green), and perivascular fibroblasts (magenta) were then imaged using a confocal microscope. Panel A represents tissue originating from a CAA patient, and panel B represents tissue originating from a control patient.

4.5 Conclusions

The design of functionalized hydrogels has allowed researchers to study a wider range of disease states, and how mechanical factors contribute to disease. Here, we utilized two unique gelatin-based hydrogel systems to mimic CAA disease conditions *in vitro*. First, a gel-MA hydrogel, which stiffens in response to light, was developed to measure real-time changes in barrier properties as a function of substrate stiffness. Then, cadherin-functionalized gels were used to embed post-mortem human tissue to support vascular survival and allow for imaging of vessel responses to soluble amyloid-β.

In the dynamic gel-MA platform, iPSC-derived BMEC-like cells formed physiologically relevant TEER values and responded to stiffening cues. No significant differences in TEER were observed between the static condition and the stiffening condition. Because stiffness values were never quantified for these experimental conditions, it is possible that the increase in stiffness was not dramatic enough to produce a significant change in TEER. Cells on gel-MA substrates also exhibited lower TEER than cells on unmodified gelatin substrates, likely because gel-MA is softer and contains slightly fewer available RGD binding domains for cells to attach to the surface. However, average TEER values still reached 1000 Ω*cm^2, which is substantial enough to model the BBB *in vitro*.

There are multiple variables within the gel-MA platform that can be tuned to better mimic CAA conditions. Overall concentration of gel-MA polymer, degree of methacrylation, concentration of mTG in primary cross-linking step, concentration of LAP in secondary cross-linking step, and light intensity and exposure time can all be tuned to achieve desired stiffness values. Future work would involve quantifying stiffness of gel-MA gels via AFM as a function of each of these variables. One caveat with using the gel-MA system that other barrier-forming endothelial cells experience barrier disruption during stiffening step. If this can be overcome, possibly by minimizing exposure to excess free radicals or by using blue light instead of UV light, then this platform may be incredibly valuable for assessing real-time responses to a dynamic substrate.

Using the cad-functionalized gels, post-mortem human cortical vessels were preserved and embedded to model CAA. Vessel were collagen type I-positive, verifying that they are larger vessel structures. Smaller vessel structures were also revealed in brightfield images. CAA vessels were observed upon treatment with soluble amyloid-β. However, future experiments will need to perform photobleaching steps prior to immunostaining to eliminate autofluorescence, which is common in human tissue. To increase viability of the cryopreserved tissue in future experiments, slow thawing of tissue can also be optimized. Some have reported arterial fracturing when tissue is rapidly thawed, and slowly thawing from liquid nitrogen to -100°C is preferred[103]. Future work can also include grafting other peptides onto gelatin that may promote the growth and survival of blood vessels, instead of or in addition to cadherin peptides. Finally, amyloid monomers can also be pre-aggregated prior to incubation with embedded tissue to accelerate CAA presentation. Incubation of amyloid in salt solutions at various concentrations and various times causes aggregation of amyloid monomers. Each of these features can be tuned to better model CAA.

Both gel-MA and cad-gel are tunable systems that can be optimized to better mimic disease progression. Both contain secondary stiffening mechanisms that allow for real-time analysis. (The cad-gel platform is capable of redox-initiated secondary crosslinking after primary crosslinking with mTG.) An overall caveat of these systems is the batch-to-batch variability that comes with preparation of natural hydrogel systems. Different batches of mTG, for example, may yield different degrees of crosslinking in the primary step. Despite that, these platforms hold potential as model systems that support 2-D and 3-D modeling of human CAA, a phenotype that an important contributor to cognitive decline.

4.6 Appendix

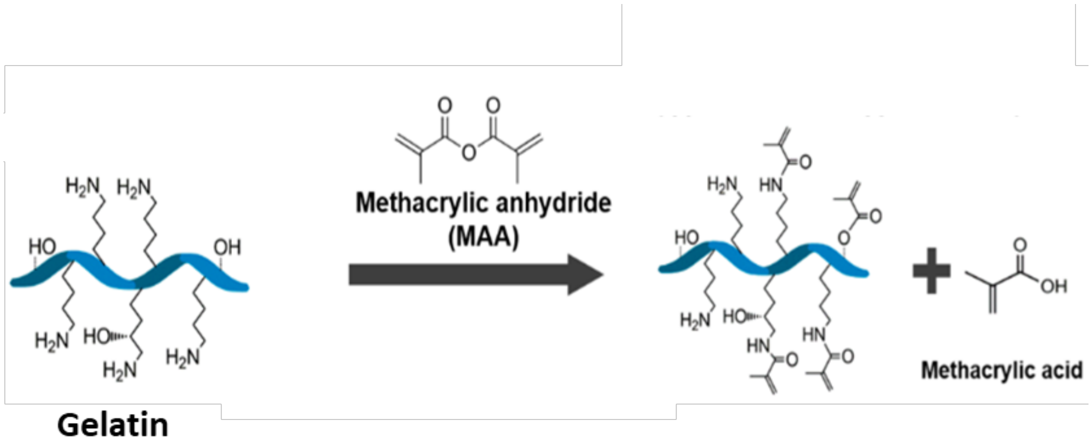

Figure A.4.1 Reaction for grafting methacrylate onto gelatin. Gelatin is reconstituted in water at 10% (w/v) then mixed with methacrylic anhydride for up to 3 hours.

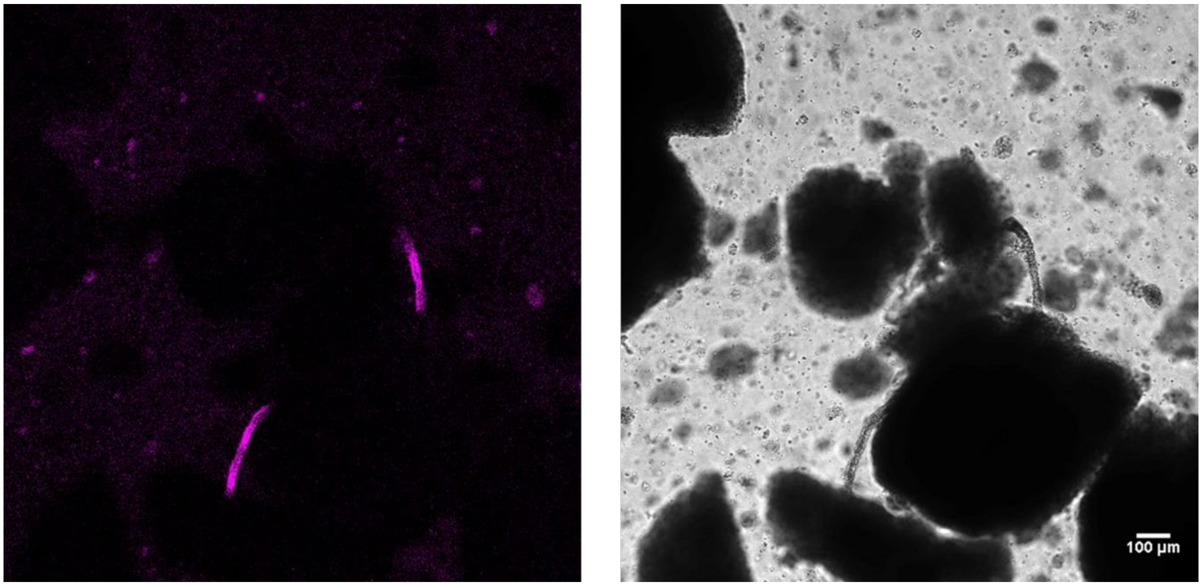

Figure A.4.2 Confirmation of vascular markers in embedded tissue. Post-mortem human tissue embedded in cad-functionalized hydrogels displayed vessel-like structures in brightfield images (right). To confirm that these structures were blood vessels, tissue was stained for collagen type I, a constituent of the vessel ECM. Colocalization of collagen I signal with the brightfield structures confirms that these structures are arteries, arterioles, or veins.

Chapter 5

CONCLUSIONS AND FUTURE OUTLOOK

5.1 Summary

In this dissertation, I have discussed our work to examine the effect of extracellular stiffness on brain vasculature. As discussed in the introduction, the burden of Alzheimer's disease massive, and it will only grow larger with increasing life expectancies. AD is historically characterized by two hallmarks, amyloid-β plaques and neurofibrillary tau tangles. However, growing evidence suggests that vasculature dysfunction contributes to cognitive decline. In 90% of AD patients, amyloid-β aggregates and deposits onto arterioles and limits autoregulation, kills vascular smooth muscle cells, and leads to increased microhemorrhage events. Little is known about what causes CAA, but common risk factors and symptoms exist between AD and vascular disease. Multiple reports have suggested that amyloid-β deposition in CAA leads to vessel stiffening, but no one has explicitly proven it[66,94]. This dissertation aimed to characterized stiffness changes that occur in CAA vasculature, to utilize an *in vitro* model system to measure endothelial responses to stiffness, and provide alternate hydrogel approaches to modeling CAA in 2-D and 3-D using human cells.

First, post-mortem human tissue was analyzing using atomic force microscopy and IHC. AFM measurements of 10 patient samples revealed that vessel stiffness is substantially higher when amyloid aggregates are present in the vessel wall. In addition, LOX enzymes are present in areas of amyloid aggregation, suggesting that LOX contributes to aggregation via lysine residue cross-linking or overall tissue stiffening. Since tissue stiffening and LOX are markers of tissue fibrosis, additional fibrosis markers were examined in the human tissue. Perivascular fibroblast-like cells were present in both control and CAA cortical vessels, but fibroblasts in CAA vessels exhibited colocalization of α-SMA, indicating the presence of myofibroblasts. In fibrosis, myofibroblasts over-secrete ECM proteins and ECM-remodeling enzymes to increase stiffness of the tissue microenvironment. Because fibrosis is well characterized in peripheral tissues, drawing parallels between fibrosis and CAA may help to extrapolate novel mechanisms of CAA.

Next, hydrogel substrates were incorporated into an existing *in vitro* model system to study substrate stiffness effects on the BBB. Based on previous work from our lab, we knew that iPSC-derived BMEC-like cells were responsive to shear stress in gelatin macrochannel devices[50]. Preliminary work in studying the effects of substrate stiffness involved incorporation of gelatin substrates in transwell TEER assays. Cells exhibited higher TEER on compliant substrates than a bare transwell, and further, modifications to gelatin concentration yielded statistically significant TEER maxima. This preliminary finding that compliant hydrogel substrates motivated additional work to examine stiffness. We moved to a polyacrylamide hydrogel system in which stiffness could be tuned independent of ECM presentation. We tested three stiffness conditions, 1, 20, and 150 kPa, and found that cells exhibit no TEER on the softest gels and very similar TEER on 20 and 150 kPa gels. Cells on the stiffest substrate declined more rapidly than cells on 20 kPa substrates. Efflux activity was not affected by stiffness.

Phenotypic, transcriptomic, and phosphoproteomic analyses were also performed on iPSC-derived BMEC-like cells as a function of stiffness. Actin reorganized in response to stiffness such that very soft and very stiff substrates yielded more intracellular stress fibers while cells on 20 kPa substrates had mostly cortical actin. Independent of hydrogel substrates, actin disruption via jasplak treatment caused a rapid decline in TEER. Surprisingly, tight junction width and tortuosity was unaffected by substrate stiffness. Bulk RNA sequencing and pathway analysis concluded that 20 kPa substrates produced cells that were more quiescent. In other words, genes associated with cell cycle were upregulated in 1 and 150 kPa cells relative to 20 kPa cells. A phosphoproteome array identified differences in activation of common kinases between 20 and 150 kPa conditions. These findings confirm trends from peripheral endothelial cell studies, namely that substrate stiffness increases worsen barrier function.

Finally, alternative approaches to modeling CAA *in vitro* were proposed. A dynamic stiffening hydrogel was incorporated into iPSC-derived BBB model to measure real-time changes to a stiffening substrate. Cells formed physiological TEER values on gel-MA substrates, but TEER was overall lower in this system in comparison to unmodified gelatin controls. Stiffening conditions, UV light and free radical generation, caused temporary decline in TEER but cells ultimately recovered back to their TEER maxima. A cadherin-functionalized gel was used to embed post-mortem human tissue to promote survival of existing cortical vasculature. Large and small vascular structures were observed upon embedding, and presence of collagen type I in these structures confirmed that they were vessels. Treatment with soluble amyloid-β yielded vasculature with amyloid aggregates in both CAA and control patient samples, however, this finding needs to be repeated with photobleaching to confirm that the signal is not coming from inherent autofluorescence of the human tissue. These platforms propose alternative models for studying CAA as opposed to the animal models that currently exist. These hydrogel platforms have tunable properties that can be optimized in future work to better mimic the CAA phenotype.

5.2 Future Directions

To further elucidate CAA disease mechanisms and to uncover deeper biological mechanisms of stiffness-mediated barrier modifications in BMECs, follow-up and tangential work can be performed. Specifically, the following topics can be investigated: 1) the synergistic effect of substrate stiffness and amyloid-β presentation on neurovascular function, and 2) LOX contribution to amyloid-β oligomer formation, and 3) Rho-kinase activation in BMECs.

5.2.1 Synergistic Effect of Substrate Stiffness and Amyloid-β Presentation on Neurovascular Function

In CAA, amyloid-β aggregates deposit onto the medial layer of arterioles and make direct contact with vascular smooth muscle cells (VSMCs), endothelial cells, and astrocyte end feet. Biomechanical properties of the vessels were explored in chapter 2, and the biochemical effect of increasing levels of amyloid-β in the vessel microenvironment has been briefly reported in literature. Primary human VSMCs upregulate complement pathway-associated genes when exposed to soluble amyloid-β *in vitro*[104]. In addition, in post-mortem human tissue, CAA vessels were positive for complement component 6[105]. This complement activation contributes to overall VSMC death in CAA. Using the polyacrylamide hydrogel substrates from chapter 3, we can perform experiments to determine if stiffness and amyloid-β cues act in synergy to accelerate complement activation in VSMCs. We can also use this platform to observe changes in BMEC integrity as a function of the synergistic effect of stiffness and amyloid-β.

To fabricate hydrogels containing both stiffness and amyloid-β cues, polyacrylamide hydrogels of 1, 20, and 150 kPa can be produced and coated with synthetic human amyloid-β.

Previous work in our lab has shown that amyloid-β monomers can be aggregated into fibrils upon exposure to salt solutions. Varying degrees of aggregation can be performed, and resulting fibrils can be used to coat polyacrylamide gel surfaces in combination with native ECM proteins, such as collagen and fibronectin. Since the succinimidyl linker binds to amine groups to link ECM proteins to the polyacrylamide gel surface, the amyloid-β peptide aggregates should bind as well. Modifying the ratio of amyloid-β to native ECM allows for investigation of biochemical signaling, and modifying the ratio alongside hydrogel stiffness allows for investigation of synergistic effects. For VSMCs, expression of the genes of the classical complement pathway, C1qB, C1r, C1s, C2, C3, C4, C5, C6, C7, C8 and C9, can be measured. This proposed work would provide insight into the contribution of a stiffening ECM and increasing amyloid-β presentation on complement activation in VSMCs. In BMECs, the same milieu of characterization techniques that were utilized in chapter 3 can be applied to cells adhered to amyloid-β-coated hydrogels. Since basement membrane composition is critical for endothelial cell identity, this work may reveal changes to BMEC integrity in response to a transforming ECM composition. Additionally, it has been shown that LDL receptor-related protein-1 (LRP-1) clears amyloid-β from the brain via BMECs, and increased amyloid-β accumulation correlates with loss of LRP-1[106]. To determine if CAA conditions, namely stiffening substrate and increased amyloid-β presentation, contribute to loss of LRP-1 in BMECs, LRP-1 expression levels and activity can be quantified using this experimental system.

Using existing lab protocols, we can analyze the synergistic effects of stiffness and amyloid presentation on neurovascular cell function. In addition to the materials protocols used, our lab has protocols for deriving BMECs and VSMCs from human iPSCs, allowing for potentially further analysis of genetic or patient-specific factors contributing to CAA. ApoE4, for example, has increased prevelance in AD, and knockout of ApoE was shown to reduce LRP-1-mediated amyloid-β clearance at the BBB[106,107]. Therefore, ApoE4-containing iPSCs may useful in these experiments in revealing additional disease mechanisms. Overall, this work would be valuable in gaining insight into VSMC and BMEC dysregulation that occurs in response to the multifactorial extracellular changes during CAA disease progression,

5.2.2 LOX Contribution to Amyloid-β Oligomer Formation

The assembly of amyloid-β monomers into oligomers then fibrils is a crucial first step in AD and CAA pathogenesis. Lysine residues on amyloid-β play a key role in stabilizing β-sheets of amyloid-β fibrils and in mediating cytotoxic effects[66]. LOX, which acts on lysine residues in native ECM to induce cross-linking, co-localizes to amyloid-β aggregates in AD and CAA, as seen in chapter 2[68]. However, the role that LOX plays is unclear—does it accelerate amyloid-β assembly, or does it trap amyloid-β structures in the native ECM being cross-linked? The answer to this question will determine whether LOX inhibitors, such as BAPN, may be used as potential therapeutics for AD and CAA.

As stated previously, our lab is able to produce amyloid-β aggregates from synthetic human amyloid-β. To determine the effect of LOX on oligomer formation, amyloid-β monomer solutions can be supplemented with recombinant LOX and cofactor LTQ. A technique called circular dichroism (CD) spectroscopy, used in previous amyloid-β assembly studies, can be used to measure how quickly secondary structures are formed[66]. TEM and western blotting can also be used to measure the size of larger structures formed. These data will provide insight into the link between LOX and amyloid-β and reveal whether BAPN may be useful as a potential therapy for preventing amyloid-β aggregation.

5.2.3 Rho-kinase Signaling in iPSC-derived BMECs

Rho kinase signaling is linked to the formation of stress fibers and focal adhesions, and it plays a major role mechanotransduction[108]. Rho kinase activation has also been associated with loss of tight junction integrity in primary human BMECs via phosphorylation of occludin and claudin-5[109]. In chapter 3 of this dissertation, RNA sequencing data revealed that genes associated with Rho GTPases were upregulated on 1 kPa substrates relative to 20 and 150 kPa substrates. This Rho activation may explain why negligible TEER was observed on 1 kPa substrates; however, follow-up work is required to validate this. To assess tight junction disruption on 1 kPa substrates, levels of occuldin, claudin-5, phosphorylated occludin, and phosphorylation claudin-5 in BMECs cultured on polyacrylamide hydrogels can be measured. More phosphorylated occludin and claudin-5 would indicate more barrier disruption. BMECs can also be treated with a Rho kinase inhibitor to determine if tight junction disruption is mediated by Rho kinase activation.

An important caveat is that BMECs on hydrogel substrates can potentially be affected by other properties of the hydrogel besides stiffness, namely ECM density and porosity. Interestingly, in the RNA sequencing pathway analysis, a significant change in Rho signaling was only observed in the 1 kPa comparisons. No differences in Rho signaling genes were observed between the 20 and 150 kPa conditions, suggesting that stiffness may not have directly caused this change. Of the three polyacrylamide formulations used in these experiments, a relatively stark difference in overall polymer concentration was used between the 1 kPa and higher stiffness gels. The 1 kPa gels contained 3% acrylamide in the precursor solution while 20 and 150 kPa gels contained 15% acrylamide. Although separate mechanisms exist for achieving stiffness and ECM presentation, it is possible that this stark difference in acrylamide content yielded different degrees of ECM presentation. To rule out this possibility, amount of bound protein can be quantified across the three polyacrylamide formulations. Once ECM presentation bias is ruled out, further work can be performed to assess the significance of Rho kinase signaling on tight junction integrity.

Broader impacts of this work would be to inform future *in vitro* hydrogel models of the optimal stiffness conditions for iPSC-derived BMEC barrier formation. In addition, the finding that iPSC-derived BMECs form suboptimal barrier properties on 1 kPa substrates means that stiffness of the intimal basement membrane likely does not match bulk brain stiffness values. Regional heterogeneity in stiffness likely exists between the vasculature to the brain parenchyma, and this information may also be valuable in informing design of future disease models.

5.3 Conclusions

Overall, this dissertation provides insight into stiffness changes that occur in CAA and the implications of those stiffness modifications on BBB endothelial cells. Loss of autoregulation of blood flow in arterioles is a primary contributor to cognitive decline that occurs in CAA patients, and the vessel stiffening reported in this dissertation suggests that biophysical forces drive vessel dysregulation. This stiffening, in combination with loss of vascular smooth muscle cells, likely prevents arterioles from contracting and dilating appropriately to direct blood flow to different areas of the brain, which is an important feature of brain vasculature. Additionally, BMECs experience optimal barrier properties on substrates matching the stiffness of control human cortical vessels. Proposed hydrogel systems may be used to model CAA *in vitro* to further characterize this disease phenotype. Future work would be valuable for further elucidating CAA mechanisms and designing next-generation *in vitro* BBB models.

Chapter 6

REFERENCES

1. Oxford, A. E., Stewart, E. S. & Rohn, T. T. Clinical Trials in Alzheimer's Disease: A Hurdle in the Path of Remedy. *Int J Alzheimers Dis* **2020**, (2020).
2. Hebert, L. E., Weuve, J., Scherr, P. A. & Evans, D. A. Alzheimer disease in the United States (2010–2050) estimated using the 2010 census. *Neurology* **80**, 1778–1783 (2013).
3. Amyloid Plaques and Neurofibrillary Tangles. *BrightFocus Foundation* https://www.brightfocus.org/alzheimers-disease/infographic/amyloid-plaques-and-neurofibrillary-tangles (2015).
4. Jellinger, K. A. & Attems, J. Neuropathological evaluation of mixed dementia. *Journal of the Neurological Sciences* **257**, 80–87 (2007).
5. Obermeier, B., Daneman, R. & Ransohoff, R. M. Development, maintenance and disruption of the blood-brain barrier. *Nat Med* **19**, 1584–1596 (2013).
6. Walsh, D. M. *et al.* Naturally secreted oligomers of amyloid β protein potently inhibit hippocampal long-term potentiation *in vivo*. *Nature* **416**, 535–539 (2002).
7. Wei, W. *et al.* Amyloid beta from axons and dendrites reduces local spine number and plasticity. *Nat Neurosci* **13**, 190–196 (2010).
8. Ahmad, M. H., Fatima, M. & Mondal, A. C. Influence of microglia and astrocyte activation in the neuroinflammatory pathogenesis of Alzheimer's disease: Rational insights for the therapeutic approaches. *Journal of Clinical Neuroscience* **59**, 6–11 (2019).
9. Kennedy, M. E. *et al.* The BACE1 inhibitor verubecestat (MK-8931) reduces CNS β-amyloid in animal models and in Alzheimer's disease patients. *Science Translational Medicine* **8**, 363ra150-363ra150 (2016).
10. Egan, M. F. *et al.* Randomized Trial of Verubecestat for Mild-to-Moderate Alzheimer's Disease. *New England Journal of Medicine* (2018) doi:10.1056/NEJMoa1706441.
11. Hawkes, N. Merck ends trial of potential Alzheimer's drug verubecestat. *BMJ* **356**, j845 (2017).
12. Doody, R. S. *et al.* A Phase 3 Trial of Semagacestat for Treatment of Alzheimer's Disease. *New England Journal of Medicine* **369**, 341–350 (2013).
13. Vellas, B. Tarenflurbil for Alzheimer's disease: a "shot on goal" that missed. *The Lancet Neurology* **9**, 235–237 (2010).
14. Salloway, S. *et al.* Two Phase 3 Trials of Bapineuzumab in Mild-to-Moderate Alzheimer's Disease. *New England Journal of Medicine* **370**, 322–333 (2014).

15. Doody, R. S. *et al.* Phase 3 Trials of Solanezumab for Mild-to-Moderate Alzheimer's Disease. *New England Journal of Medicine* **370**, 311–321 (2014).

16. Pankevich, D. E., Altevogt, B. M., Dunlop, J., Gage, F. H. & Hyman, S. E. Improving and Accelerating Drug Development for Nervous System Disorders. *Neuron* **84**, 546–553 (2014).

17. Bowler, J. V., Munoz, D. G., Merskey, H. & Hachinski, V. Fallacies in the pathological confirmation of the diagnosis of Alzheimer's disease. *Journal of Neurology, Neurosurgery & Psychiatry* **64**, 18–24 (1998).

18. Zekry, D., Hauw, J.-J. & Gold, G. Mixed Dementia: Epidemiology, Diagnosis, and Treatment. *Journal of the American Geriatrics Society* **50**, 1431–1438 (2002).

19. Langa, K. M., Foster, N. L. & Larson, E. B. Mixed Dementia: Emerging Concepts and Therapeutic Implications. *JAMA* **292**, 2901–2908 (2004).

20. Van Iterson, E. H., Snyder, E. M., Joyner, M. J., Johnson, B. D. & Olson, T. P. Intrathecal fentanyl blockade of afferent neural feedback from skeletal muscle during exercise in heart failure patients: Influence on circulatory power and pulmonary vascular capacitance. *International Journal of Cardiology* **201**, 384–393 (2015).

21. Weekman, E. M. *et al.* Reduced Efficacy of Anti-Aβ Immunotherapy in a Mouse Model of Amyloid Deposition and Vascular Cognitive Impairment Comorbidity. *J Neurosci* **36**, 9896–9907 (2016).

22. 2015 Alzheimer's disease facts and figures. *Alzheimer's & Dementia* **11**, 332–384 (2015).

23. Mahley, R. W. Apolipoprotein E: from cardiovascular disease to neurodegenerative disorders. *J Mol Med (Berl)* **94**, 739–746 (2016).

24. Davignon J, Gregg R E, & Sing C F. Apolipoprotein E polymorphism and atherosclerosis. *Arteriosclerosis: An Official Journal of the American Heart Association, Inc.* **8**, 1–21 (1988).

25. APOE4 Causes Widespread Molecular and Cellular Alterations Associated with Alzheimer's Disease Phenotypes in Human iPSC-Derived Brain Cell Types. - PubMed - NCBI. https://www.ncbi.nlm.nih.gov/pubmed/29861287.

26. Abbott, N. J., Rönnbäck, L. & Hansson, E. Astrocyte–endothelial interactions at the blood–brain barrier. *Nat Rev Neurosci* **7**, 41–53 (2006).

27. Hawkins, B. T. & Davis, T. P. The Blood-Brain Barrier/Neurovascular Unit in Health and Disease. *Pharmacol Rev* **57**, 173–185 (2005).

28. Montagne, A. *et al.* Blood-Brain Barrier Breakdown in the Aging Human Hippocampus. *Neuron* **85**, 296–302 (2015).

29. Park, R., Kook, S.-Y., Park, J.-C. & Mook-Jung, I. Aβ1-42 reduces P-glycoprotein in the blood-brain barrier through RAGE-NF-κB signaling. *Cell Death Dis* **5**, e1299 (2014).

30. Vogelgesang, S. *et al.* Deposition of Alzheimer's beta-amyloid is inversely correlated with P-glycoprotein expression in the brains of elderly non-demented humans. *Pharmacogenetics* **12**, 535–541 (2002).

31. Gejl, M. *et al.* Blood-Brain Glucose Transfer in Alzheimer's disease: Effect of GLP-1 Analog Treatment. *Scientific Reports* **7**, 17490 (2017).

32. Farkas, E. & Luiten, P. G. M. Cerebral microvascular pathology in aging and Alzheimer's disease. *Progress in Neurobiology* **64**, 575–611 (2001).

33. Lauretti, E. & Praticò, D. Glucose deprivation increases tau phosphorylation via P38 mitogen-activated protein kinase. *Aging Cell* **14**, 1067–1074 (2015).

34. Nation, D. A. *et al.* Blood–brain barrier breakdown is an early biomarker of human cognitive dysfunction. *Nature Medicine* **25**, 270 (2019).

35. Mancardi, G. L., Perdelli, F., Rivano, C., Leonardi, A. & Bugiani, O. Thickening of the basement membrane of cortical capillaries in Alzheimer's disease. *Acta Neuropathol* **49**, 79–83 (1980).

36. Kalaria, R. N. & Pax, A. B. Increased collagen content of cerebral microvessels in Alzheimer's disease. *Brain Research* **705**, 349–352 (1995).

37. Christie, R., Yamada, M., Moskowitz, M. & Hyman, B. Structural and Functional Disruption of Vascular Smooth Muscle Cells in a Transgenic Mouse Model of Amyloid Angiopathy. *Am J Pathol* **158**, 1065–1071 (2001).

38. van Veluw, S. J. *et al.* Cerebral amyloid angiopathy severity is linked to dilation of juxtacortical perivascular spaces. *J Cereb Blood Flow Metab* **36**, 576–580 (2016).

39. Murphy, M. C. *et al.* Decreased brain stiffness in Alzheimer's disease determined by magnetic resonance elastography. *J. Magn. Reson. Imaging* **34**, 494–498 (2011).

40. Murphy, M. C. *et al.* Regional brain stiffness changes across the Alzheimer's disease spectrum. *Neuroimage Clin* **10**, 283–290 (2015).

41. Avery, D. *et al.* Extracellular matrix directs phenotypic heterogeneity of activated fibroblasts. *Matrix Biol.* **67**, 90–106 (2018).

42. Cecelja, M. & Chowienczyk, P. Role of arterial stiffness in cardiovascular disease. *JRSM Cardiovasc Dis* **1**, (2012).

43. Deplano, V. *et al.* Biaxial tensile tests of the porcine ascending aorta. *J Biomech* **49**, 2031–2037 (2016).

44. Bloodworth Nathaniel C. *et al.* Bone Marrow–Derived Proangiogenic Cells Mediate Pulmonary Arteriole Stiffening via Serotonin 2B Receptor Dependent Mechanism. *Circulation Research* **123**, e51–e64 (2018).

45. Sewell-Loftin, M. K., Brown, C. B., Scott Baldwin, H. & David Merryman, W. Novel technique for quantifying mouse heart valve leaflet stiffness with atomic force microscopy. *J Heart Valve Dis* **21**, 513–520 (2012).

46. O'Grady, B. J. *et al.* Development of an N-Cadherin Biofunctionalized Hydrogel to Support the Formation of Synaptically Connected Neural Networks. *ACS Biomater. Sci. Eng.* **6**, 5811–5822 (2020).

47. Gray, K. M. & Stroka, K. M. Vascular endothelial cell mechanosensing: New insights gained from biomimetic microfluidic models. *Seminars in Cell & Developmental Biology* (2017) doi:10.1016/j.semcdb.2017.06.002.

48. Huynh, J. *et al.* Age-Related Intimal Stiffening Enhances Endothelial Permeability and Leukocyte Transmigration. *Sci Transl Med* **3**, 112ra122 (2011).

49. Mammoto, A. *et al.* Control of lung vascular permeability and endotoxin-induced pulmonary oedema by changes in extracellular matrix mechanics. *Nature Communications* **4**, 1759 (2013).

50. Faley, S. L. *et al.* iPSC-Derived Brain Endothelium Exhibits Stable, Long-Term Barrier Function in Perfused Hydrogel Scaffolds. *Stem Cell Reports* **0**, (2019).

51. Jalili, N. & Laxminarayana, K. A review of atomic force microscopy imaging systems: application to molecular metrology and biological sciences. *Mechatronics* **14**, 907–945 (2004).

52. Christ, A. F. *et al.* Mechanical difference between white and gray matter in the rat cerebellum measured by scanning force microscopy. *Journal of Biomechanics* **43**, 2986–2992 (2010).

53. Elkin, B. S., Azeloglu, E. U., Costa, K. D. & Morrison III, B. Mechanical Heterogeneity of the Rat Hippocampus Measured by Atomic Force Microscope Indentation. *Journal of Neurotrauma* **24**, 812–822 (2007).

54. Ghiso, J., Tomidokoro, Y., Revesz, T., Frangione, B. & Rostagno, A. CEREBRAL AMYLOID ANGIOPATHY AND ALZHEIMER'S DISEASE. *Hirosaki Igaku* **61**, S111–S124 (2010).

55. Scuteri, A., Brancati, A. M., Gianni, W., Assisi, A. & Volpe, M. Arterial stiffness is an independent risk factor for cognitive impairment in the elderly: a pilot study. *Journal of Hypertension* **23**, 1211–1216 (2005).

56. Fukuhara, M. *et al.* Prediction of Cognitive Function by Arterial Stiffness in the Very Elderly. *Circulation Journal* **70**, 756–761 (2006).

57. Waldstein, S. R. *et al.* Pulse Pressure and Pulse Wave Velocity Are Related to Cognitive Decline in the Baltimore Longitudinal Study of Aging. *Hypertension* **51**, 99–104 (2008).

58. Kimbrough, I. F., Robel, S., Roberson, E. D. & Sontheimer, H. Vascular amyloidosis impairs the gliovascular unit in a mouse model of Alzheimer's disease. *Brain* **138**, 3716–3733 (2015).

59. Gilad, G. M., Kagan, H. M. & Gilad, V. H. Evidence for increased lysyl oxidase, the extracellular matrix-forming enzyme, in Alzheimer's disease brain. *Neuroscience Letters* **376**, 210–214 (2005).

60. Johnson, G. V. W. *et al.* Transglutaminase activity is increased in Alzheimer's disease brain. *Brain Research* **751**, 323–329 (1997).

61. Kohn, J. C., Lampi, M. C. & Reinhart-King, C. A. Age-related vascular stiffening: causes and consequences. *Front. Genet.* **6**, (2015).

62. Balestrini, J. L., Chaudhry, S., Sarrazy, V., Koehler, A. & Hinz, B. The mechanical memory of lung myofibroblasts. *Integrative Biology* **4**, 410–421 (2012).

63. Szeto, S. G. *et al.* YAP/TAZ Are Mechanoregulators of TGF-β-Smad Signaling and Renal Fibrogenesis. *J Am Soc Nephrol* **27**, 3117–3128 (2016).

64. Achterberg, V. F. *et al.* The Nano-Scale Mechanical Properties of the Extracellular Matrix Regulate Dermal Fibroblast Function. *Journal of Investigative Dermatology* **134**, 1862–1872 (2014).

65. Bloodworth Nathaniel C. *et al.* Bone Marrow–Derived Proangiogenic Cells Mediate Pulmonary Arteriole Stiffening via Serotonin 2B Receptor Dependent Mechanism. *Circulation Research* **123**, e51–e64 (2018).

66. Sinha, S., Lopes, D. H. J. & Bitan, G. A Key Role for Lysine Residues in Amyloid β-Protein Folding, Assembly, and Toxicity. *ACS Chem Neurosci* **3**, 473–481 (2012).

67. VanderBurgh, J. A. & Reinhart-King, C. A. Chapter Ten - The Role of Age-Related Intimal Remodeling and Stiffening in Atherosclerosis. in *Advances in Pharmacology* (ed. Khalil, R. A.) vol. 81 365–391 (Academic Press, 2018).

68. Wilhelmus, M. M. M., Bol, J. G. J. M., van Duinen, S. G. & Drukarch, B. Extracellular matrix modulator lysyl oxidase colocalizes with amyloid-beta pathology in Alzheimer's disease and hereditary cerebral hemorrhage with amyloidosis—Dutch type. *Experimental Gerontology* **48**, 109–114 (2013).

69. Harvey, A., Montezano, A. C., Lopes, R. A., Rios, F. & Touyz, R. M. Vascular Fibrosis in Aging and Hypertension: Molecular Mechanisms and Clinical Implications. *Canadian Journal of Cardiology* **32**, 659–668 (2016).

70. Vanlandewijck, M. *et al.* A molecular atlas of cell types and zonation in the brain vasculature. *Nature* (2018) doi:10.1038/nature25739.

71. Ongali, B. *et al.* Transgenic Mice Overexpressing APP and Transforming Growth Factor-β1 Feature Cognitive and Vascular Hallmarks of Alzheimer's Disease. *The American Journal of Pathology* **177**, 3071–3080 (2010).

72. Nicoll, J. A. R. *et al.* Aβ Species Removal After Aβ42 Immunization. *Journal of Neuropathology & Experimental Neurology* **65**, 1040–1048 (2006).

73. Califano, J. P. & Reinhart-King, C. A. A Balance of Substrate Mechanics and Matrix Chemistry Regulates Endothelial Cell Network Assembly. *Cel. Mol. Bioeng.* **1**, 122–132 (2008).

74. Hollmann, E. K. *et al.* Accelerated differentiation of human induced pluripotent stem cells to blood–brain barrier endothelial cells. *Fluids Barriers CNS* **14**, (2017).

75. Neal, E. H. *et al.* A Simplified, Fully Defined Differentiation Scheme for Producing Blood-Brain Barrier Endothelial Cells from Human iPSCs. *Stem Cell Reports* **12**, 1380–1388 (2019).

76. Neal, E. H. *et al.* Influence of basal media composition on barrier fidelity within human pluripotent stem cell-derived blood-brain barrier models. *bioRxiv* 2021.03.01.433282 (2021) doi:10.1101/2021.03.01.433282.

77. Poole, K. M., McCormack, D. R., Patil, C. A., Duvall, C. L. & Skala, M. C. Quantifying the vascular response to ischemia with speckle variance optical coherence tomography. *Biomed Opt Express* **5**, 4118–4130 (2014).

78. Kroon, D.-J. Hessian based Frangi Vesselness filter (https://www.mathworks.com/matlabcentral/fileexchange/24409-hessian-based-frangi-vesselness-filter). *MATLAB Central File Exchange*.

79. Wang, J., Vasaikar, S., Shi, Z., Greer, M. & Zhang, B. WebGestalt 2017: a more comprehensive, powerful, flexible and interactive gene set enrichment analysis toolkit. *Nucleic Acids Research* **45**, W130–W137 (2017).

80. McKee, C. T., Last, J. A., Russell, P. & Murphy, C. J. Indentation Versus Tensile Measurements of Young's Modulus for Soft Biological Tissues. *Tissue Engineering Part B: Reviews* **17**, 155–164 (2011).

81. Kohn, J. C., Lampi, M. C. & Reinhart-King, C. A. Age-related vascular stiffening: causes and consequences. *Front. Genet.* **6**, (2015).

82. Watanabe, K. *et al.* A ROCK inhibitor permits survival of dissociated human embryonic stem cells. *Nature Biotechnology* **25**, 681–686 (2007).

83. Krishnan, R. *et al.* Substrate stiffening promotes endothelial monolayer disruption through enhanced physical forces. *American Journal of Physiology-Cell Physiology* **300**, C146–C154 (2010).

84. Bogatcheva, N. V. & Verin, A. D. The role of cytoskeleton in the regulation of vascular endothelial barrier function. *Microvasc. Res.* **76**, 202–207 (2008).

85. Van Itallie, C. M., Fanning, A. S., Bridges, A. & Anderson, J. M. ZO-1 Stabilizes the Tight Junction Solute Barrier through Coupling to the Perijunctional Cytoskeleton. *Mol Biol Cell* **20**, 3930–3940 (2009).

86. Huveneers, S. *et al.* Vinculin associates with endothelial VE-cadherin junctions to control force-dependent remodeling. *Journal of Cell Biology* **196**, 641–652 (2012).

87. Bubb, M. R., Senderowicz, A. M., Sausville, E. A., Duncan, K. L. & Korn, E. D. Jasplakinolide, a cytotoxic natural product, induces actin polymerization and competitively inhibits the binding of phalloidin to F-actin. *J. Biol. Chem.* **269**, 14869–14871 (1994).

88. Waschke, J., Curry, F. E., Adamson, R. H. & Drenckhahn, D. Regulation of actin dynamics is critical for endothelial barrier functions. *American Journal of Physiology-Heart and Circulatory Physiology* **288**, H1296–H1305 (2005).

89. Greene, W. & Gao, S.-J. Actin Dynamics Regulate Multiple Endosomal Steps during Kaposi's Sarcoma-Associated Herpesvirus Entry and Trafficking in Endothelial Cells. *PLOS Pathogens* **5**, e1000512 (2009).

90. van Nieuw Amerongen G.P. *et al.* Involvement of Rho Kinase in Endothelial Barrier Maintenance. *Arteriosclerosis, Thrombosis, and Vascular Biology* **27**, 2332–2339 (2007).

91. Dbouk, H. A. *et al.* Actions of the protein kinase WNK1 on endothelial cells are differentially mediated by its substrate kinases OSR1 and SPAK. *PNAS* **111**, 15999–16004 (2014).

92. Zagórska, A. *et al.* Regulation of activity and localization of the WNK1 protein kinase by hyperosmotic stress. *J Cell Biol* **176**, 89–100 (2007).

93. Stebbins, M. J. *et al.* Activation of RARα, RARγ, or RXRα Increases Barrier Tightness in Human Induced Pluripotent Stem Cell-Derived Brain Endothelial Cells. *Biotechnology Journal* **13**, 1700093 (2018).

94. Kimbrough, I. F., Robel, S., Roberson, E. D. & Sontheimer, H. Vascular amyloidosis impairs the gliovascular unit in a mouse model of Alzheimer's disease. *Brain* **138**, 3716–3733 (2015).

95. Caliari, S. R. *et al.* Stiffening hydrogels for investigating the dynamics of hepatic stellate cell mechanotransduction during myofibroblast activation. *Scientific Reports* **6**, 21387 (2016).

96. Guvendiren, M. & Burdick, J. A. Stiffening hydrogels to probe short- and long-term cellular responses to dynamic mechanics. *Nature Communications* **3**, 792 (2012).

97. Loessner, D. *et al.* Functionalization, preparation and use of cell-laden gelatin methacryloyl–based hydrogels as modular tissue culture platforms. *Nature Protocols* **11**, 727–746 (2016).

98. Pepelanova, I., Kruppa, K., Scheper, T. & Lavrentieva, A. Gelatin-Methacryloyl (GelMA) Hydrogels with Defined Degree of Functionalization as a Versatile Toolkit for 3D Cell Culture and Extrusion Bioprinting. *Bioengineering (Basel)* **5**, (2018).

99. Wu, Y. *et al.* The influence of the stiffness of GelMA substrate on the outgrowth of PC12 cells. *Biosci Rep* **39**, (2019).

100. Hribar, K. C. *et al.* A Simple Three-dimensional Hydrogel Platform Enables Ex Vivo Cell Culture of Patient and PDX Tumors for Assaying Their Response to Clinically Relevant Therapies. *Mol Cancer Ther* **18**, 718–725 (2019).

101. Wang, J. *et al.* Ex vivo blood vessel bioreactor for analysis of the biodegradation of magnesium stent models with and without vessel wall integration. *Acta Biomaterialia* **50**, 546–555 (2017).

102. Kural, M. H., Dai, G., Niklason, L. E. & Gui, L. An Ex Vivo Vessel Injury Model to Study Remodeling. *Cell Transplant* **27**, 1375–1389 (2018).

103. Bakhach, J. The cryopreservation of composite tissues. *Organogenesis* **5**, 119–126 (2009).

104. Walker, D. G., Dalsing-Hernandez, J. E. & Lue, L.-F. Human postmortem brain-derived cerebrovascular smooth muscle cells express all genes of the classical complement pathway: A potential mechanism for vascular damage in cerebral amyloid angiopathy and Alzheimer's disease. *Microvascular Research* **75**, 411–419 (2008).

105. Schrag, M. *et al.* Correlation of hypointensities in susceptibility-weighted images to tissue histology in dementia patients with cerebral amyloid angiopathy: a postmortem MRI study. *Acta Neuropathol* **119**, 291–302 (2010).

106. Shibata, M. *et al.* Clearance of Alzheimer's amyloid-$\beta_{1\text{-}40}$ peptide from brain by LDL receptor–related protein-1 at the blood-brain barrier. *J Clin Invest* **106**, 1489–1499 (2000).

107. William Rebeck, G., Reiter, J. S., Strickland, D. K. & Hyman, B. T. Apolipoprotein E in sporadic Alzheimer's disease: Allelic variation and receptor interactions. *Neuron* **11**, 575–580 (1993).

108. Amano, M. *et al.* Formation of Actin Stress Fibers and Focal Adhesions Enhanced by Rho-Kinase. *Science* **275**, 1308–1311 (1997).

109. Persidsky, Y. *et al.* Rho-mediated regulation of tight junctions during monocyte migration across the blood-brain barrier in HIV-1 encephalitis (HIVE). *Blood* **107**, 4770–4780 (2006).